12-13-2019

# Power Management and Protection in MT-HVDC Systems with the Integration of High-Voltage Charging Stations

Fazel Mohammadi
*University of Windsor*

# Power Management and Protection in MT-HVDC Systems with the Integration of High-Voltage Charging Stations

By

**Fazel Mohammadi**

A Dissertation
Submitted to the Faculty of Graduate Studies
through the Department of Electrical and Computer Engineering
in Partial Fulfillment of the Requirements for
the Degree of Doctor of Philosophy
at the University of Windsor

Windsor, Ontario, Canada

2019

**Power Management and Protection in MT-HVDC Systems with the Integration of High-Voltage Charging Stations**

by

**Fazel Mohammadi**

APPROVED BY:

_____

C. Wang, External Examiner
Wayne State University

_____

R. Carriveau
Department of Civil and Environmental Engineering

_____

R. Rashidzadeh
Department of Electrical and Computer Engineering

_____

S. Erfani
Department of Electrical and Computer Engineering

_____

G.-A. Nazri, Co-Advisor
Department of Electrical and Computer Engineering

_____

M. Saif, Co-Advisor
Department of Electrical and Computer Engineering

December 13, 2019

DECLARATION OF CO-AUTHORSHIP / PREVIOUS PUBLICATION

## I. Co-Authorship

I hereby declare that this thesis incorporates material that is result of my research under the supervision of Prof. Mehrdad Saif, University of Windsor, ON, Canada and Prof. Gholam-Abbas Nazri, Wayne State, MI, U.S.A., as follows:

I was responsible for methodology, collecting resources, data analysis, writing—original draft preparation, and writing—review and editing. Prof. G.-A. Nazri and Prof. M. Saif were responsible for the supervision, and writing—review and editing.

I am aware of the University of Windsor Senate Policy on Authorship and I certify that I have properly acknowledged the contribution of other researchers to my thesis, and have obtained written permission from each of the co-author(s) to include the above material(s) in my thesis.

I certify that, with the above qualification, this thesis, and the research to which it refers, is the product of my own work.

## II. Previous Publication

This thesis includes several original papers that have been previously published/submitted for publication, as follows:

Chapter 2:

1. Fazel Mohammadi, Gholam-Abbas Nazri, Mehrdad Saif, "A Bidirectional Power Charging Control Strategy for Plug-in Hybrid Electric Vehicles," *Sustainability*, Vol. 11(16), Aug. 2019.

2. Fazel Mohammadi, Gholam-Abbas Nazri, Mehrdad Saif, "Modeling and Simulation of Hybrid Electric Vehicle Using MATLAB/Simulink," 5$^{th}$ International Conference on Power Generation Systems and Renewable Energy Technologies (PGSRET 2019), Aug. 2019.

Chapter 3:

1. Fazel Mohammadi, Gholam-Abbas Nazri, Mehrdad Saif, "An Improved Droop-Based Control Strategy for MT-HVDC Systems," Electronics, Vol. 9(1), Jan. 2020.

Chapter 4:

1. Fazel Mohammadi, Gholam-Abbas Nazri, Mehrdad Saif, "An Improved Mixed AC/DC Power Flow Algorithm in Hybrid AC/DC Grids with MT-HVDC Systems," Applied Sciences, Vol. 10(1), Jan. 2020.

Chapter 5:

1. Fazel Mohammadi, Gholam-Abbas Nazri, Mehrdad Saif, "A New Topology of a Fast Proactive Hybrid DC Circuit Breaker for MT-HVDC Grids," *Sustainability*, Vol. 11(16), Aug. 2019.

2. Fazel Mohammadi, Gholam-Abbas Nazri, Mehrdad Saif, "A Fast Fault Detection and Identification Approach in Power Distribution Systems," 5$^{th}$ International Conference on Power Generation Systems and Renewable Energy Technologies (PGSRET 2019), Aug. 2019.

I certify that I have obtained a written permission form the copyright owner(s) to include the above-published material(s) in my thesis. I certify that the above material describes work completed during my registration as a graduate student at the University of Windsor.

I certify that, to the best of my knowledge, my thesis does not infringe upon anyone's copyright nor violate any proprietary rights and that any ideas, techniques, quotations, or any other material from the work of other people included in my thesis, published or otherwise, are fully acknowledged in accordance with the standard referencing practices. Furthermore, to the extent that I have included copyrighted material that surpasses the bounds of fair dealing within the meaning of the Canada Copyright Act, I certify that I have obtained a written permission from

the copyright owner(s) to include such material(s) in my thesis and have included copies of such copyright clearances to my appendix.

I declare that this is a true copy of my thesis, including any final revisions, as approved by my thesis committee and the Graduate Studies office, and that this thesis has not been submitted for a higher degree to any other University or Institution.

# ABSTRACT

Due to the significant increase of the long-distance electricity demand, effective use of Distributed Generations (DGs) in power system, and the challenges in the expansion of new transmission lines to improve the reliability of power system reliability, utilizing Multi-Terminal HVDC (MT-HVDC) technology is an applicable, reliable, and cost-effective solution in hybrid AC/DC grids. MT-HVDC systems have flexibility in terms of independent active and reactive power flow (reversible control) and voltage control. Interconnecting two AC grids with different frequencies and transmitting electricity for the long-distance with low power-losses, which leads to less operation and maintenance costs, can be done through the MT-HVDC systems. The integration of large-scale remote DGs, e.g., wind farms, solar power plants, etc., and high-voltage charging stations for Electric Vehicles (EVs) into the power grid have different issues, such as economic, technical, and environmental challenges of transmission and network expansion/operation of both AC and DC grids. In details, damping oscillation, voltage support at different buses, operation of grid-connected inverters to the off-shore and on-shore AC systems, integrating of existing converter stations in MT-HVDC systems without major changes in control system, evaluation of communication infrastructure and also reactive power and filtering units' requirements in MT-HVDC systems are the technical challenges in this technology. Therefore, a reliable MT-HVDC system can be a possible mean of resolving all the above-mentioned issues. MT-HVDC systems need a control system that can bring stability to the power system during a certain period of the operation/planning time while providing effective and robust electricity.

This thesis presents an improved droop-based control strategy for the active and reactive power-sharing on the large-scale MT-HVDC systems integrating different types of AC grids considering the operation of the hybrid AC/DC grids under normal/contingency conditions. The main objective of the proposed strategy is to select the best parameters of the local terminal controllers at the site of each

converter station (as the primary controller) and a central master controller (supervisory controller) to control the Power Flow (PF) and balance the instantaneous power in MT-HVDC systems.

In this work, (1) various control strategies of MT-HVDC systems are investigated to propose (2) an improved droop-based power-sharing strategy of MT-HVDC systems while the loads (e.g., high-voltage charging stations) in power systems have significant changes, to improve the frequency response and accuracy of the PF control, (3) a new topology of a fast proactive Hybrid DC Circuit Breaker (HDCCB) to isolate the DC faults in MT-HVDC grids in case of fault current interruption. The results from this research work would include supporting energy adequacy, increasing renewable energy penetration, and minimizing losses when maintaining system integrity and reliability.

The proposed strategies are evaluated on different systems, and various case scenarios are applied to demonstrate their feasibility and robustness. The validation processes are performed using MATLAB software for programming, and PSCAD/EMTDC and MATLAB/Simulink for simulation.

DEDICATION

*To my family and supervisors who have supported me every step of the way.*

ACKNOWLEDGEMENTS

*I would like to sincerely thank my supervisors, Professor Mehrdad Saif and Professor Gholam-Abbas Nazri, for their inspiration, guidance, and support during my Ph.D. study at the University of Windsor.*

TABLE OF CONTENTS

LIST OF TABLES

LIST OF FIGURES

## RESEARCH MOTIVATIONS

Complex design, operation, and control system considering filter and reactive power compensation units, quality of the output voltage and current, need for a fast and high-quality protection system and expanding MT-HVDC systems are the major challenges in the area of MT-HVDC technology. Moreover, the interaction between MT-HVDC systems, DG resources, including high-voltage charging stations is another challenge in this area. Under the contingency condition, MT-HVDC systems should be able to transmit the available power to the local/remote loads. Therefore, the reliability of MT-HVDC systems performs a vital role in terms of adequacy (having sufficient substation/converters and both AC and DC grids to satisfy the loads) and security (having a robust system to be able to respond to the transient faults/outages) of the entire power systems. When it comes to interconnecting DG resources to AC grids, those challenges become more interesting as a new topic of research in MT-HVDC technology.

There are several technical barriers that manufacturers, network planners, and operators are trying to resolve to facilitate the deployment of the MT-HVDC systems. Protection and fault-current interruption in MT-HVDC systems are arguably the most challenging research and development problems that the manufacturers and academia are presently engaged in. As MT-HVDC systems are unprecedented with no operational experience, the network operators do not have much understanding of the interaction between an MT-HVDC system and the host AC systems and the overall stability. Moreover, there is a lack of clarity about whether and how the MT-HVDC systems could be operated and controlled to support the host AC systems. The prerequisite to study the above issues systematically is to develop a generic modeling and stability analysis framework for MT-HVDC systems that is compatible with those for conventional AC systems. This can then be used to analyze the overall stability of the hybrid AC/DC grids and identify and resolve potential interactions. System support provisions (for instance frequency support) through an MT-HVDC system are beneficial for the network

operation especially, considering the lower inertia of the turbine systems and interaction of high-voltage charging stations. However, they need to be exercised carefully to avoid adverse interactions leading to potential overall instability.

Most of the HVDC links are connected between two points of a single AC system or two separate AC systems. These are commonly known as point-to-point HVDC links. There are only two exceptions around the world, where the HVDC system has more than two points of connection to the AC system, which is referred to as MT-HVDC systems. Incidentally, both multi-terminal links in operation "Sardinia-Corsica-Italy" link and "Quebec-New England" link work with power flowing through the DC link from a generation center (e.g., the hydropower from James Bay region in the north of Quebec province) to a main load center (e.g., Boston area and parts of New England) with another intermediate load center (e.g., Montreal region) on the way. However, unlike a meshed interconnected AC network, a truly meshed HVDC grid is yet to be realized in practice. For overhead lines, HVDC is cost-effective only at large transmission distances (e.g., above 600 km) at which level meshed interconnections are not economically justifiable. For underground or subsea cable transmission, the distance beyond which DC technology is effective is much shorter. This has resulted in a number of point-to-point interconnections between AC systems separated by sea to allow the exchange of cost-effective electricity. With the increased penetration of intermittent renewable energy sources (e.g., wind power) and high-voltage charging stations, balancing the supply and demand is likely to be a major problem. To ensure reliable operation of the system, there is a growing need for meshed interconnection to effectively share the diverse portfolio of renewable energy resources and thereby increase operational flexibility. For instance, in Europe, the hydropower from Norway and solar power in Spain and Portugal could be utilized when the wind is not blowing in the UK or mainland Europe and vice versa. There are several visions for an offshore grid in Europe. One aspect in common with all such visions is that several DC links are connected at a single point, forming a DC grid. Because of the subsea transmission distances involved, the only viable option is to use DC, which essentially calls for an MT-HVDC or meshed grid. In such a meshed DC grid, the PF in the DC links

would have to reverse frequently depending on the geographical distribution of renewable generation and the electricity price differential at a given point in time. The VSC technology allows such PF reversals without altering the DC voltage polarity and is, therefore, the only option for a meshed DC grid. On the other hand, Line-Commutated Converters (LCCs) rely on reversing voltage polarity to change the PF direction which is not a problem for a point-to-point link but does not support a meshed grid operation without physical isolation. The situation is different from the two multi-terminal links in operation today where PF is substantially unidirectional (from generation to load centers). Hence, they work with LCC technology, which was the only available option anyway at the time of installation of these systems.

The MT-HVDC systems require to be fully analyzed and controlled before using in the practical projects. Although numerous research studies are done in analysis, control, operations, and protection of MT-HVDC system, there are still many research points which need deep understating and investigation, such as:

# CONTRIBUTIONS

The main contributions of this thesis based on each chapter are as follows:

**Chapter 2:**

- A precise bidirectional charging control strategy of PHEVs in power grids to simultaneously regulate the voltage and frequency, as well as reducing the peak load, and improving the power quality by considering the SoC and available active power in power grids is proposed.

**Chapter 3:**

- To contribute the MT-HVDC system to the grid regulation, a generalized model of MT-HVDC systems topology and the steady-state interaction among MT-HVDC system and AC grids are investigated.
- A communication-free and improved droop-based controller is proposed to enforce the stability of the DC grid, and allow the MT-HVDC systems to participate in the grid regulation. A new strategy to control active and reactive power flow using the AC voltage-droop, DC voltage-droop, and frequency-droop controllers is proposed to manage the operational constraints of the hybrid AC/DC grids. Moreover, an optimal tuning strategy is investigated to either optimize the controllers' response time with the aim of enhancing the cut-off frequency or improve the system stability with the aim of less damping oscillation and overshoot percentage.
- Because of the nonlinear behavior of the MT-HVDC system, the corresponding parameters of the controllers of the VSC-HVDC stations in a decentralized structure are tuned to mitigate any changes in the frequency, AC voltage, and DC voltage and consequently, balance the instantaneous power share in the MT-HVDC system.

**Chapter 4:**

- To address all the challenges of unified and sequential AC/DC PF and considering the droop parameters, a mixed AC/DC PF algorithm for MT-HVDC systems is proposed in this chapter. The proposed strategy is a fast and accurate method, which is capable of optimizing the AC/DC PF calculations. Except for the high accuracy and optimized performance, considering all operational constraints and control objectives of the integration of MT-HVDC systems into the large-scale AC grids is the other contribution of this chapter.

**Chapter 5:**

- A new topology of Hybrid DC Circuit Breaker (HDCCB) for MT-HVDC systems with capabilities of reclosing and rebreaking, as well as bidirectional fault current interruption is proposed. The proposed topology of the HDCCB is based on the switching technique to minimize the costs of implementation and on-state switching losses, as well as interrupting the fault current in both directions. Also, in this topology, the polarity of the capacitor is based on the direction of fault current, which would lead to reducing the interruption time. Hence, it can be used in MT-HVDC systems.
- The proposed topology has reclosing and rebreaking capabilities without the need for an external power supply, which leads to reducing the overall cost.
- Improving the fault tolerance capability by increasing the maximum breaking current 0.25% compared to the conventional HDCCB, while having approximately the same total dissipated energy of the surge arrestor in the DC CB, and clearing the fault in 16 ms.
- The proposed topology limits the rate of rise of the voltage across the DC CB, reduces the on-state switching losses, and ensures an equal

voltage distribution regardless of tolerances in the switching characteristics.

- The proposed topology can improve the overall performance of MT-HVDC systems and increase the reliability of the DC grids.

# CHAPTER 1

## *Introduction*

### *1.1. Motivation*

The rapid increase in energy demand, destruction of the earth's resources, and discharge of carbon dioxide are the leading causes of environmental pollution and climate change in the world. Further, transportation is more attentive, considering the fact that it causes more than 15% of carbon dioxide discharge, which is critical for all the people [1-2]. As a result of that, the transition from the Internal Combustion Engine (ICE) to hybrid and full-electric vehicles has been an immense focus for the reduction of greenhouse gases [2]. Due to pollution and energy crisis, many studies in the field of Electric-Drive Vehicles (EDVs), including Battery Electric Vehicles (BEVs), Hybrid Electric Vehicles (HEVs), and Plug-in Hybrid Electric Vehicles (PHEVs) have appeared worldwide [2-4]. However, developments in the field of electric vehicles are restricted by the technology of the batteries and Energy Storage Systems (ESSs), there are many positive signs of progress in this field [5-7]. A good number of alternative energy sources, which are renewable, are already being harnessed and utilized to meet the energy demand in the world [8-9].

The arbitrary connection of PHEVs to the power grid leads to the complicated operation, planning, and control of the power system. There are different charging mechanisms for PHEVs to be charged. IEC Std. 61851 is one of the common standards, which is established for PHEVs charging [8]. Regardless of the charging mechanism, the availability of charging stations is an essential factor that should be considered for power systems control, operation, and long-term planning. The common and low-cost procedure for charging PHEVs is slow charging, which drains less power from the grid. However, the main drawback of this mechanism is that it takes more time to fully charge the batteries of PHEVs. On the other hand, the fast charging mechanism, based on the new developments in power electronics devices and restructuring both of both ESSs and chargers, can expedite the charging process and charge a depleted battery from 10 to 80 percent in half an hour [10]. However, this mechanism drains more current at a high voltage

level from the network and has a negative effect on the other loads connected to the same bus, e.g., the voltage drop at the end of the power line.

In modern power systems, microgrids are defined as interconnected local energy centers with control and management capabilities and clear boundaries. They enable bidirectional and autonomous power exchange to prevent power outage by providing high-quality operation and more reliable energy supply to the load centers. Aging electric power grid infrastructures, continuous increase in the load demand, integration of renewable energy resources and electric vehicles, transmission power losses, and improving the efficiency of power systems, are several challenges in modern power systems. Therefore, to overcome the mentioned challenges, macro and micro-grids are utilized to both enhance the power quality and increase the reliability of the grid side and the load side. There are several studies in the field of microgrids, considering their different manifestations, such as Smart Grids (SGs) and Virtual Power Plants (VPPs), etc. [11]. One of the main concerns in modern power systems analysis is the dependency on the power from microgrids by using the grid power along with their developments. As a result, microgrids can interconnect to the power grid and improve the power quality and reliability. From another perspective, microgrids can connect to/disconnect from power grids to enable themselves and operate in both grid-connected and islanding modes.

Based on the expansion of the interconnected power grids through the long transmission lines, increasing the load demand, and the need for a supervisory control system for the power generation units, electric utilities are moving toward the decentralized and deregulated power systems, focusing on independent microgrids. Non-traditional power generation sources (e.g., wind farms, solar power plants, diesel generators, etc.) in microgrids are allowed to trade electricity with the local consumers. In addition, microgrids in a centralized structure no longer rely on a single power source. On-site generations can be utilized as emergency backups in the event of blackout or load shedding to mitigate disturbances and increase power systems reliability. Figure 1.1 illustrates the concept of modern microgrids. As shown, there are several ways to utilize Distributed Generations (DGs), such as wind, solar, ESSs, etc. in the power system to support the grid and supply the load demand.

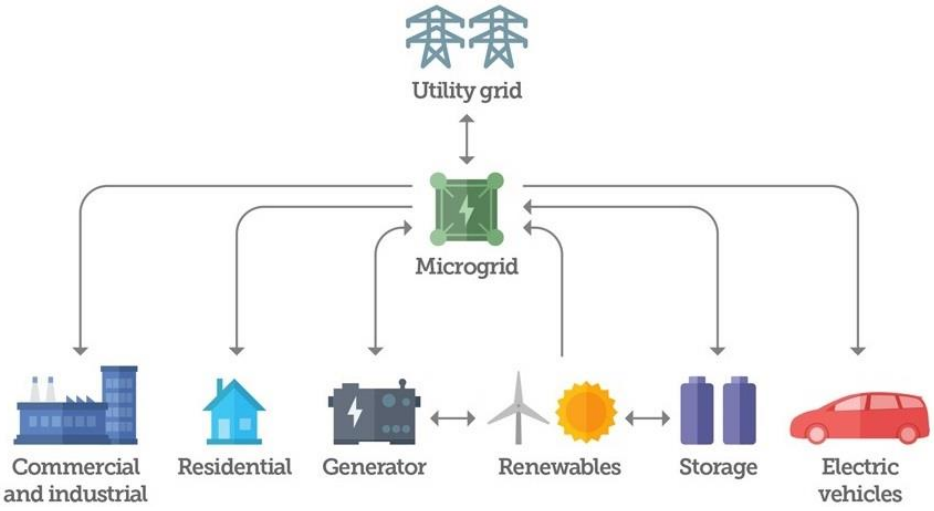


**Figure 1.1.** The concept of modern microgrids

### *1.2. Literature Survey*

#### *1.2.1. Impact of Charging Station on Power Grids*

Technically, modern microgrids are a small part of low voltage distribution networks that are located far from the substation and interconnected through a Point of Common Coupling (PCC) [12]. Based on the nature of microgrids operation (e.g., ownership, location, reliability requirements, and trading purposes), significant developments are carried out by researchers, industrial and commercial factories, and military bases. According to the Power and Utilities Navigant Research, the capacity of the global microgrid has been projected to grow from 1.4 GW in 2015 to 7.6 GW in 2024 under a base scenario [12]. Modern microgrids not only offer great promises owing to their significant benefits but also result in tremendous technical challenges. There is an urgent need to investigate the state-of-art control and energy management systems in microgrids.

One of the main challenges in microgrids technology is to manage and balance the generation and consumption of energy [13]. The power imbalance is a typical scenario in microgrids, which comes from the nature and availability of renewable energy resources to discontinuously generate power and available loads connected to microgrids. The control system should manage these imbalances to prevent electrical damage and maintain both AC and DC grids stable [14-17]. As a result, recent studies have focused on proper

power management and control strategies to manage the generation and consumption of energy. These control strategies are mainly targeted at: (i) controlling the interconnected DGs and ESSs, (ii) DC bus voltage regulation, (iii) minimizing the cost of imported/exported energy from/to the main grid by optimizing the power dispatch between converters and DC bus voltage, (iv) management, and optimization of ESSs operation, and (v) current sharing management between parallel converters in DC grids [17-20].

In order to optimize the power dispatch, proper communication infrastructure between the microgrids and the grid operator are required [21-22]. However, real-time simulation and monitoring can be implemented by the communication infrastructure, the outage of the communication links/signals can cause many complicated problems. The droop control method is a well-known strategy to maintain the power balance in DC microgrids [17, 22-26], which does not require communication infrastructure [17]. The power management of microgrids can be classified into centralized, decentralized, and distributed control categories [25-29]. The energy dispatched in the centralized control systems can be monitored and managed by an intelligent centralized (master) controller, which receives and analyzes the data, manages the power among the converter stations under operation, and forecasts the power and voltage references to all the power devices of the microgrids. [30-31]. These systems usually offer precise power-sharing among converters in microgrids [28-29]. In case of loss or outage of the master controller, local autonomous controllers (decentralized structure) are needed to fulfill the master controller failure [32-35]. In a distributed control system, each microgrid is allowed to only communicate with its nearby neighbors. Therefore, there is still a need for communication infrastructure. Further, there are many loops in a distributed control system, which make its design more complicated [36].

However, installing new components and/or upgrading the existing components are two methods to overcome the negative impacts of PHEVs in power grids, high investment costs prevent the mentioned solutions to be implemented. If the high penetration level of PHEVs is connected to the system, up to a 15% increase in the cost of upgrading the existing grid to guarantee the adequacy of the power system can be expected [37]. Therefore, more investigations are required to find a suitable and cost-effective solution.

Utilizing proper ESSs and appropriate charging/discharging mechanism to control the Power Flow (PF) in PHEVs are preferable to installing new components and/or upgrading the existing infrastructures in power grids. High penetration chargers can be designed and implemented to allow bidirectional PF between ESSs and power grids.

PHEVs can assist in improving the load-leveling profile and reducing power losses [38]. Further, utilizing efficient Voltage-Sourced Converters (VSCs) in power system allows transferring reactive power, as well as active power into the power grid. The DC-link capacitor and a proper switching mechanism can improve the quality of the transferred power into the grid [39]. Therefore, several studies have investigated different control strategies to implement the concept of a bidirectional charger and solve the charging issues of PHEVs [40-43].

A practical power electronics grid interface that can provide the Vehicle-to-Grid (V2G) bidirectional PF with a high power quality is necessary to perform the grid-connected vehicle battery application. This interface should respond to the charge/discharge commands that are received from the monitoring system to enhance the reliability of the power grid. Moreover, essential requirements, such as reactive power injection and tracking the reference charge/discharge power, should be met [44-45]. A comprehensive review of the bidirectional converters is presented in [46], and discusses their advantages and disadvantages. In [47], the energy efficiency in PHEV charges along with the evaluation and comparison of the AC/DC topologies, such as the conventional Power Factor Correction (PFC) boost converter, including a diode-bridge rectifier followed by a boost converter, an interleaved PFC boost inverter, a bridgeless PFC boost converter, a phase-shifted semi bridges PFC boost converter [48], and a bridgeless interleaved boost converter [49] is presented. In addition, some non-inverted topologies are presented in [50-60], some of which require two or more switches to be operated in Pulse Width Modulation (PWM) mode, which causes higher total switching losses [50-52, 54-61]. However, bidirectional PF cannot be achieved in the topologies of [50, 54, 57, 61-64].

Different DC charging station architectures for PHEVs are proposed in [65-67]. For instance, the control of the individual EV charging processes introduced in [65] is decentralized, while a separate central supervisory system controls the power transfer from

the power grid to the DC link. With sufficient energy stored in the battery of PHEVs, the bidirectional charging/discharging power control of PHEVs can be applied to reduce the frequency fluctuation [68-74]. A power charging control system to control the frequency in the interconnected power system with wind farms is considered in [68]. The controller in [68] is capable of stabilizing the system frequency during the charging period. Further, the bidirectional power control of PHEV applied for frequency control in the interconnected power systems with wind farms is proposed in [69]. The proportional-based PHEV power controller in [69] provides satisfactorily control, but its performance may not tolerate such uncertainties, and it may fail to handle the system frequency fluctuation.

Further, the system parameters may not remain constant and continuously change when operating conditions vary [75]. The system parameter variations, such as the inertia constant and damping ratio, are conventionally considered to check the performance and robustness in the Load Frequency Control (LFC) approach [76]. Hence, the robustness of the controller against system uncertainties is a vital factor that must be considered.

### *1.2.2. Control of MT-HVDC Systems*

For long-distance transmission, Multi-Terminal High Voltage Direct Current (MT-HVDC) grids are utilized to transfer the generated power from offshore AC sources, e.g., wind farms, to onshore AC grids. The delivered power can be shared by the onshore AC grids with the aim of maintaining the DC voltage within a certain range at all the system buses. The power-sharing strategy depends on several objectives, such as power losses minimization, sharing ratio, and priority order [79]. Power-sharing and voltage control in MT-HVDC systems are the major challenges especially for the control and operation of the power system while it faces an outage [80-81]. Significant research studies are conducted on MT-HVDC system modeling [82-84, 86-94] and control [85, 95-102].

In hybrid AC/DC grids, two parameters should be considered: (1) The DC voltage at different buses for the DC grids to share the power. (2) The frequency for the AC grids to minimize the deviations in power, and among the other interconnected AC grids. There are several methods to perform the operation of power-sharing control and frequency and voltage regulation [95-96, 98-101]. These control strategies can be classified into two main

categories: (1) Master-Slave technique and (2) Distributed DC voltage control strategy. In terms of sub-categories, both of them can be classified into centralized and decentralized control methods.

#### *1.2.2.1. Master-Slave Technique*

In order to control the DC voltage in MT-HVDC systems, the active power should be controlled considering one converter as the slack converter, while the other converters are controlling the active power at a constant level. The slack converter can control the DC voltage using the outer loop in the DC voltage controller. By performing the Optimal Power Flow (OPF) at different buses, the $P_{ref}$ setting for all the other converters can be calculated in the master converter. To ensure the operation within the acceptable limits of the converter, the master converter must be oversized and it needs a larger power rating. Moreover, a fast communication infrastructure between different nodes is required to improve the reliability of both AC and DC grids [80, 103-104]. In order to prevent the voltage of the entire system from violating the limits, the reference value for the DC voltage in the master converter should be defined [107]. The master-slave technique has some drawbacks, which are mentioned as follows [103-109]:

- A high-speed communication infrastructure is required.
- Regulating voltage through the entire AC and DC grids is complicated through one converter.
- The outage of mater converter leads to DC over-voltage or under-voltage, and consequently collapse of the entire DC grids.

Figure 1.2 shows the active power-DC voltage ($P - V_{DC}$) characteristics of a typical master-slave controller.

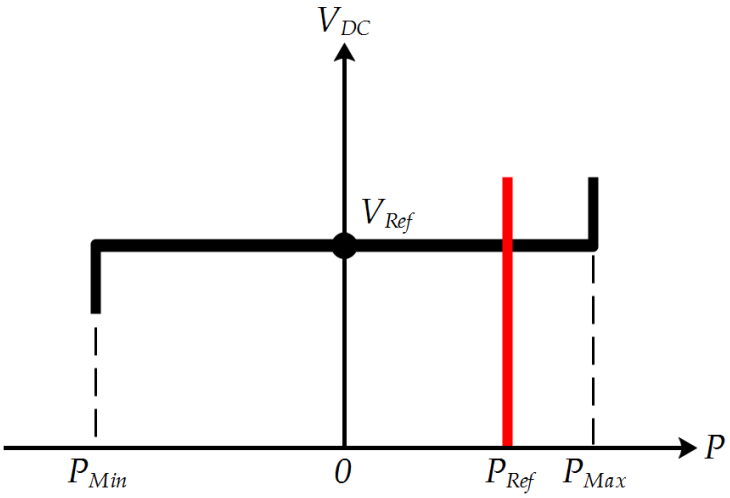


**Figure 1.2.** $P - V_{DC}$ characteristics of (black) the master converter and (red) the slaves

In [110], a communication-free DC voltage control strategy for MT-HVDC systems is proposed. The configuration of the system is based on a grid-side master converter and a wind farm to incorporate and maintain the DC-link voltage in its acceptable range, as well as providing frequency support and improving the power dispatch. The control strategy uses the DC-link voltage at the master converter and maintains the wind power reserve. As a result, the wind farm can participate in the DC-link voltage control without the need for the communication infrastructure. The main drawback of this control strategy is that the outage/contingency at the master converter can cause instability of the entire hybrid AC/DC grids. In addition, since the other converters are injecting power to the MT-HVDC systems, AC/DC grids experience with surplus/deficit injected power, and consequently, the DC voltage increases/decreases drastically. N-1 converter security analysis can improve the reliability of both AC and DC grids.

To overcome the dependency of high-speed communication infrastructure and improve the reliability of the hybrid AC/DC grids, the voltage margin method and voltage droop-based control method are proposed. The voltage margin method is a modified version of the master-slave technique to tackle the N-1 security problem and control the voltage through the voltage and active power of different converters in MT-HVDC systems [111-116]. The main drawbacks of this method are the complexity in terms of controlling several parameters and the large oscillations of PF due to the sudden changes in the DC voltage [96]. In MT-HVDC systems, two or more converters are equipped with the DC

voltage-droop controller to improve the reliability of the hybrid AC/DC grids. The rest of the local terminals can operate in a constant power control mode. If any changes in the DC voltage are detected by a converter equipped with DC voltage droop-based controller, this controller can generate adequate deviation of $P_{ref}$ of the converter and support the power balance on the DC grids and reduce the large DC voltage oscillations [85-86, 117-118]. In practice, a high-accuracy of power balance in AC off-shore and on-shore AC system is mandatory. Hence, the droop parameters should be optimized according to the DC voltage changes [119]. In addition, the frequency changes generate adequate power deviation response of the converter and modify $P_{ref}$ [95, 117, 119-123]. However, a global frequency-droop control strategy of the MT-HVDC system is required. In [123], a control strategy is proposed to emulate the pattern of the conventional AC generators when participating in the frequency regulation. The proposed frequency-droop control strategy can enable/disable different control loops, but it negates the action of any possible voltage-droop controller.

#### *1.2.2.2. Distributed DC Voltage Control Strategies*

To improve the stability of the hybrid AC/DC grids, as well as increasing the accuracy of balancing the power, the distributed DC voltage control strategies, such as distributed direct DC voltage control and adaptive droop-based control are investigated. In these two techniques, a PI controller on the slack bus combines with the other PI controllers on the different local buses, and regulates the DC voltage. By utilizing the communication infrastructure, the control parameters and reference values can be computed frequently and sent to a centralized supervisory controller, and then, sent to the other local converters.

##### *1.2.2.2.1. Distributed Direct DC Voltage Control Strategy*

Several research studies related to the distributed direct DC voltage control method are carried out [96, 101, 112, 124-128]. Therefore, different OPF algorithms are proposed to minimize the losses and determine the reference value for the DC voltage of local direct DC voltage-controlled converters without the need for communication infrastructure. Also, to analyze the operation of the power system, the proposed OPF techniques are used to study the contingency in one of the direct DC voltage-controlled converters and tackle the

N-1 security problem. Considering the uncertainty in the generated power by the off-shore AC systems interconnected with the MT-HVDC systems to the power grids and the line resistance can reduce the accuracy of the OPF. Moreover, due to the direct relationship between the line resistance and the power balance and DC voltage, by losing the communication connections for a long time, the DC voltage deviations increase and it can cause instability of the entire hybrid AC/DC grids. As a result, protective equipment, such as dump resistors are required to prevent the excessive increase in the DC voltage level. As a matter of fact, the distributed direct DC voltage control is suitable for the AC grids, where no single power station is left alone to guarantee the stability of the system [124].

#### *1.2.2.2.2. Adaptive Droop-Based Control Strategy*

The droop control strategy for MT-HVDC system can operate as in traditional AC grids, where the load-dependent frequency deviations can be used as an input signal for the control system and adjust the generated power to meet the demand [129-130]. An adaptive droop-based control strategy is a promising solution due to the disadvantage of distributed direct DC voltage control method to lose communication connections for a long time and lose the stability of the hybrid AC/DC grids.

##### *1.2.2.2.2.1. Adaptive Power and DC Voltage Droop-Based Control Strategy*

In MT-HVDC systems, the control system employs the droop setting to regulate the DC voltage within the system by adjusting the converter current in such a way that power balance is guaranteed [131-134]. The defined gain of the adaptive power and DC voltage droop-based controller can reduce the sensitivity of power balance to the line resistance, improve the accuracy of the OPF, and simultaneously, regulate the DC voltage. In addition, the corresponding parameters of the adaptive droop-based controller can be optimized for different operation objectives. In [134], a methodology to calculate the droop parameters of the droop-based converter to minimize the power losses in transmission lines in off-shore AC systems interconnected with the MT-HVDC systems is proposed. The main drawback of this method is its complexity to be applied to the ring or meshed grids [134]. In [106], the droop parameters of the droop-based converter are calculated in such a way that a certain power-sharing ratio between converters at contestant no-load voltage is

achieved. However, the proposed method cannot be applied to the ring or meshed grids. In [85-86], a droop-based control method for the MT-HVDC systems in a decentralized operation is proposed. But, the main drawback of the proposed droop-based control method is the fact that the sensitivity of power balance depends on the line resistance and it can cause inaccuracy of the OPF calculations. Increasing the voltage level in hybrid AC/DC grids with the aim of minimizing the transmission lines losses can lead to an increase in the converter losses. In order to minimize the transmission lines and converter losses, an OPF method to select the optimal reference values considering the fixed droop parameter for the DC voltage of the droop-based converter is proposed in [126]. Supporting energy adequacy, increasing off-shore AC system penetration, and maximizing converter loadability, as well as minimizing total losses, are the major priorities in the MT-HVDC system analysis. Another priority is the impact of droop parameters on the accuracy of the power balance and DC voltage dynamics [131-132]. Optimal DC voltage dynamics without violating the defined constraints is an important factor in the power balance which is considered in [109, 128, 131] in such a way that the droop parameters are selected by multiplying the local droop parameters by a multiplier. The accuracy of the power balance is the main drawback of the previous methodologies. Each converter has a particular available headroom to participate more in the DC voltage control. In [133], the available headroom of each converter is used to analyze the droop parameters and it is replaced with the new operating points after each contingency to improve the stability of the hybrid AC/DC grids. The droop-based controllers' parameters are selected optimally due to the sudden change in the reference values in [135]. The main drawback of this research study is neglecting power-sharing control.

#### *1.2.2.2.2.2. Adaptive Frequency and DC Voltage Droop-Based Control Strategy*

In modern power systems, the significant contribution of DG resources in the electricity generation and PHEVs in the load consumption are increasing gradually. Previously, the DG resources could not participate in the frequency regulation of AC grids the same as the conventional AC generators. Therefore, in order to participate in frequency regulation, a primary reserve sharing between AC grids and the candidate AC/DC converters is an important concern [117, 121]. Using the frequency-droop based controller,

the AC/DC converters can participate in the primary frequency regulation of the AC grids [95, 120-122]. The deviation in power caused by the frequency-droop controller of the converter should adopt the standards of the power grids and it should be matched with the accurate values of the frequency deviation of the AC grids. The DC voltage-droop based controllers can be a solution to enforce the stability of the DC grid by optimizing voltage-droop controllers' parameters, as well as regulating the DC voltage and balance the power. On the large-scale MT-HVDC system, optimizing frequency-droop based controllers' parameters can adjust the frequency deviations and allow the MT-HVDC system to participate in the frequency regulation of the different AC system interconnected by the DC grids. A control methodology to support the frequency of the system through the MT-HVDC systems by calculating the eigenvalues of the hybrid AC/DC grids is proposed in [120]. In [22], the dead-band control is utilized for both frequency and DC voltage droop-based controllers. However, in both [22] and [120], the interactions among the frequency and DC voltage droop-based controllers are not considered. In [95], the primary frequency control of remote grids connected by MT-HVDC systems is studied to control the frequency-droop parameters and comply with the desired value for the predefined frequency deviation. An analytical methodology of the interactions among AC and DC grids is performed in [121] to utilize the frequency and DC voltage droop-based controllers and modify either the DC voltage dynamics or the frequency deviations. The same study as [121] is conducted in [117] with the aim of determining the interactions among DC voltage droop-based controller, to comply with the maximum DC voltage deviation constraints, and frequency-droop controller to allow the HVDC system to participate in the frequency regulation of AC grid. In [122], the interactions between frequency and DC voltage droop-based controllers through the evolution pattern of the frequency of each AC grids is studied. However, the correction of droop parameters to minimize the deviations in DC voltage and frequency is disregarded.

### *1.2.3. AC/DC Power Flow for MT-HVDC Systems*

Due to the recent developments in the power electronics technology, Voltage-Sourced Converter (VSC)-High Voltage Direct Current (HVDC) systems have solved the problem of bidirectional PF in hybrid AC/DC grids [136-138]. MT-HVDC systems are

capable of controlling the active and reactive power, independently. One of the important considerations to control the HVDC systems is that the $V_{DC}$-control and $P$-control VSC-HVDC stations should be capable of operating in inverter and rectifier modes, respectively [139-141]. Changing the control mode from $V_{DC}$-control to $P$-control leads to changing the direction of PF. The main purpose of applying different control strategies in MT-HVDC systems is to achieve a precise and secure control mode for the MT-HVDC systems without violating the constraints. For stable operation and active and reactive PF, MT-HVDC systems need to maintain the DC voltage and frequency within the operating limits [136-139].

In the past decades, there have been some relevant surveys about power system operation considering PF problem solutions [142-143]. In traditional AC system, the PF can be controlled through three hierarchical levels which are, HL I (generation level), HL II (generation and transmission levels), and HL III (generation, transmission, and distribution levels). Considering hierarchical levels and the market analysis, the Independent Electricity System Operator (IESO) can only control the generated power on the power system, and based on that, control the PF to the next hierarchical level(s). The integration of MT-HVDC systems to the existing AC grids leads to increasing the region of controllability of hybrid AC/DC grids. This fact is due to the capability of controlling active and reactive PF by each converter in MT-HVDC systems [136, 139, 144]. Therefore, MT-HVDC systems can change the PF patterns, and from the IESO and Transmission System Operator (TSO) perspectives, these changes in the pattern may cause significant issues in hybrid AC/DC grids. Moreover, due to the temporary or permanent outages of the components in hybrid AC/DC grids, the dynamic behavior of nonlinear components can change the PF and enhance the risk of instability in the entire hybrid AC/DC grids [144-145].

#### *1.2.3.1. Solving the Power Flow Problem for MT-HVDC Systems*

The unified method and sequential method are the two well-known methods to solve the PF problem for MT-HVDC systems.

#### *1.2.3.1.1. The Unified Method*

The unified method solves the PF problem for the entire hybrid AC/DC grids using a modified Jacobian matrix [146-148], where all the AC and DC variables, such as the impact of DC links in the Jacobian matrix, can be calculated in each iteration process. Many techniques are proposed and developed to improve the efficiency of the unified method, but the main drawback of those methods is neglecting the impact of droop parameters' settings on the AC/DC PF [146-148]. Another issue of the unified method to solve the PF problem is that it needs an alternation of the extension of an existing AC PF.

#### *1.2.3.1.2. The Sequential Method*

The sequential method solves the AC/DC PF equations sequentially, one after another in each iteration [149-150]. The main advantage of the sequential method is to make the solution easy to combine the DC PF to the AC PF solution technique, and it can be implemented easily when the extension of an existing AC PF is needed. In [151], a numerical method based on the Newton-Raphson algorithm to calculate the converter losses using the unified approach by iterations is proposed. A detailed steady-state model of the converter station to solve the AC/DC PF problem sequentially based on the Newton-Raphson technique considering converter losses and reference power is proposed in [152-153]. An algorithm with per-unit conversion and changing the bus numbers to simplify solving the PF problem when multiple DC lines and converters outages occur is developed in [152]. The main drawback of this method is neglecting the AC grid connection in the problem. In [154], a detailed model of the converter station with AC/DC PF equations, including converter losses, for solving the PF sequentially is proposed. In [155], a method to solve the PF problem through the Gauss-Seidel method is developed.

### *1.2.3.2. AC/DC Power Flow for MT-HVDC Systems Considering Droop Parameters*

Controlling the droop parameters in MT-HVDC systems has a significant impact on the PF of AC and DC grids after an outage [139]. In [156], the concept of distributed DC voltage control with the droop parameters on the PF problem in MT-HVDC systems

is considered. In [157], a methodology to determine the mean voltage instead of a single slack converter in MT-HVDC systems to solve the DC PF is proposed. By interconnecting MT-HVDC systems to the large-scale AC grids, solving the AC/DC PF goes through a complicated process, and a combined solution of AC/DC PF considering all the system variables and constraints is required.

### *1.2.4. Protection of MT-HVDC Systems*

Protection of the MT-HVDC grids in case of a DC fault is vital to improve the reliability of the power system [145, 158]. Conventional Voltage Sourced Converters (VSCs) are not capable of limiting or interrupting the current that flows following a DC-side fault. Also, the high power DC Circuit Breakers (CBs) are not commercially available. Therefore, opening the CB on the AC side is the only possible way to isolate the DC-side fault. Opening all the AC CBs to isolate/clear the DC-side fault in a DC grid with high capacity can lead to a large loss of power infeed. Therefore, clearing the DC fault within the DC grid by opening the AC CBs is practically impossible [158-160].

The consequence of a DC-side fault within an MT-HVDC grid is the sudden increase in the fault current, and that is due to the capacitive behavior of the HVDC grids and low resistance of the DC cables. The fault current should be interrupted in less than 20 ms to limit it within the acceptable levels [161]. Using AC-side CB in the point-to-point VSC-HVDC grids to interrupt the fault current leads to loss of the entire link. Adopting the same strategy for MT-HVDC grids and opening all the AC-side CBs is a disruptive measure and can cause losing a large amount of power infeed. Therefore, it is mandatory to isolate only the faulty section of MT-HVDC grids. Two measures can be considered to deal with this issue: (1) Using fast-acting DC CBs at both ends of the DC-links. (2) Using fault-blocking converters to open the DC-links in case of a sudden increase in the DC fault current. Moreover, determining the exact location of the DC-side faults within MT-HVDC grids is difficult [162-163]. In the AC grids, impedance relays are used to determine the fault location. However, due to the low resistance of the DC cables compared to the impedance of the AC grids, it is impractical for the impedance relay to determine the fault location in a DC-link within its protective zone. Besides, distinguishing between the AC and DC-side faults is another major challenge in a DC protection system [164-165].

In order to interrupt the fault current, the AC CBs at the high voltage transmission levels require 4-5 cycles (within 80-100 ms). By creating zero crossings of the current, the AC CBs provide interruption with minimal arcing [166]. As there is no zero crossing of the current in DC, the conventional AC CBs are not useful to prevent large DC currents. To overcome this issue, a passive or active resonant circuit can be used to force the current zero crossing. The other way is to bypass or interrupt the fault current using semiconductor switches (Insulated-Gate Bipolar Transistor (IGBTs)), which considering the power losses, it is an expensive strategy. Due to the lack of reactance in the DC circuits, the rate of rise of fault current in the DC grids is higher than the AC grids [167-168]. Thus, the DC CBs must be capable of interrupting the fault currents faster than the AC CBs.

Different CB topologies are studied in the literature. The CBs can be categorized into three types: Mechanical Circuit Breakers (MCBs), Solid-State Circuit Breakers (SSCBs), and Hybrid Circuit Breakers (HCBs) [169-170]. The MCBs consist of the conventional AC CBs with a parallel circuit to generate a current zero crossing [171]. In both passive and active MCBs structures, due to the existence of the parallel circuit, the interruption time of the MCBs is long (30-50 ms), which is not suitable for VSC-HVDC systems. The SSCBs consist of several solid-state switches that can interrupt the fault current faster than the MCBs without the need for a current zero crossing [172-175]. Proper configuration of switches can lead to achieving the desired breaking current capability. To design a bidirectional CB, at least two switches are needed. The SSCBs are faster compared to the MCBs, but their on-state switching losses and total cost are high. The HCBs configurations are the results of the combination of MCBs and SSCBs [176]. The combinations are based on the operation time, breaking current capability, power losses, and total cost. The operation time and breaking current capability of the MCBs are low, but they are cheap. In contrast, the SSCBs are fast, but when it comes to a complicated configuration for the VSC-HVDC systems, they are expensive. Also, because of the existence of permanent resistance, the SSCBs have large power losses compared to the MCBs. The HCBs take advantage of both MCBs and SSCBs, such as fast current interruption and low power losses [177-178].

The first HCB [178], which was based on inverse voltage generation method, provided the advantages of both MCBs and SSCBs. It consisted of a semiconductor-based CB using IGBTs and a bypass circuit developed by the semiconductor-based load communication switches in series with an ultra-fast disconnector. Reducing the fault current level to zero is achieved by generating the arc voltage at a higher level than the source voltage. This topology has a short interruption time than the MCSs and lower on-state switching losses compared to the SSCBs. A detailed analysis of the operating modes of HCBs (reclosing and rebreaking) is performed in [170]. An accurate model considering the coordinated control of the four subunits (two semiconductor values along with two mechanical switches) and the opening and closing sequences of each subunit of the HCB is presented in [177]. This topology is not suitable for MT-HVDC grids, where the fault location is hard to find, and the switches in the auxiliary CB might damage due to the high rate of rise of current. To overcome this issue, a large number of semiconductor switches in the semiconductor-based CB branch is needed, which can increase the cost of implementation and relatively increase the on-state switching losses. To reduce the on-state switching losses of the HCBs, another topology considering multiple thyristors connected in series is proposed in [179]. In this topology, by injecting current stored in the capacitor with the initial charge, a current zero crossing can be generated. The main issue with this topology is the high on-state switching losses because of the existence of IGBT in the main CB. Moreover, the fault interruption time is increased due to the transferring the fault current from the CB to the auxiliary CB. Besides, using an external power supply to charge the capacitor might lead to an increase in the costs of implementation. This topology provides the bidirectional fault current interruption, but reclosing and rebreaking capabilities of the HCBs is not considered. The topology of the HCBs presented in [180] is provided reclosing and rebreaking capabilities, as well as bidirectional fault current interruption. Reclosing and rebreaking capabilities have prevented the interruption of the power to the connected AC systems, and the auxiliary power source is used to charge the capacitor. Although the polarity of the capacitor can change according to the direction of fault current, it might have delay time to interrupt the fault and consequently, increase of the fault current magnitude.

### *1.3. Outline*

The subsequent chapters of this study are structured as follows:

**Chapter 2** presents a bidirectional charging control strategy for high-voltage charging stations considering the SoC of the batteries of the EVs and simultaneous voltage and frequency regulation in power systems. The main aim of this chapter is to investigate the control the batteries charge which are connected to the grid, and simultaneously regulate the voltage and frequency of the power grid during the charging time based on the available power when different events occur over a 24-hour period.

**Chapter 3** presents an improved droop-based control strategy for the active and reactive power-sharing on the large-scale MT-HVDC systems. As droop parameters enforce the stability of the DC grid, and allow the MT-HVDC systems to participate in the AC voltage and frequency regulation of the different AC systems interconnected by the DC grids, in this chapter, a communication-free control method to optimally select the droop parameters, consisting of AC voltage-droop, DC voltage-droop, and frequency-droop parameters, is investigated to balance the power in MT-HVDC systems and minimize the AC voltage, DC voltage, and frequency deviations.

**Chapter 4** presents a mixed AC/DC PF strategy for MT-HVDC systems considering the operational constraints, such as the voltage range, voltage operating region, total transfer capability, transmission reliability margin, converter power rating, etc. to analyze the steady-state interaction of the large-scale MT-HVDC systems.

**Chapter 5** presents a new topology of a fast proactive Hybrid DC Circuit Breaker (HDCCB) to isolate the DC faults in MT-HVDC grids in case of fault current interruption, along with lowering the conduction losses and lowering the interruption time. Different modes of operation of the proposed topology are presented in detail and tested in a simulation-based system.

**Chapter 6** contains some brief conclusions of this thesis. In addition, the improvements for future works are also provided in this Chapter.

CHAPTER 2

## *A Bidirectional Charging Control Strategy for High-Voltage Charging Stations in Power Systems*

### *2.1. Principles of Bidirectional Power Flow*

Figure 2.1 shows a basic model of a power system consisting of two generators and a transmission line which is connected to two generation buses. In this figure, each bus has its voltage magnitude and phase angle, where $V_1\angle\theta_1$ and $V_2\angle\theta_2$ are the corresponding voltage magnitude and phase angle of buses 1 and 2, respectively. The impedance of the transmission line is $Z\angle\gamma$, where:

$$Z = R + jX \tag{2-1}$$

and,

$$\gamma = tan^{-1}\frac{X}{R} \tag{2-2}$$

Therefore, by considering voltage magnitude and phase angle differences between buses, the active power, $P$, and reactive power, $Q$, can be transferred, bidirectionally. In order to study the bidirectional power flow, it should be assumed that both buses are capable of supplying and absorbing active and reactive power.

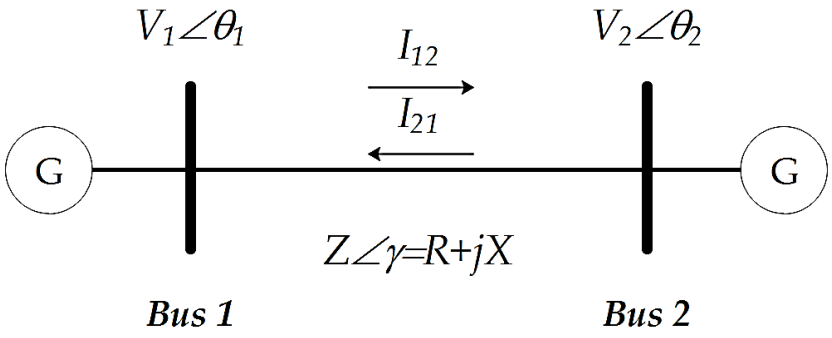


**Figure 2.1.** Single diagram of a two-bus system

Based on the direction of power flow, the active and reactive power equations can be written as:

$$P_{12} = \frac{|V_1^2|}{|Z|} cos\,\gamma - \frac{|V_1||V_2|}{|Z|} cos(\gamma + \theta_1 - \theta_2) \quad (2\text{-}3)$$

$$Q_{12} = \frac{|V_1^2|}{|Z|} sin\,\gamma - \frac{|V_1||V_2|}{|Z|} sin(\gamma + \theta_1 - \theta_2) \quad (2\text{-}4)$$

Assuming $X \gg R$, Equations (2-3) and (2-4) can be re-written as:

$$P_{12} = \frac{|V_1||V_2|}{X} sin(\theta_1 - \theta_2) \quad (2\text{-}5)$$

$$Q_{12} = \frac{|V_1|}{X}[|V_1| - |V_2|cos(\theta_1 - \theta_2)] \quad (2\text{-}6)$$

Small changes in the voltage magnitude have a direct impact on the reactive power flow, while deviations in phase angle can change the active power flow in power grids. If $\theta_1 > \theta_2$, the active power can be transferred from bus 1 to bus 2 and vice versa. Further, if $V_1 > V_2$, the reactive power can be transferred from bus 1 to bus 2 and vice versa. Therefore, the voltage magnitude and phase angle play the important roles in power transfer in power grids.

### *2.2. Control Strategy and Power System Modeling*

#### *2.2.1. Bidirectional Charging Station*

PHEV chargers should be installed off-board and onboard in a vehicle. Onboard chargers are built with a small size, low power rating, and can be used based on a slow charging mechanism. Off-board PHEV chargers are located at specific places and provide either a slow or fast charging mechanism. As a result, charging networks play an important role to support PHEVs. In addition, there are two common architectures (series and parallel) in the PHEV drivetrain. Moreover, a combination of these two (series-parallel architecture) is also used in some vehicles [1, 5-8, 77]. This chapter has considered a generic aggregation of PHEVs with different charging profiles. The number of vehicles in charge, the rated power and rated capacity, and the power converter efficiency are the

important factors in this model. This model is also capable of enabling vehicles to the grid, instantly. Table 2.1 shows the charging station specifications.

**Table 2.1.** Charging station specifications

| Parameter | Descriptions |
|---|---|
| Rated Power | 40 kW |
| Rated Capacity | 85 kWh |
| Rated Voltage | 50-600 $V_{DC}$ |
| System Efficiency | 90% |
| No. of cars (different profile) | 35, 25, 10, 20, 10 |

The fundamental configuration of the charging station consists of a centralized AC/DC converter and different DC/DC converters as the charging lots. The AC/DC converter rectifies the three-phase AC input signal into a DC output signal. DC/DC converters have been used to regulate and shift the output signal to the desired level. A bidirectional charging station is capable of controlling the power flow in both directions between charging stations and power grids.

Figure 2.2 illustrates the single-line diagram of the case study in this chapter [78]. Further, the proposed scheme of the grid-connected PHEV system is illustrated in this figure. The proposed model has a central AC/DC VSC station and different controllable DC/DC converters based on a certain number of PHEVs. All DC/DC converters are in a parallel architecture and are connected to a common DC bus, which has been regulated by the central AC/DC VSC station. Two different conditions have been assumed for the charging stations: (1) cars in regulation, which contribute to the grid regulation; and (2) cars in charge, which are regularly in the charging process. Therefore, there are two modes of operation for each PHEV: (1) regulation mode; and (2) charging mode.

In order to minimize the output harmonics during the operation and switching processes of converters, an RL filter has been considered between the charging station and power grid. The charging system proposed in this chapter allows transferring the active and reactive power bidirectionally with the help of a control system. The control strategy mainly focuses on the AC/DC and DC/DC converters. By proper controlling the central AC/DC VSC station, injecting reactive power into the power grid to regulate the voltage, improving the power factor, and maintaining a constant DC-bus voltage, can be achieved.

Moreover, an appropriate control mechanism for the DC/DC converters can ensure controlling the charging and discharging processes of PHEVs. This chapter has considered both charging and discharging operations, where the DC/DC converters are controlled by charge/discharge PHEV batteries.

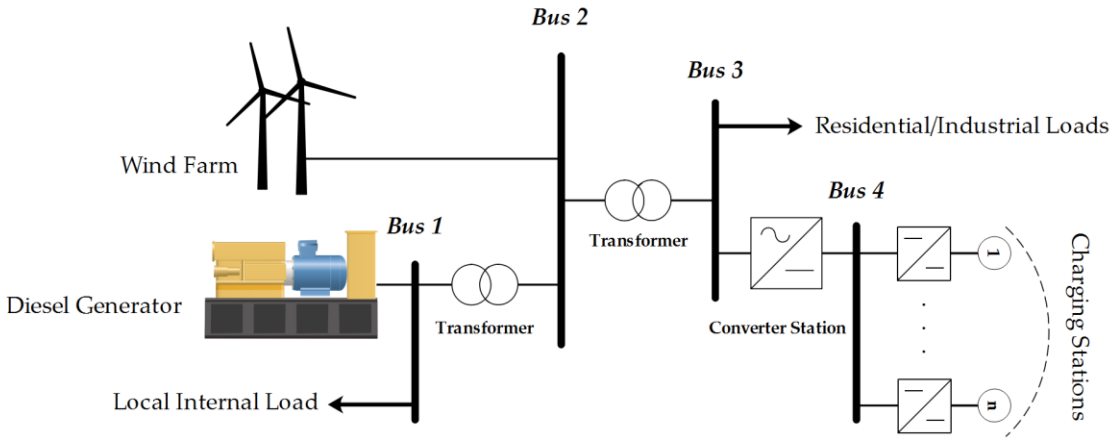


**Figure 2.2.** Single line scheme of the modified microgrid system (case study)

### *2.2.2. Converter Station Control Systems*

As stated in Section 2.2.1, the converter station can work in two modes: (1) the regulation mode, and (2) the charge mode, and is capable of compensating reactive power, and consequently, regulating the voltage of the power grid during the charging and discharging processes of PHEVs. This section provides details of the control systems of the converter station in different modes.

#### *2.2.2.1. Grid Regulation Mode*

In order to contribute to the grid regulation, two controllers have been designed: (1) a grid regulation controller, and (2) a grid regulation power generation. Figure 2.3 shows the grid regulation controller scheme. This controller is fed by the maximum regulated active power, $P_{max\_reg}$.

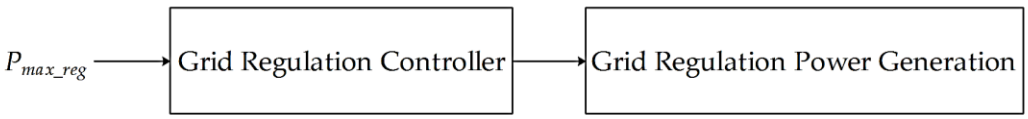


**Figure 2.3.** Grid regulation controller scheme

To achieve the maximum active power regulation, a control system that consistently checks the nominal active power, $P_{nom}$, is proposed, as shown in figure 2.4. In this controller, the nominal active power, the number of cars in regulation, $N$, and an online key to enable the V2G mode are matter. Lastly, the output power has been limited within the standard range to be considered as the maximum regulated active power. There is a threshold (0.5) for passing the first input to the second input, $C_1$, of this controller.

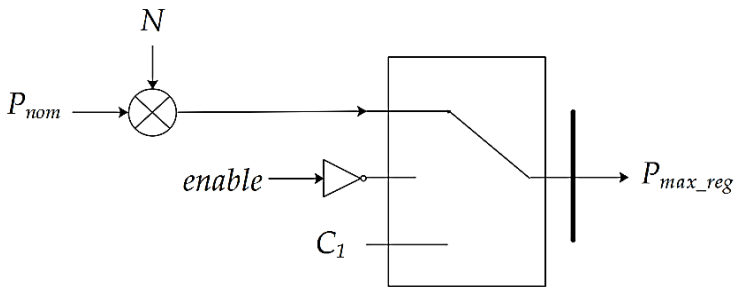


**Figure 2.4.** Outer control system scheme for gaining maximum regulated active power

In order to contribute to the grid regulation, real-time measurement of the frequency, $\omega_{\text{grid}}$, is required. By comparing $\omega_{\text{grid}}$ and the reference frequency, $\omega_{\text{ref}}$, the frequency deviation can be obtained. The frequency deviation should be less than 0.05%. Otherwise, the controller stops the process. To prevent sudden changes in the frequency deviation, the controller's derivative has been utilized. By considering that the frequency deviation is within the standard range, two gains for the grid regulation controller have been set by the operator, the open-loop gain, $K_1$, and the loop gain, $K_2$. Changing these two gains has a direct impact on the SoC of all the cars in the charge mode. A zero-crossing detection integrator has been considered to minimize the disturbance and steady-state error of the input signal. The output signal of the integrator has been rechecked to avoid the maximum allowable regulated active power that is fed into the grid regulation power generation system. Figure 2.5 illustrates a detailed diagram of the grid regulation controller.

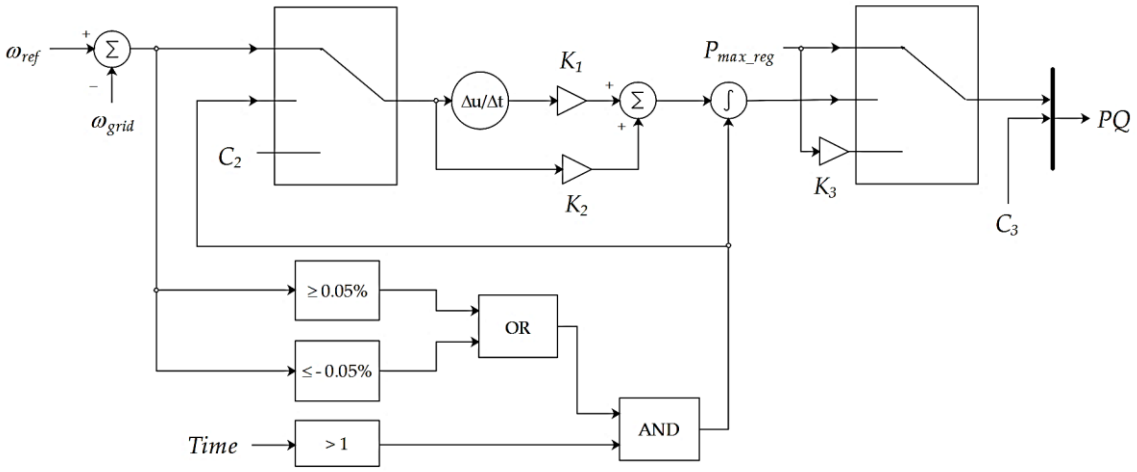


**Figure 2.5.** Control diagram of the grid regulation controller

Furthermore, by controlling the voltage, and consequently, the current through another control system, the proposed control strategy can ensure a contribution to the grid regulation power generation, as shown in figure 2.6.

The grid regulation power generation controller captures the voltage of pair phases. Therefore:

$$V = \frac{1}{3}(V_{ab} - a^2 V_{bc}) \tag{2-7}$$

where $V_{ab}$ is the voltage between phases a and b, and $V_{bc}$ is the voltage between phases b and c.

Moreover:

$$a^2 = e^{-j\frac{2\pi}{3}} \tag{2-8}$$

By using Equation (2-7) and decomposing the real and imaginary parts from the apparent power, $S$, the current can be derived as follows:

$$I = \frac{2}{3}\frac{S^*}{V^*} \tag{2-9}$$

where $V$ and $I$ denote the voltage and current, respectively. $S^*$and $V^*$ represent the complex conjugate of the apparent power and the complex conjugate of the voltage, respectively. Accordingly, the controller feeds constant current into the power grid and regulates the voltage and frequency, simultaneously.

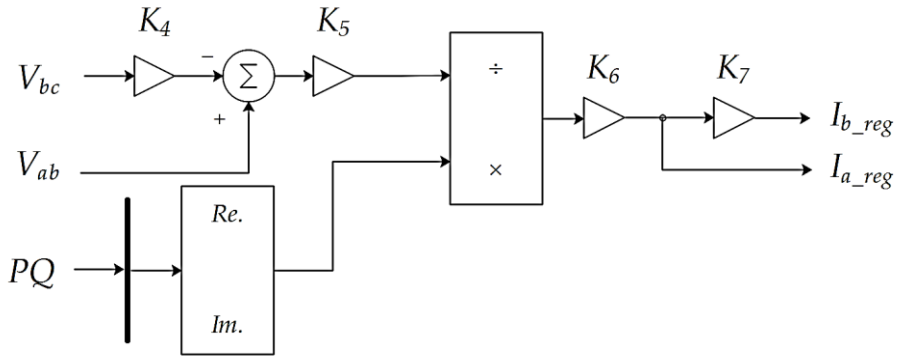


**Figure 2.6.** Control diagram of the grid regulation power generation

### *2.2.2.2. Charge Mode*

In order to control the PHEV station in charge mode, two states have been studied: (1) SoC, and (2) plug. The charge power generation controller requires the nominal active power and the number of cars in charge, $M$, as its inputs. Same as the grid regulation mode, a threshold (0.5) is used for passing the first input to the second input, $C_4$, of the charge power generation control system. The threshold can guarantee safe operation. Figure 2.7 shows the outer control diagram of the charge power generation controller.

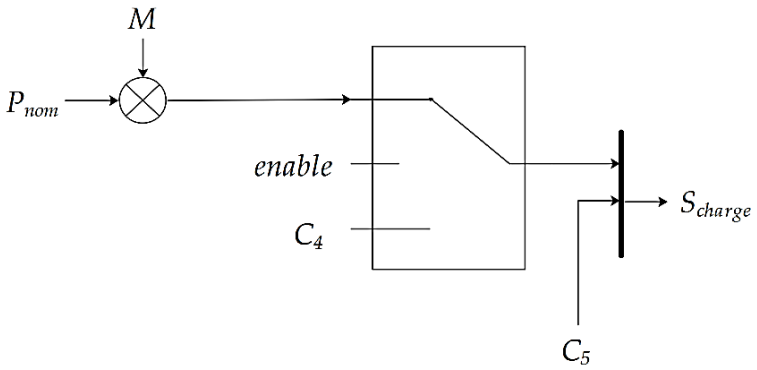


**Figure 2.7.** The outer control diagram of the charge power generation controller

Same as the previous section, by regulating the voltage, and decomposing the real and imaginary parts of the apparent power of the charging system, a constant current, $I_{reg}$, is obtained from the controller, and fed into the power grid. Figure 2.8 illustrates the inner control diagram of the charge power generation controller.

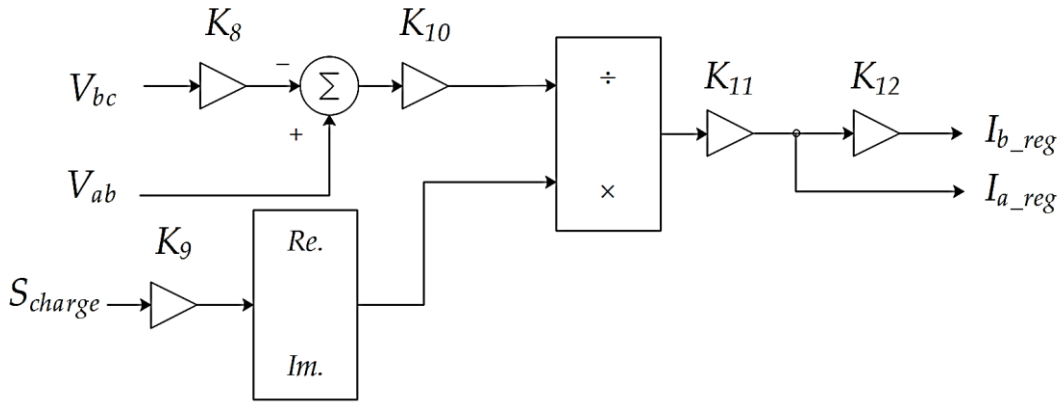


**Figure 2.8.** The inner control diagram of the charge power generation controller

Each group of cars has a certain charging profile. As mentioned, the car profile has been investigated by checking the SoC and plug states. Figure 2.9 demonstrates the control diagram of the profile of each PHEV in charge and regulation modes. In this control design, the SoC initialization and plug state have been implemented by using the Binary Search Method (BSM). Therefore, the SoC initialization and plug state have stochastic, but linear behavior. Complementary descriptions for the different profiles are provided in Section 2.2.7.

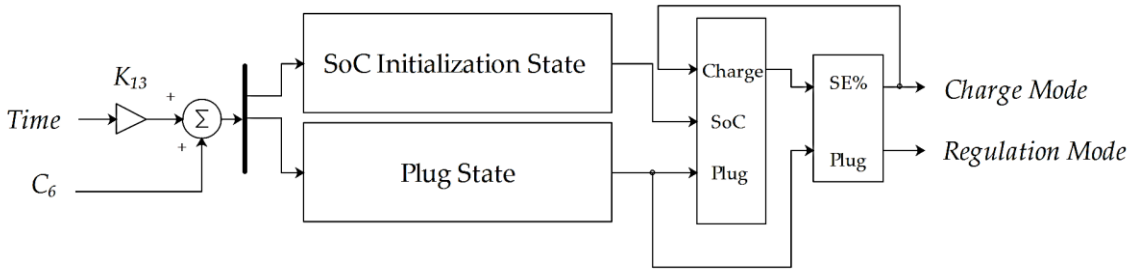


**Figure 2.9.** The control diagram of the profile of each PHEV in charge and regulation modes

In order to control the output changes of the SoC initialization and plug state within limits, two state limiters have been considered. By capturing the SoC initialization and plug state, and the present values of the SoC in different profiles, the state estimator for each SoC controller has been designed. Figure 2.10 indicates the SoC controller, where the output of this controller is the State Estimator ($SE\%$), and regulated for the charger controller. The SoC controller needs accurate information of the active power of the cars in charge, $P_{charge}$, the number of cars in charge mode, $M$, the number of cars in the specific charging profile, $L_i$ (where $i = 1, \dots, 5$), the number of cars in regulation mode, $N$, the active power of the cars in EV mode, $P_{EV}$, and the regulated output of the SoC initialization and plug state.

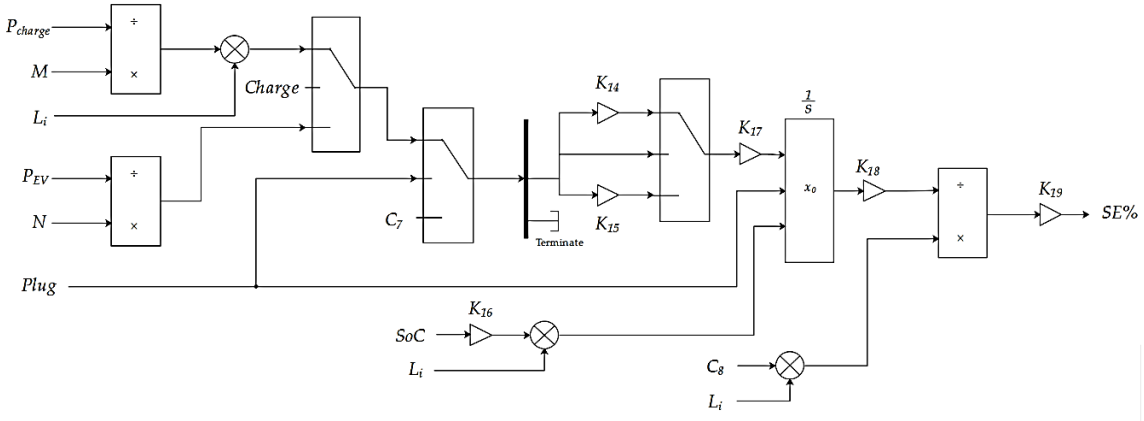


**Figure 2.10.** The control diagram of the SoC controller

The state estimation of batteries in PHEVs requires checking the mode of vehicles. The PHEV can be either in charge or EV mode. Therefore, there should be a switch to toggle between these two modes. By reaching the maximum level of the charge, the controller terminates the charging process. In the meantime, the controller checks the plug state dynamically, and if the PHEV is unplugged from the grid, it sends zero signal, $C_7$, as shown in figure 2.10, and terminates the charging process.

Assuming the PHEV is in charge mode, the charge/discharge efficiency has been taken into consideration. These two are modeled as two direct gains, $K_{14}$ and $K_{15}$, so that:

$$\begin{cases} K_{14} = \eta \\ K_{15} = 1/\eta \end{cases} \tag{2-10}$$

where $\eta$ shows the efficiency.

The SoC, which is converted to real-time by multiplying the present capacity by 1000×3600, the plug state, and the charging state are sent to an integrator with the initial condition and dynamic saturation, and lastly, the output is multiplied by the number of cars in a particular profile to obtain the state estimation. State estimation from this stage is used as the SoC of the vehicles. Deriving the state estimation, the cars are checked whether they are either in the charge mode or regulation mode through the charger controller. Figure 2.11 indicates the charger control diagram. In order to guarantee a high-efficiency output during the charging process, the state estimation has been set within the range of 85% and 95%. Otherwise, the charger terminates the process. In fact, this can ensure both injecting power with high quality to the power grid during the regulation mode and charging the batteries during the charging mode.

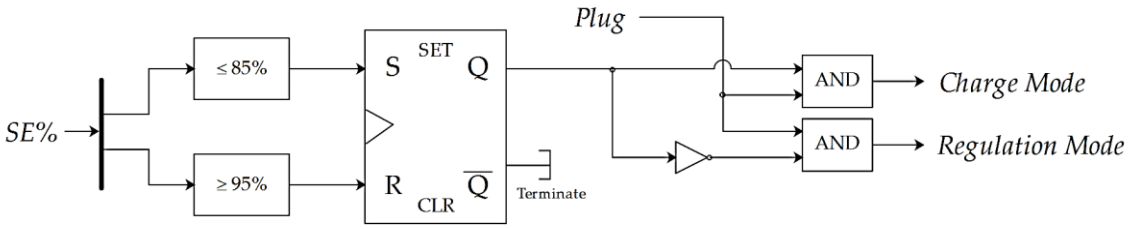


**Figure 2.11.** Control diagram of the charger

Proper operation of the charging station of PHEVs lead to the energy balance of ESSs in PHEVs subject to the maximum and minimum operating limitations in charging and discharging power as follows:

$$E_{s,i,(t+1)} = E_{s,i,t} + \eta_{s,i,c} \times P_{s,i,t,c} - \frac{P_{s,i,t,disc}}{\eta_{s,i,disc}} \tag{2-11}$$

subject to:

$$0 \leq P_{s,i,t,c} \leq k_{s,i,t,c} \times P_{s,i,c\_max} \tag{2-12}$$

$$0 \leq P_{s,i,t,disc} \leq k_{s,i,t,disc} \times P_{s,i,disc\_max} \tag{2-13}$$

$$k_{s,i,t,c} + k_{s,i,t,disc} \leq 1 \tag{2-14}$$

$$k_{s,i,t,c} + k_{s,i,t,disc} \in \{0,1\} \tag{2-15}$$

$$E_{s,i,min} \leq E_{s,t} \leq E_{s,i,max} \tag{2-16}$$

where indices $s$, $i$, and $t$ refer to the $s^{th}$ energy storage system at the $i^{th}$ bus in the $t^{th}$ time interval. Therefore, $E_{s,i,t}$ is the energy storage of the $s^{th}$ energy storage system at the $i^{th}$ bus in the $t^{th}$ time interval in MWh. $\eta_{s,i,c}$ and $\eta_{s,i,disc}$ are charging and discharging efficiencies, respectively. $P_{s,i,t,c}$ and $P_{s,i,t,disc}$ are charge and discharge power, and $k_{s,i,t,c}$ and $k_{s,i,t,disc}$ are the binary variables for charging and discharging operations of the $s^{th}$ energy storage system at the $i^{th}$ bus in the $t^{th}$ time interval, respectively.

Figure 2.12 shows the flow chart of the proposed bidirectional power charging strategy. According to the collected data from the installed meters, the amount of the active and reactive power in the system is checked. When V2G is not activated, the existing microgrid(s) satisfy the total load consumption, whether there is a contingency in the system or not. When V2G is activated, the SoC initialization and plug state of PHEVs are checked and based on them, the SoC can be estimated. According to the estimated SoC, PHEVs mode can be either in charge or regulations mode. By considering that there is no contingency in the system, the required power to charge PHEVs is supplied by the existing microgrid(s). Otherwise, all PHEVs in charge and regulation modes are passed through a regulation unit, and the regulated voltage and frequency are then used to update the active and reactive power.

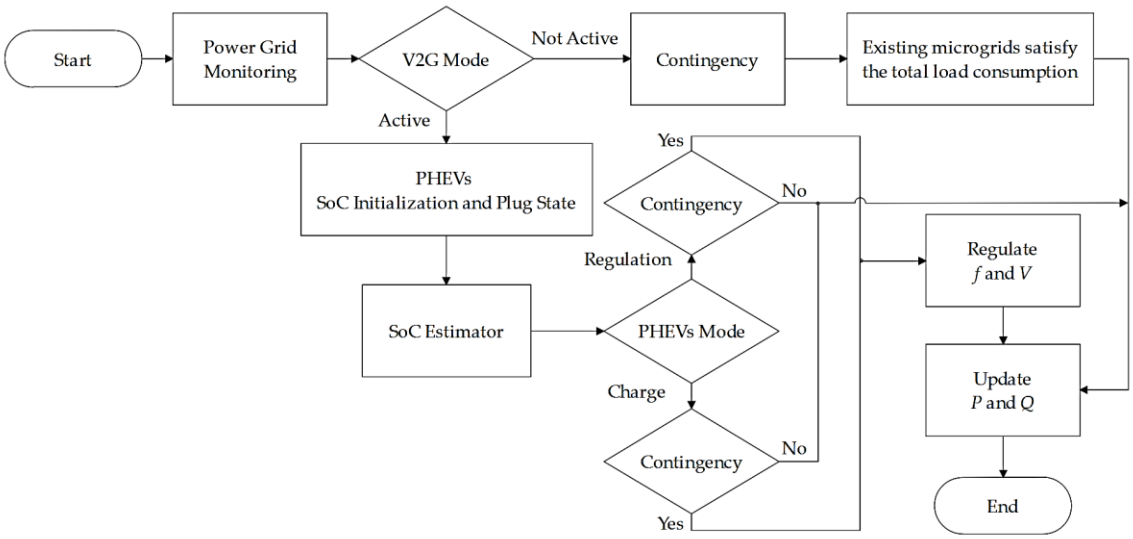


**Figure 2.12.** Flow chart of the proposed bidirectional power charging strategy

### *2.2.3. Diesel Generator*

A three-phase synchronous machine in the dq-rotor reference frame with the engine governor and excitation system has been modeled and considered as the diesel generator to feed 15 MW active power to the power grid. The nominal power, line-to-line voltage, and frequency of the generator are 15 MW, 25 kV, and 60 Hz, respectively. The IEEE type 1 synchronous generator voltage regulator combined with an exciter has been implemented as the excitation system. Moreover, the diesel governor has been modeled, where the desired and actual rotor speeds are the inputs and the mechanical power of the diesel engine is the output. Further, the motor inertia has been combined with the generator. The design considerations for the governor are made through the regulation of the controller and actuator as follows:

$$H_c = \frac{K(1 + T_3 s)}{(1 + T_1 s + T_1 T_2 s)} \tag{2-17}$$

where $H_c$ is the controller transfer function, $K$ is the regulator gain, and $T_1$, $T_2$, and $T_3$ are the regulator time constants, respectively.

Furthermore:

$$H_a = \frac{(1 + T_4 s)}{s((1 + T_5 s)(1 + T_6 s))} \tag{2-18}$$

where $H_a$ is the actuator transfer function, and $T_4$, $T_5$, and $T_6$ are the regulator time constants, respectively. The engine time delay, $T_d$, has been set to 0.024 sec. It should be noted that $\omega_{ref}$ and $V_{ref}$ of the diesel engine governor and excitation system have been set to 1 p.u.

Accordingly:

$$T_m - T_e - D\Delta\omega = J\frac{d\omega}{dt} \tag{2-19}$$

where $T_m = \frac{P_m}{\omega_m}$, $T_e = \frac{P_e}{\omega_e}$, and $\Delta\omega = \omega - \omega_{rated}$. $T_m$, $T_e$, $\omega_m$, and $\omega_e$ are the mechanical torque of the synchronous generator rotor shaft input from the prime mover, stator electromagnetic torque, mechanical speed of the rotor, and synchronous speed, respectively. $D$ indicates the damping coefficient, $\omega$ and $\omega_{rated}$ are the actual electrical and rated angular velocities, respectively. $P_m$ and $P_e$ are the mechanical and electromagnetic power, respectively. $J$ shows the rotational inertia, and $\theta$ indicates the electrical angle.

In addition:

$$E_0 = V_s - I(r_a - jx_s) \tag{2-20}$$

where $E_0$, $V_s$, and $I$ are the three-phase stator winding electromotive force, the stator voltage and current, respectively. Moreover, $r_a$ and $x_s$ indicate the armature resistance and stator reactance, respectively.

### *2.2.4. Wind Farm*

As the second source of energy, a wind farm with 4.5 MW nominal power capacity, with 13.5 m/s as the nominal wind speed, and 15 m/s as the maximum wind speed, is studied in this chapter. The wind speed fluctuations provide a situation to study the power

grid under a stochastic condition (uncertainty). The generated power by the wind farm can be obtained as follows:

$$P_{wind} = \begin{cases} 0 & 0 \le v_i < v_{cut-in} \\ \dfrac{v_i - v_{cut-in}}{v_r - v_{cut-in}} \times P_r & v_{cut-in} \le v_i < v_r \\ P_r & v_r \le v_i < v_{cut-out} \\ 0 & v_i \ge v_{cut-out} \end{cases} \quad (2\text{-}21)$$

where $P_{wind}$ is the active power generated by the wind farm, $P_r$ shows the rated power of the wind farm, $v_i$ indicates the wind speed, and $v_{cut-in}$, $v_r$, and $v_{cut-out}$ are the cut-in, rated, and cut-out speeds of the wind turbine, respectively. The output power of the wind farm has been treated as a negative load so that the power factor can be kept at a constant level.

### *2.2.5. Loads*

A three-phase squirrel-cage asynchronous machine 1.5 MVA, 600 V, 60 Hz in the dq-reference frame (as the industrial load), and a set of loads with the nominal power of 10 MW at 0.95 power factor (as the residential load) have been modeled as the loads' case study. This model can represent the impact of inductive loads on the microgrid. The residential load follows a specific profile with the assigned power factor during the day. Further, the industrial load has been controlled by the square relation between the mechanical torque and the rotor speed.

### *2.2.6. Power Transformers*

Two three-phase power transformers, a 20 MVA, 25kV/25kV, 60Hz transformer for the voltage regulation with Yg-Yg winding connections and a 20 MVA, 25kV/600V, 60 Hz step-down transformer with Yg-Yg winding connections have been modeled as a part of transmission systems for the power system.

### *2.2.7. Power System Modeling*

As shown in figure 2.2, a single-line diagram of a power system consisting of different microgrids and PHEVs has been modeled, where the total peak load is 10.15 MW,

and the total generated power is 19.5 MW. One of the contributions of this thesis is to consider variable power loading levels for PHEVs, which lead to different profiles for the charging stations. Five different profiles have been assigned to PHEVs. Profile 1 is for vehicles with the possibility to be charged during the working hours. Profile 2 is for vehicles with the possibility to be charged during working hours but with a longer ride. Profile 3 is for vehicles with no possibility to be charged during the working hours. Profile 4 is for vehicles which are parked at home and charged during the whole day. Profile 5 is for vehicles that are charged during the night shift. In this case, the impact of charging on the power grid has been investigated. In order to differentiate between the SoC of the PHEVs and the stand-alone battery packs, different charging and discharging cycles have been studied in this chapter. The generator balances the power and load demand. The generator determines the frequency deviations of the grid at the rotor speed. By using transformers, the voltage level has been stepped-down to suitable voltage levels for the power grid. Table 2.2 shows the corresponding values of the control parameters for the charging station system in the power grid.

**Table 2.2.** Control parameters of the charging station

| Parameter | Value |
|---|---|
| $C_1$, …, $C_5$ and $C_7$ | 0 |
| $C_6$ | 1 |
| $C_8$ | $85\times10^3$ |
| $K_1$ | 2 |
| $K_2$ | $4\times10^3$ |
| $K_3$, $K_9$, and $K_{17}$ | -1 |
| $K_4$, $K_7$, $K_8$, and $K_{12}$ | $e^{(-j2\pi/3)}$ |
| $K_5$ and $K_{10}$ | 1/3 |
| $K_6$ and $K_{11}$ | 2/3 |
| $K_{13}$ and $K_{18}$ | 1/3600 |
| $K_{14}$ | 1/(90%) |
| $K_{15}$ | 90% |
| $K_{16}$ | $306\times10^6$ |
| $K_{19}$ | 100 |

It is well-known that the PHEV charging process highly depends upon the connection point to the power system. This means that by connecting the PHEV to a weak bus, more power drains from the grid and the voltage drop increases, and consequently, it has a negative impact on the power grid.

Two scenarios have been investigated in 24 hours. The wind speed varies during the day and has multiple maximum and minimum values. The residential load consumption profile is similar to that of the real world. The demand is low during the day, increases to the peak value during the evening and night, and gradually decreases during the late night. Two events have significantly affected the grid frequency during the day: (1) event 1, which is the asynchronous machine (industrial load) start-up at t = 03:00 a.m., and (2) event 2, which is the wind farm outage at t = 10:00 p.m., when the wind speed exceeds the maximum speed. The case study has been simulated under two different conditions for vehicles in regulation and charging modes.

### *2.3. Results and Discussions*

The case study in this chapter conducts the power profile (the generated and consumed power) as the bidirectional power flow during a 24-hour. Contributions of the diesel generator and wind farm and the impact of PHEVs on the peak load reduction have been studied in this section. To study the bidirectional power flow, the active and reactive power balance of the system have been determined as follows:

$$P_{g_{i,t}} + P_{w_{i,t}} + P_{L_{i,t}} - P_{s,i,c} + P_{s,i,disc} - \sum_{j}[\frac{V_{i,t}V_{i,t}}{Z_{ij}}\cos\theta_{ij} + \frac{V_{i,t}V_{j,t}}{Z_{ij}}\cos(\theta_i - \theta_j + \theta_{ij})] = 0 \quad (2\text{-}22)$$

$$Q_{g_{i,t}} - Q_{L_{i,t}} - \sum_{j}[\frac{V_{i,t}V_{i,t}}{Z_{ij}}\sin\theta_{ij} + \frac{V_{i,t}V_{j,t}}{Z_{ij}}\sin(\theta_i - \theta_j + \theta_{ij})] = 0 \quad (2\text{-}23)$$

subject to:

$$\frac{V_{i,t}V_{j,t}}{Z_{ij}}\cos(\theta_{i,t} - \theta_{j,t} + \theta_{ij,t}) - \frac{V_{i,t}V_{j,t}}{Z_{ij}}\cos\theta_{ij,t} \le P_{ij,max} \quad (2\text{-}24)$$

$$\frac{V_{i,t}V_{j,t}}{Z_{ij}}\sin(\theta_{i,t} - \theta_{j,t} + \theta_{ij,t}) - \frac{V_{i,t}V_{j,t}}{Z_{ij}}\sin\theta_{ij,t} \le Q_{ij,max} \quad (2\text{-}25)$$

where indices i, j, s, and t refer to the bus i, bus j, the sth energy storage system, and the tth time interval. $P_{g_{i,t}}$, $P_{w_{i,t}}$, $P_{L_{i,t}}$, $Q_{g_{i,t}}$ and $Q_{L_{i,t}}$ show the active power generated

by the non-renewable energy source, the active power generated by the wind farm, the active power consumed by the load, the reactive power generated by the non-renewable energy source, and the reactive power consumed by the load at the ith bus in the tth time interval, respectively. Further, $V$, $\theta$, and $Z$ indicate the voltage magnitude, and angle, and the impedance of the bus, respectively. $P_{ij,max}$ and $Q_{ij,max}$ are the maximum allowable active and reactive power that can be transferred between the buses, respectively.

### *2.3.1. V2G Mode is Deactivated*

Based on the results of the simulation for 86,400 sec. (24 hours), which is shown in figure 2.13, when the V2G system is not under operation, due to the defined scenarios during two different time intervals, one at $t = 03:00\ a.m.$ (10,800 sec.) and the second one at $t = 10:00\ p.m.$ (79,200 sec.), the industrial load bus voltage shows a significant change. Due to the first event, the voltage at all buses changes. Based on the nature of the load profile, the industrial load is not under operation before the third hour (the output power is 0 MVA), and the residential load reaches its minimum value (5.446 MVA), because of less usage of the normal resistive and inductive loads, such as lightings, refrigerators, etc. Therefore, the amount of current, and consequently, the drained power from the grid is not significant. At t = 10,800 sec., the industrial load starts up, and the power flow in the grid changes. The voltage at the industrial load bus drops, and the current increases drastically (from 0 to 2,184 A). Hence, 445.3 kW power is extracted as the power losses due to this event, and accordingly, this power is supplied by the diesel generator and wind farm. The total load demand at that time reaches 7.235 MVA, and the power grid supplies the load through the amount of generated power by the two microgrids, where the generation contributions of the diesel generator and wind farm are 5.328 MVA and 2.446 MVA, respectively. Thus, the total generated power is derived as 7.774 MVA, which is more than the total load demand. It should be noted that when the V2G mode is deactivated, by increasing or decreasing the corresponding values of the controller's gains ($K_1$ and $K_2$), the SoC of the batteries of PHEVs in the charge mode does not change.

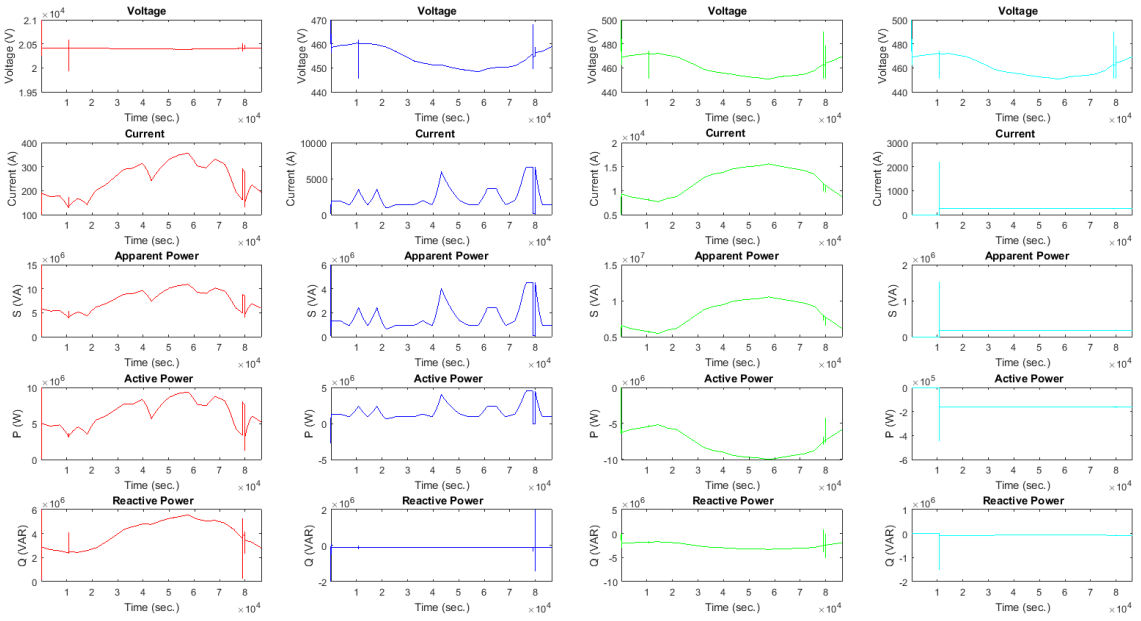


**(a)** **(b)** **(c)** **(d)**

**Figure 2.13.** Voltage, current, the apparent power, active power and reactive power curves of **(a)** the diesel generator, **(b)** wind farm, **(c)** residential load, and **(d)** industrial load during 24 hours when the V2G system is not under operation

As shown in figure 2.14, the total load consumption increases from 6.0980 MVA at 05:00 a.m. (21,600 sec.) to 8.1800 MVA at 10:00 p.m. (79,200 sec.). Based on the results of the simulation, the diesel generator and wind farm successfully supply the load demand, even during the contingency. The transient time related to the voltage regulation at each bus is minimized by proper operating of the controllers. This is achieved by defining the power flow constraints (Equations 2-24 and 2-25) for the power grid. When the wind farm has less generation or is not under operation for a certain period of the time, the diesel generator acts as a fast-response power supply to supply the load without interruption. Table 2.3 shows the power flow of the power grid during the entire day.

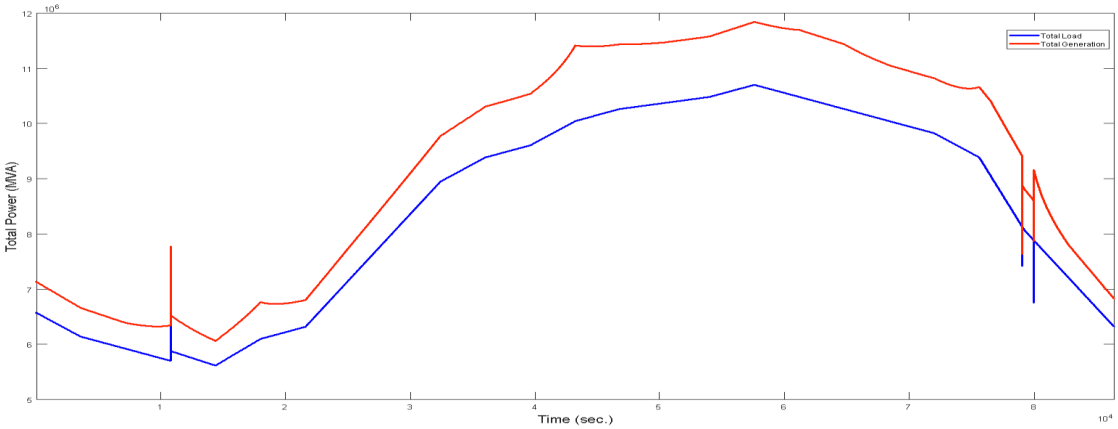


**Figure 2.14.** Total generated and consumed power curves in 24 hours when the V2G system is not under operation

**Table 2.3.** Power flow results when the V2G system is not under operation

| Time | Diesel<br>Wind | Total Generation | Total Demand | Power Losses |
|---|---|---|---|---|
| 00:00 a.m. | 3.3660<br>0.7000 | 4.0660 | 3.8480 | 0.2180 |
| 01:00 a.m. | 5.3350<br>1.3300 | 6.6650 | 6.1430 | 0.5220 |
| 02:00 a.m. | 5.4550<br>0.9340 | 6.3890 | 5.9210 | 0.4680 |
| 03:00 a.m. | 5.3280<br>2.4460 | 7.7740 | 7.2350 | 0.5390 |
| 04:00 a.m. | 5.1270<br>0.9340 | 6.0610 | 5.6160 | 0.4450 |
| 05.00 a.m. | 4.3380<br>2.4260 | 6.7640 | 6.0980 | 0.6660 |
| 06:00 a.m. | 6.1750<br>0.6270 | 6.8025 | 6.3170 | 0.4855 |
| 07:00 a.m. | 6.8530<br>0.9330 | 7.7860 | 7.1920 | 0.5940 |
| 08:00 a.m. | 7.8370<br>0.9340 | 8.7710 | 8.0710 | 0.7000 |
| 09:00 a.m. | 8.8380<br>0.9340 | 9.7720 | 8.9470 | 0.8250 |
| 10:00 a.m. | 8.9790<br>1.3290 | 10.308 | 9.3830 | 0.9250 |
| 11:00 a.m. | 9.6030<br>0.9350 | 10.538 | 9.6060 | 0.9320 |
| 12.00 p.m. | 7.4050<br>4.0110 | 11.416 | 10.004 | 1.4120 |
| 01:00 p.m. | 9.0070<br>2.4300 | 11.437 | 10.260 | 1.1770 |
| 02:00 p.m. | 10.140<br>1.3300 | 11.470 | 10.370 | 1.1000 |
| 03:00 p.m. | 10.640<br>0.9340 | 11.574 | 10.480 | 1.0940 |
| 04:00 p.m. | 10.910<br>0.9340 | 11.844 | 10.700 | 1.1440 |
| 05.00 p.m. | 9.2090<br>2.4290 | 11.638 | 10.430 | 1.2080 |
| 06:00 p.m. | 9.0070<br>2.4290 | 11.436 | 10.260 | 1.1760 |
| 07:00 p.m. | 10.120<br>0.9340 | 11.054 | 10.040 | 1.0140 |
| 08:00 p.m. | 9.4940<br>1.3290 | 10.823 | 9.8260 | 0.9970 |
| 09:00 p.m. | 6.6540<br>4.0100 | 10.664 | 9.3870 | 1.2770 |
| 10:00 p.m. | 8.3160<br>0.0120 | 8.3250 | 8.1800 | 0.1480 |
| 11:00 p.m. | 6.8520<br>0.9340 | 7.7860 | 7.1950 | 0.5910 |

Note: All the values are in MVA and have been rounded to the closest number.

Figure 2.15 shows the dynamic behavior of the converter station during the simulation time. As long as the breaker of the converter station is open and the V2G system is not under operation, the power consumption by the converter station is completely insignificant. However, the station detects the two events during the simulation time. It should be noted that the consumed power by the converter station is considered as the power losses in table 2.3. As shown in figure 2.15, in the regulation and charge modes, the consumed power by the converter station is close to zero.

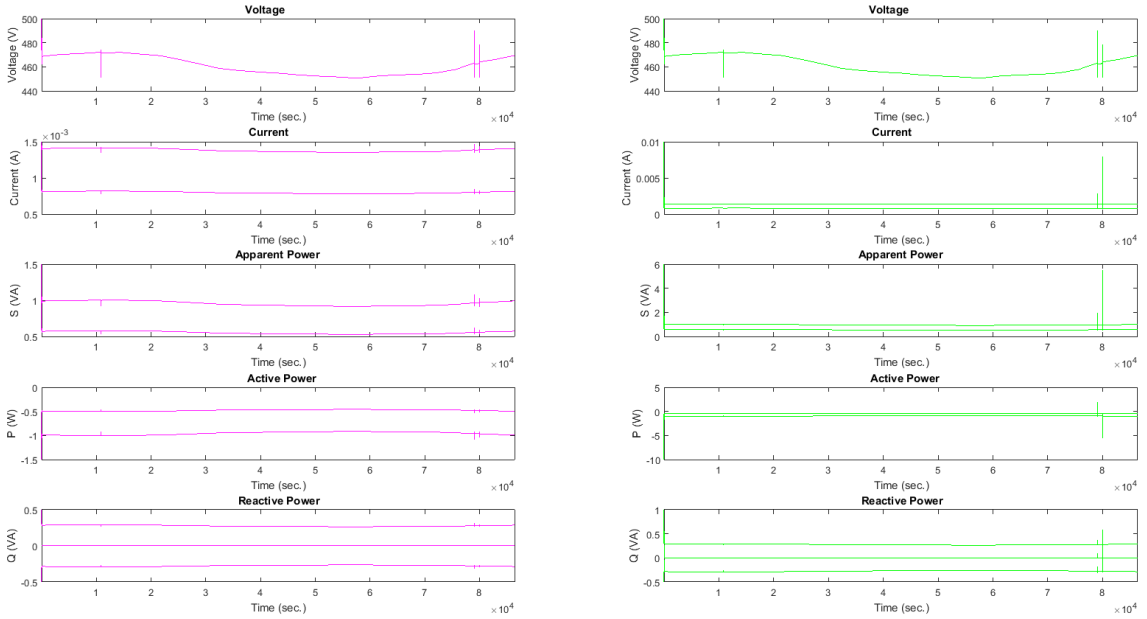


**(a)** **(b)**

**Figure 2.15.** Voltage, current, the apparent power, active power, and reactive power curves of the converter station in **(a)** the charge mode and **(b)** the regulation mode in 24 hours when the V2G system is not under operation

### *2.3.2. V2G Mode is Activated*

When the V2G mode is activated, the operating impact of the V2G system changes the power flow of the grid. Theoretically, it is expected that when the V2G system is under operation, more power is supposed to be drained from the power grid. The more power consumed by the converter station, the greater the power required from the diesel generator and wind farm. Unlike the previous mode that the V2G mode was deactivated, the different car profiles change the total load profile. Therefore, the peak load is expected to be more

than the previous operating mode. Figure 2.16 shows the results of the simulation in the V2G system operation.

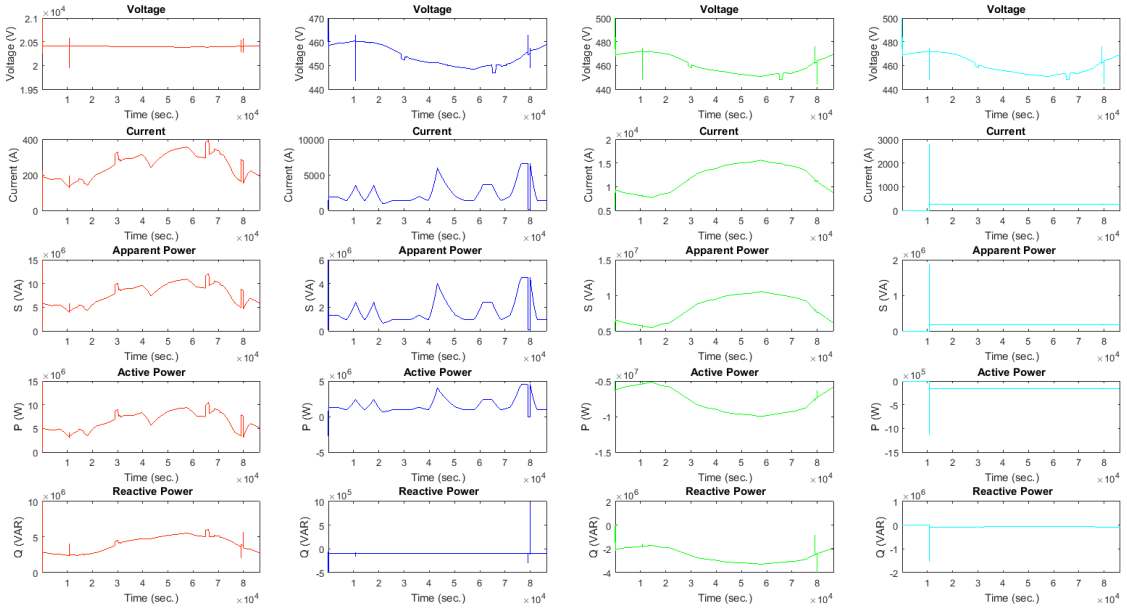


**(a)** **(b)** **(c)** **(d)**

**Figure 2.16.** Voltage, current, the apparent power, active power and reactive power curves of **(a)** the diesel generator, **(b)** wind farm, **(c)** residential load, and **(d)** industrial load during 24 hours when the V2G system is under operation

Unexpected events (contingency and/or outage) in the power system lead to a change in the voltage and frequency. Heavy load or generator outages can be considered as such changes that influence the voltage and frequency variations. As shown in figure 17, based on the two defined scenarios, at $t = 10{,}800\ sec.$, the industrial load starts up and drains power from the generation buses. The total generated power should satisfy the total load demand, including the cars in profiles 4 and 5. Due to the sudden changes in the power, the converter station detects the voltage and frequency variations, and the controllers switch to the regulation mode and contribute to the grid regulation, as shown in figure 2.17. However, the voltage curve in both charge and regulation modes fluctuates around its nominal value, the frequency deviations related to the power changes after the contingency are more visible. Due to rapid fluctuations in the voltage of the power supply or loads, a momentary flicker can also be observed in the power system. The designed

system attempts to mitigate and eliminate this momentary flicker by regulating (or stabilizing) the voltage.

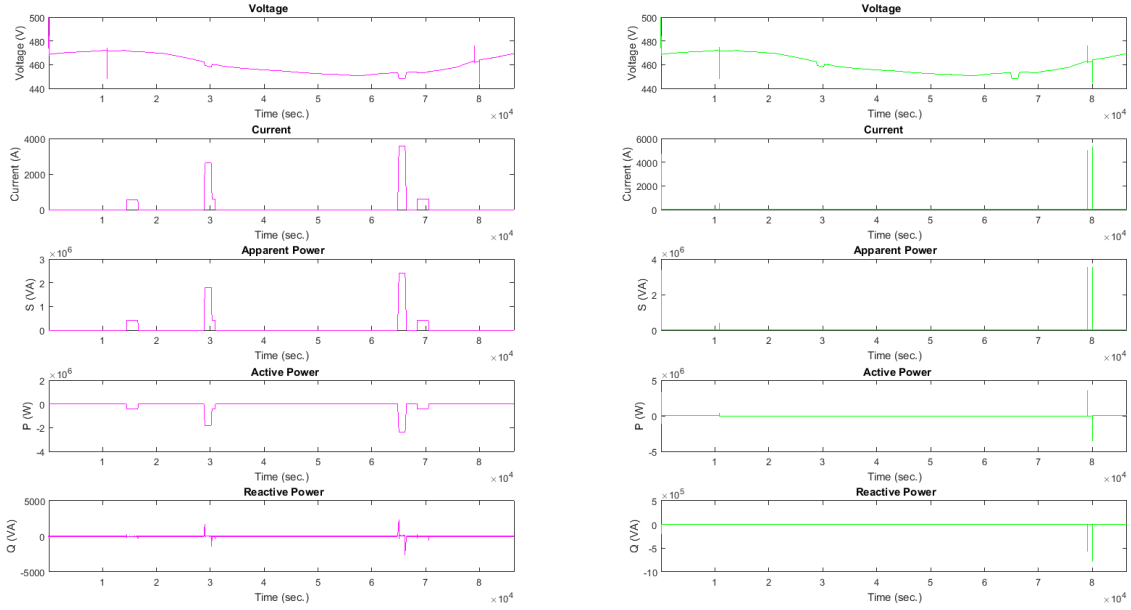


**(a)** **(b)**

**Figure 2.17.** Voltage, current, the apparent power, active power, and reactive power curves of the converter station in **(a)** the charge mode and **(b)** the regulation mode in 24 hours when the V2G system is under operation

According to the descriptions of the car profiles in Section 2.2.7, the behavior of the SoC varies based on the car profile. Figure 2.18 illustrates the SoC of the different car profiles during the day, when the V2G system is under operation. When the second scenario occurs at $t = 79{,}200\, sec.$, the level of the generated power is reduced significantly. Consequently, PHEVs switch to the regulation mode to contribute to the voltage and frequency regulation and restore the system to its previous condition. Because the cars in profile 4 are connected to the grid for the entire day, their contributions to the grid regulation are more severe. Also, due to the grid mode controller settings, a gradual increase in the SoC is expected. Due to the fact that the wind farm outage decreases the level of generated power, the system can reach a critical condition without utilizing proper control systems.

It is observed that when the V2G mode is activated, by decreasing $K_1$, the SoC of the batteries decreases very slightly during the simulation time. By increasing $K_1$, the SoC

of the cars in profile 4 increases from 90.0 to 90.6. Decreasing $K_2$ causes an inverse trend in the SoC variations. This means that the SoC of the cars in profile 4 increases, and then, gradually decreases. By increasing $K_2$, the SoC of the batteries of the cars in profile 4 moderately decreases during the simulation time. It should be noted that the minimum level of the SoC is 10%.

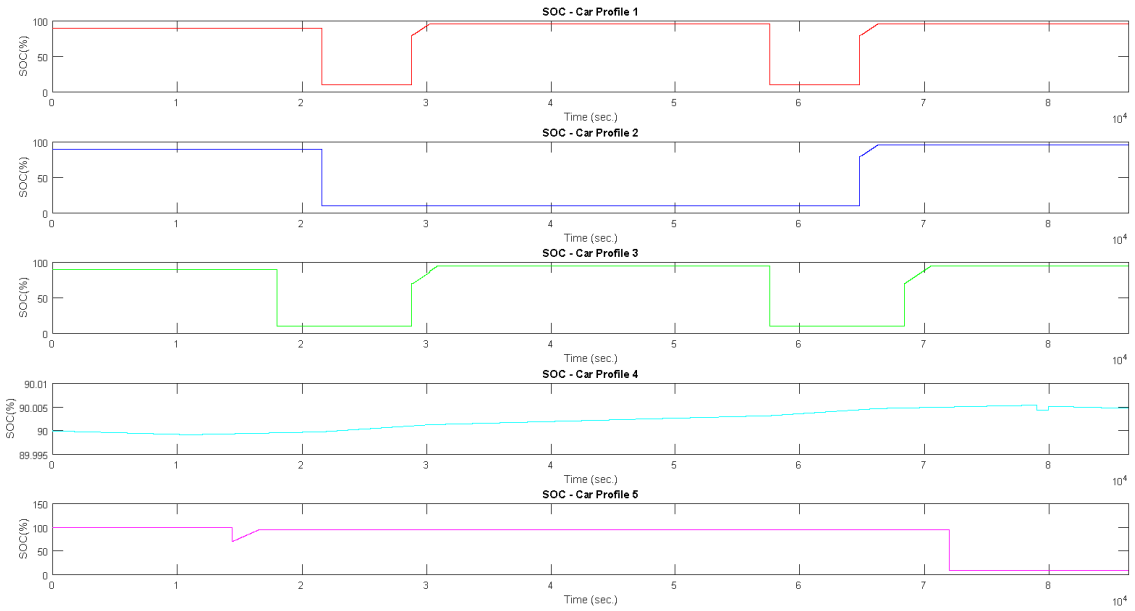


**Figure 2.18.** SoC of the different car profiles in 24 hours when the V2G system is under operation

Figure 2.19 illustrates the total generated and consumed power curves when the V2G system is under operation. As shown in this figure, the total load demand varies throughout the day and is met by the dispatchable generation unit. The generation units adjust operations to follow the load pattern. When the V2G system is not under operation, there is only one peak point during the entire simulation time. However, when the V2G mode is activated, the number of peak points is increased due to the different car profiles. The peak points are met when the number of car-users is increased, and the generation units are forced to generate more power. The maximum peak point has been detected between t = 17:00 and t = 18:00, because cars in profiles 1, 3, 4, and 5 are all in the charging mode. Although the wind farm has been under operation, the diesel generator has been operated close to its maximum capacity. The total power at $t = 10{,}800\ sec.$ has reached its first

peak point of 8.107 MVA as the generated power, and 7.435 MVA as the total load demand. The loads have met the minimum value of 5.616 MVA at $t = 14{,}400\ sec.$ where the generated power has been 6.062 MVA. Between $t = 14{,}400\ sec.$ and $t = 16{,}550\ sec.$, the total load demand has increased to 6.303 MVA (due to the different charging profiles), and the generation units have followed the load profile, and have generated 6.831 MVA. Over time, the total load level has shown an overall increasing trend and increased from 6.100 MVA at t = 18,800 sec. to 6.317 MVA at t = 21,600 sec. and 8.071 MVA at t = 28,800 sec., where the total generated power has reached 6.766 MVA, 6.802 MVA, 8.771 MVA, respectively. The power grid has experienced the second increase between t = 28,800 sec. and t = 30.160 sec. in which more cars have been in the charging mode. During this time interval, the total load demand has increased from 9.916 MVA to 10.200 MVA, and the generated power has been 10.680 MVA and 11.020 MVA, respectively. The same trend has been observed between t = 30,940 sec. and t = 64,800 sec. in which the number of PHEVs in charge has been increased. The demand has changed from 8.591 MVA to 10.270 MVA, and correspondingly, the generated power has varied from 9.365 MVA to 11.440 MVA, respectively. At the third peak point, the generated power has reached its maximum capacity where approximately the total load demand has been 12.650 MVA. From t = 66.200 sec. to t = 79,200 sec., both the total load demand and generated power have decreased, but in general, their corresponding values have remained at a high level. At t = 79,200 sec., the power grid has lost 4.5 MW active power due to the outage of the wind farm and accordingly, there has been an intensive drop in the generated power, and the load demand has been more than the generated power. This could interrupt the power flow, and there has been this need to use an auxiliary system, such as the V2G system to restore power. As shown in figure 2.19, PHEVs have supported the grid and contributed to the voltage and frequency regulation, and also the robustness of the proposed control system has been illustrated. The decreasing trend in both the generated power and total load demand has continued until the load level has decreased.

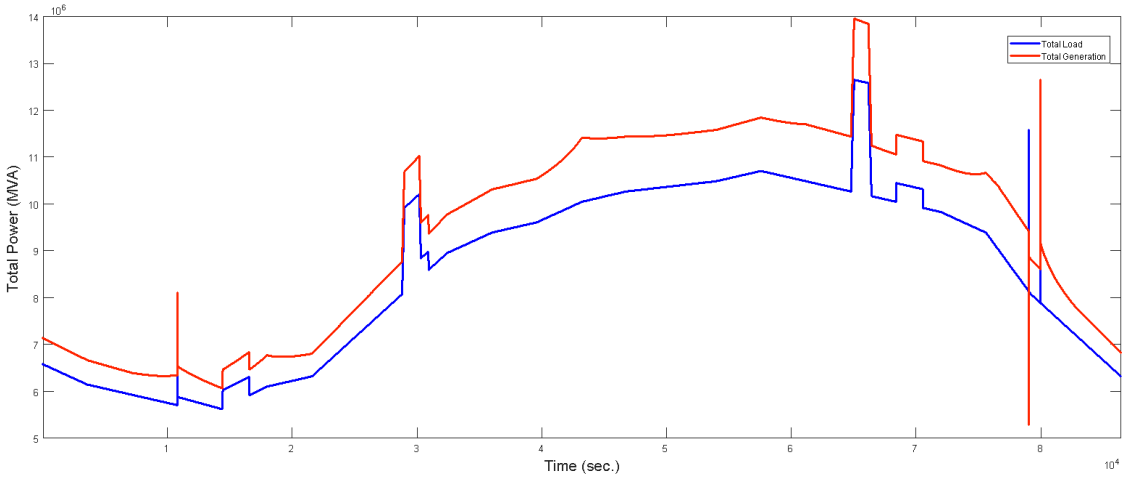


**Figure 2.19.** Total generated and consumed power curves in 24 hours when the V2G system is under operation

### *2.4. Summary*

This chapter reveals the impact of PHEVs charging on the power grid. A bidirectional charging station with a novel control strategy is proposed to solve the problem of voltage and frequency regulation in the power system due to the charging of PHEVs. A central AC/DC VSC converter station is investigated to inject active and reactive power into the power grid to regulate the voltage and frequency and reduce the peak load, as well as power quality improvement by considering the SoC and available active power in power grids. The proposed control strategy allows PHEVs to contribute to the grid regulation when an event occurs in a DG-based power grid consisting of different microgrids, diesel generator and wind farm, PHEVs with several charging profiles, and different loads. The simulation results show the robustness of the proposed control strategy.

# CHAPTER 3

## *An Improved Droop-Based Control Strategy for MT-HVDC Systems*

### *3.1. VSC-HVDC Station in MT-HVDC Systems*

#### *3.1.1. VSC-HVDC Station Control Strategy*

The MT-HVDC system consists of several Voltage-Sourced Converter (VSC)-HVDC stations, which are connected to each other via the DC grids. The DC voltage level at each bus should be fixed or in a small window of maximum and minimum limits. Each terminal should be capable of adopting various control strategies depending on the system requirements. Therefore, a proper VSC-HVDC system should be capable of monitoring and controlling both the AC-side and DC-side parameters. On the AC side and considering the type of the power grid connection, the VSC-HVDC station can operate in constant $V_{AC}$-mode or constant $Q$-mode. It is also possible to add $f$-droop controller in the AC-bus control. On the DC side, the VSC-HVDC station can operate in constant $V_{DC}$-mode, constant $P$-mode, or constant $I_{DC}$-mode. Considering the connected VSC-HVDC station to the AC generator(s) as the single power source in the AC grid, none of the DC parameters can be controlled.

##### *3.1.1.1. Constant AC Voltage Control*

The main objective of the constant $V_{AC}$ control strategy is to maintain the level of the AC voltage at the Point of Common Coupling (PCC) constant. This strategy is utilized, when the connected VSC-HVDC station to the AC generator(s) is the single power source in the entire power grids. Therefore, the power flow is dependent on the grid structure and consequently, the active and reactive power flows are not decoupled. It should be noted that in this control strategy, there is no need for frequency control.

##### *3.1.1.2. Constant Active Power-AC Voltage Control*

In the long transmission lines, when the resistance ($R$) and inductance ($L$) are too high, the voltage drop across the line increases. As $V_{AC}$ in the long transmission lines is not

constant, the VSC-HVDC station should be capable of regulating the level of the AC voltage. Therefore, the $P - V_{AC}$ control strategy is utilized, when both constant active power flow and AC voltage is required. The constant active power flow is achieved using the active power flow controller. $P_{ref}$ comes from a central power dispatching VSC-HVDC station or sets by operators manually.

#### *3.1.1.3. AC Voltage-DC Voltage Control*

The $V_{AC} - V_{DC}$ control strategy is applied, when the transmission lines have a significant voltage drop and the aim is to regulate the level AC voltage, as well as the DC voltage, by the VSC-HVDC station. To control $V_{AC}$ and $V_{DC}$, the reactive power flow controller and active power flow controller are required, respectively.

#### *3.1.1.4. Active Power-Reactive Power Control*

When the level of the AC voltage is constant by itself, the constant $P - Q$ control strategy is required. In this control strategy, $P_{ref}$ and $Q_{ref}$ are needed to be assigned for each VSC-HVDC station.

#### *3.1.1.5. Reactive Power-DC Voltage Control*

In the $Q - V_{DC}$ control strategy, the level of the AC voltage is constant by itself and there is the need for regulating the DC voltage. Also, the generated reactive power can be consumed at the other buses in the AC grid.

#### *3.1.1.5. Frequency Control*

When the $f$ control strategy is applied, the VSC-HVDC station contributes to the aggregated frequency regulation (based on the specific droop characteristics) of the AC grid.

### *3.1.2. VSC-HVDC Station Configuration*

Figure 3.1 illustrates the complete structure of a two-level VSC-HVDC station in the $dq$ reference frame. A two-level VSC-HVDC station consists of a six-pulse bridge with Insulated-Gate Bipolar Transistors (IGBTs) and parallel diodes. Using parallel diodes in

the opposite direction enables power flow in either direction. The transformer in the AC side transforms the level of the AC voltage into a level, which is suitable for the converter. A passive filter should be used to minimize the AC voltage ripples and isolate the harmonics in the current due to the IGBT switching away from the AC grid. It should be noted that the shunt capacitance and resistance, and the series inductance of the DC grids are neglected. The DC capacitor can minimize the DC voltage ripples. For the long transmission lines, only the series resistance should be considered for the DC links. The VSC-HVDC station consists of a three-phase switch-mode converter and uses the Pulse Width Modulation (PWM) technique to control its phase voltage [17].

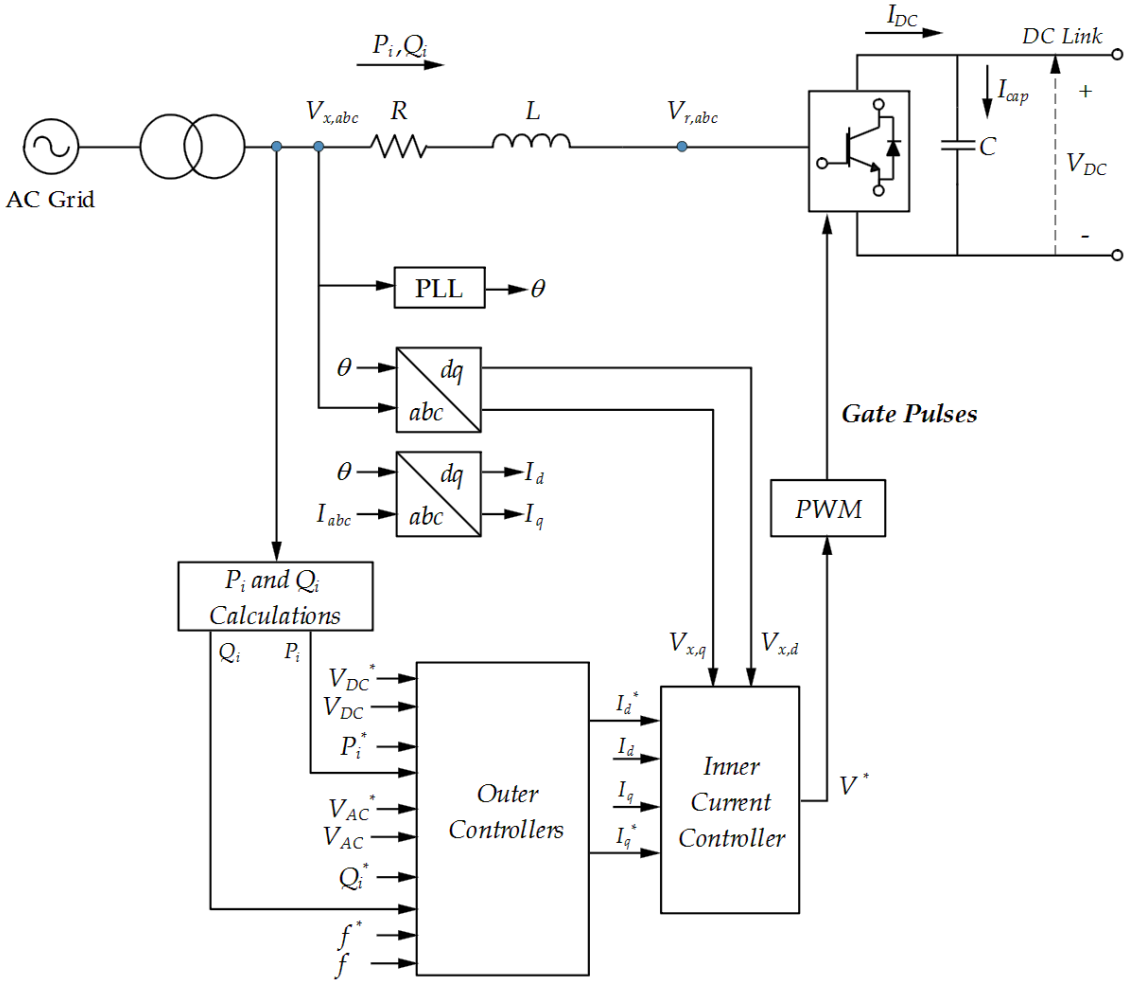


**Figure 3.1.** The complete structure of a two-level VSC-HVDC station

### *3.1.3. VSC-HVDC Station Operation*

The inner current controller, shown in figure 3.1, is equipped with a Phase Lock Loop (PLL) to instantaneously determine the phase angle and frequency. Furthermore, the inner current controller depends on the synchronously rotating reference frame for observing all the AC voltage and current quantities involved in the VSC-HVDC stations. As shown in figure 3.1, the inner controller should be fed by the outer controllers. Considering the control mode, the outer controllers provide the reference current to the VSC-HVDC station. Moreover, the inner current controller prevents overloading during faults and evaluate the voltage drop on the AC side.

In order to analyze the operation of the VSC-HVDC station and considering that the converter station is connected to an AC grid, the voltage on the AC side of the VSC-HVDC station can be calculated by applying the Kirchhoff's Voltage Law (KVL) as follows:

$$V_{x,abc} = RI_{abc} + L\frac{dI_{abc}}{dt} + V_{r,abc} \tag{3-1}$$

where $V_{x,abc}$ is the voltage on the AC side, $V_{r,abc}$ is the input voltage of the converter station, $I_{abc}$ is the injected current to the converter station, and $R$ and $L$ are the resistance and inductance between the converter station and the AC grid, respectively.

Neglecting the power losses, on the steady-state, the DC-side active power is equal to the AC-side active power. Therefore,

$$P_{abc} = P_{DC} \tag{3-2}$$

To achieve a decoupled control of active and reactive power, Equation (3-1) should be transferred to the $dq$ reference frame using the Park transformation, as follows:

$$\begin{bmatrix} V_{x,d} \\ V_{x,q} \\ V_{x,0} \end{bmatrix} = \frac{2}{3} \begin{bmatrix} \cos(\theta) & \cos(\theta - \frac{2\pi}{3}) & \cos(\theta + \frac{2\pi}{3}) \\ \sin(\theta) & \sin(\theta - \frac{2\pi}{3}) & \sin(\theta + \frac{2\pi}{3}) \\ \frac{1}{2} & \frac{1}{2} & \frac{1}{2} \end{bmatrix} \begin{bmatrix} V_{x,a} \\ V_{x,b} \\ V_{x,c} \end{bmatrix} \quad (3\text{-}3)$$

The input voltage of the converter station in the $dq$ reference frame is as follows:

$$\begin{bmatrix} V_{r,d} \\ V_{r,q} \\ V_{r,0} \end{bmatrix} = \frac{2}{3} \begin{bmatrix} \cos(\theta) & \cos(\theta - \frac{2\pi}{3}) & \cos(\theta + \frac{2\pi}{3}) \\ \sin(\theta) & \sin(\theta - \frac{2\pi}{3}) & \sin(\theta + \frac{2\pi}{3}) \\ \frac{1}{2} & \frac{1}{2} & \frac{1}{2} \end{bmatrix} \begin{bmatrix} V_{r,a} \\ V_{r,b} \\ V_{r,c} \end{bmatrix} \quad (3\text{-}4)$$

The AC current passing through the resistance and inductance is as follows:

$$\begin{bmatrix} I_d \\ I_q \\ I_0 \end{bmatrix} = \frac{2}{3} \begin{bmatrix} \cos(\theta) & \cos(\theta - \frac{2\pi}{3}) & \cos(\theta + \frac{2\pi}{3}) \\ \sin(\theta) & \sin(\theta - \frac{2\pi}{3}) & \sin(\theta + \frac{2\pi}{3}) \\ \frac{1}{2} & \frac{1}{2} & \frac{1}{2} \end{bmatrix} \begin{bmatrix} I_a \\ I_b \\ I_c \end{bmatrix} \quad (3\text{-}5)$$

The voltage across the inductor in Equation (3-1) should be applied to each current separately. Moreover, the time derivative of the voltage of the inductor in the $dq$ reference frame requires to consider $\frac{d\theta}{dt} = \omega$, where $\omega$ is the angular frequency of the fundamental component in the AC grid. Therefore,

$$\begin{bmatrix}\frac{dI_d}{dt}\\ \frac{dI_q}{dt}\end{bmatrix}=\frac{2}{3}\begin{bmatrix}\cos(\theta) & \cos(\theta-\frac{2\pi}{3}) & \cos(\theta+\frac{2\pi}{3})\\ \sin(\theta) & \sin(\theta-\frac{2\pi}{3}) & \sin(\theta+\frac{2\pi}{3})\end{bmatrix}\begin{bmatrix}\frac{dI_a}{dt}\\ \frac{dI_b}{dt}\\ \frac{dI_c}{dt}\end{bmatrix}$$
$$-\frac{2}{3}\omega\begin{bmatrix}\sin(\theta) & \sin\left(\theta-\frac{2\pi}{3}\right) & \sin\left(\theta+\frac{2\pi}{3}\right)\\ \cos(\theta) & \cos\left(\theta-\frac{2\pi}{3}\right) & \cos\left(\theta+\frac{2\pi}{3}\right)\end{bmatrix}\begin{bmatrix}I_a\\ I_b\\ I_c\end{bmatrix} \quad (3\text{-}6)$$
$$=\frac{2}{3}\begin{bmatrix}\cos(\theta) & \cos(\theta-\frac{2\pi}{3}) & \cos(\theta+\frac{2\pi}{3})\\ \sin(\theta) & \sin(\theta-\frac{2\pi}{3}) & \sin(\theta+\frac{2\pi}{3})\end{bmatrix}\begin{bmatrix}\frac{dI_a}{dt}\\ \frac{dI_b}{dt}\\ \frac{dI_c}{dt}\end{bmatrix}-\frac{2}{3}\omega\begin{bmatrix}I_q\\ I_d\end{bmatrix}$$

The two parts in Equation (3-6) are the two expressions that can describe the current of the AC side of the converter station, as follows:

$$\frac{dI_d}{dt}=\frac{V_{x,d}-V_{r,d}}{L}-\frac{R}{L}I_d-\omega I_q \quad (3\text{-}7)$$

and,

$$\frac{dI_q}{dt}=\frac{V_{x,q}-V_{r,q}}{L}-\frac{R}{L}I_q-\omega I_d \quad (3\text{-}8)$$

The apparent power of the VSC-HVDC station can be written as follows:

$$S_{dq}=\frac{3}{2}((V_dI_d)-j(V_qI_q)) \quad (3\text{-}9)$$

The active power injected to (and/or absorbed from) the AC grid is as follows:

$$P_{DC}=\frac{3}{2}(V_{x,d}I_d+V_{x,q}I_q) \quad (3\text{-}10)$$

The inner controller of the VSC-HVDC station can be implemented using Equation (3-1), which includes minimizing the inductance effect by a feedforward crossing term in

the controller term. Using the PI controller, the dominant poles of VSC-HVDC station can be canceled by zeros of the PI controller. The nonlinear term in Equation (3-1) causes the static error at the steady-state. Therefore, using the PI controller with the feedback of the instantaneous value of $I_d$ and $I_q$, both current vectors can be regulated. Correspondingly, the nonlinear term can be traced by $I_d^*$ and $I_q^*$ in the inner control loop with $I_d$ and $I_q$. It should be noted that $I_d^*$ and $I_q^*$ are the reference current of the $d$-axis and $q$-axis current controllers, respectively.

$$L\frac{dI_d}{dt} = (K_P + \frac{K_i}{s})(I_d^* - I_d) \tag{3-11}$$

and,

$$L\frac{dI_q}{dt} = (K_P + \frac{K_i}{s})(I_q^* - I_q) \tag{3-12}$$

Substituting Equations (3-11) and (3-12) in Equation (3-1), the inner current controller loops of the VSC-HVDC station can be expressed as follows:

$$\left(K_P + \frac{K_i}{s}\right)\begin{bmatrix} I_d^* - I_d \\ I_q^* - I_q \end{bmatrix} = \begin{bmatrix} V_{x,d} \\ V_{x,q} \end{bmatrix} - \begin{bmatrix} V_{r,d} \\ V_{r,q} \end{bmatrix} - R\begin{bmatrix} I_d \\ I_q \end{bmatrix} - \omega L\begin{bmatrix} I_q \\ I_d \end{bmatrix} \tag{3-13}$$

This method is called the decoupled current control strategy.

At the same time, two of the following types of the outer controller can be applied to control the VSC-HVDC station.

- Active Power Flow Controller

The $dq$ reference frame is selected in a direction such that the $d$-axis is in the same phase as the voltage of the AC source. Therefore,

$$V_{x,q} = 0 \tag{3-14}$$

Hence, Equation (3-10) can be rewritten as follows:

$$P_{DC} = \frac{3}{2} V_{x,d} I_d \tag{3-15}$$

Equation (3-15) suggests that the active power flow can be controlled using $I_d$, and correspondingly, the output of the active power flow controller is $I_d^*$.

- DC Voltage Controller

Neglecting the converter losses and considering $P_i$ as the power transferred from the AC side to the DC side, and $P_{DC}$ and $P_{Capacitor}$ as the power flowing into the DC grid and the DC capacitor, respectively, the active power balance of VSC-HVDC station can be written as follows:

$$P_i = P_{DC} + P_{Capacitor} \tag{3-16}$$

where,

$$P_{DC} = V_{DC} I_{DC} \tag{3-17}$$

and,

$$P_{Capacitor} = V_{DC} I_{Capacitor} \tag{3-18}$$

Accordingly,

$$I_{Capacitor} = C \frac{dV_{DC}}{dt} \tag{3-19}$$

Therefore, the differential equation of the DC voltage can be rewritten as:

$$C \frac{dV_{DC}}{dt} = \frac{3 V_{x,d} I_d}{2 V_{DC}} - I_{DC} \tag{3-20}$$

where $C$ is the capacitance of the DC-link capacitor.

Equation (3-20) shows that the DC voltage can be controlled using $I_d$. Although $I_{DC}$ can be represented as a feedforward control in the DC voltage controller, the DC

voltage can be controlled without using a feedforward control loop. The reason is that the PI controller is capable of maintaining the DC voltage constant.

According to the above-mentioned explanations, figure 3.2 shows the complete block diagram of the active power flow and DC voltage controllers of the VSC-HVDC station.

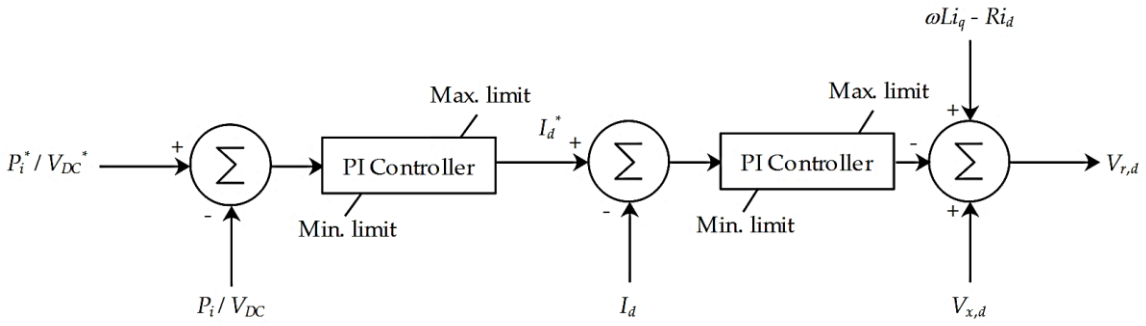


**Figure 3.2.** The complete block diagram of the active power flow and DC voltage controllers

- Reactive Power Flow Controller

Reactive power flow equation can be written as follows:

$$Q_{dq} = -\frac{3}{2} V_{x,d} I_q \tag{3-21}$$

Equation (3-21) suggests that the reactive active power flow can be controlled using $I_q$. As a result, the output of the reactive active power controller is $I_q^*$.

- AC Voltage Controller

The same as the DC voltage control, the AC voltage can be controlled using the reference and measured AC voltage signals. The output of this controller is $I_q^*$. Also, the AC voltage can be controlled with a feedforward control loop. Figure 3.3 demonstrates the complete block diagram of the reactive power flow and AC voltage controllers of the VSC-HVDC station.

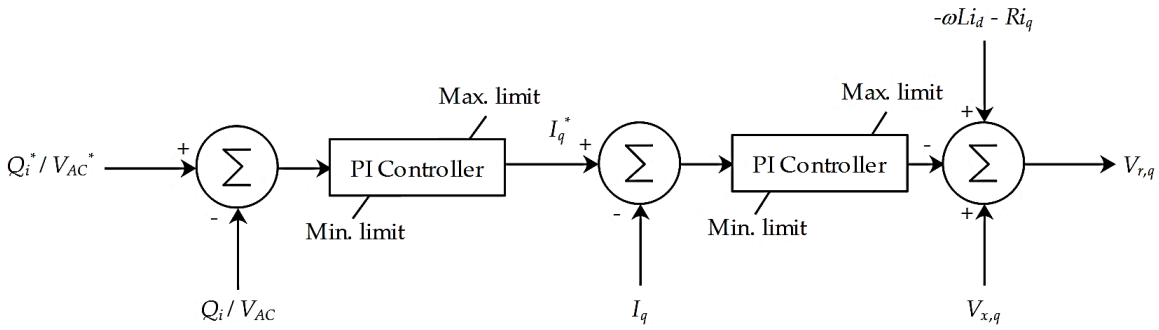


**Figure 3.3.** The complete block diagram of the reactive power flow and AC voltage controllers

It should be noted that equipping the outer controllers with the droop-based controllers balances the power and enforces the stability of MT-HVDC systems.

- DC Voltage-Droop Controller

The $V_{DC}$-droop control strategy is applied, when two or more VSC-HVDC stations in MT-HVDC system have to regulate the DC voltage according to their predetermined $V_{DC}$ -droop characteristics. In other words, the $V_{DC}$ -droop control strategy enables instantaneous balancing power in the DC grids.

$$\Delta P^*_{V_{DC}} = \frac{1}{K_{V_{DC}}}(V^*_{DC} - V_{DC}) \tag{3-22}$$

where $\Delta P^*_V$ is the power reference deviation generated by the $V_{DC}$-droop controller, $V^*_{DC}$ is the reference voltage, and $K_V$ represents the $V_{DC}$-droop parameter ($K_V < 0$).

$\Delta P^*_V > 0$ shows the power injection from the DC grid to the AC grid.

- Frequency-Droop Control

A converter station equipped with the $f$-droop controller participates in the frequency regulation of the AC grid that it is connected to and modifies the $P_{ref}$ according to its predetermined $f$-droop characteristics.

$$\Delta P^*_f = \frac{1}{K_f}(f^* - f) \tag{3-23}$$

where $\Delta P_f^*$ is the power reference deviation generated by the $f$-droop controller, $f^*$ is the reference frequency, and $K_f$ is the $f$-droop parameter ($K_f > 0$).

$\Delta P_f^* > 0$ shows the power injection from the DC grid to the AC grid.

The Power Factor (PF) of the VSC-HVDC station should always be close to one to synchronize the power transfer into the AC grid. Synchronizing the AC voltage of the converter station with the AC voltage of the grid and comparing it with zero (as the steady-state error in voltage reference in the $q$-axis) leads to Equation (3-14). Using the PLL, the displacement angle between the Clark and Park vectors can be obtained and consequently, the frequency of the AC voltage of the converter station becomes equal to the frequency of the AC grid. It should be noted that to transform from the three-phase voltage into the $dq$ reference frame, the displacement angle is needed for matrix multiplication. Figure 3.4 shows the extraction of the displacement angle from the three-phase voltage. Technically, a complete PLL has three back-to-back components, which are the voltage controlled oscillator, the phase detector, and the loop filter.

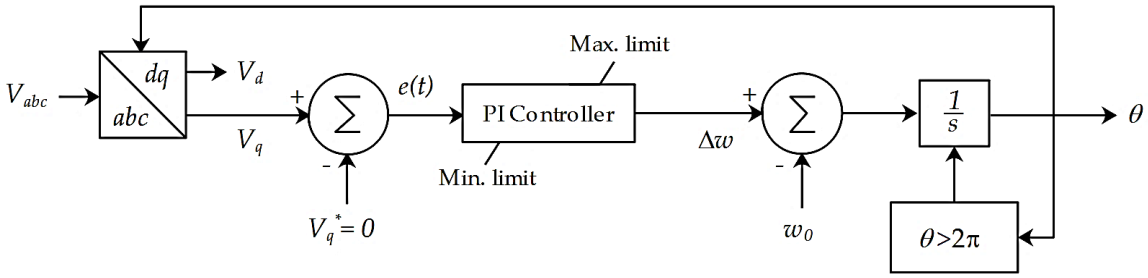


**Figure 3.4.** The PLL control diagram

### *3.2. Proposed Improved Droop-Based Control Strategy for MT-HVDC Systems*

#### *3.2.1. Proposed Improved Droop-Based Control System*

Figures 3.5 and 3.6 show the proposed *improved* droop-based control strategy for MT-HVDC systems, in which $I_d^*$ and $I_q^*$ can be obtained from the two outer controllers. The combination of the droop-based controllers provides a strong DC grid, balances the power, regulates the frequency, and improves the overall stability of the MT-HVDC systems.

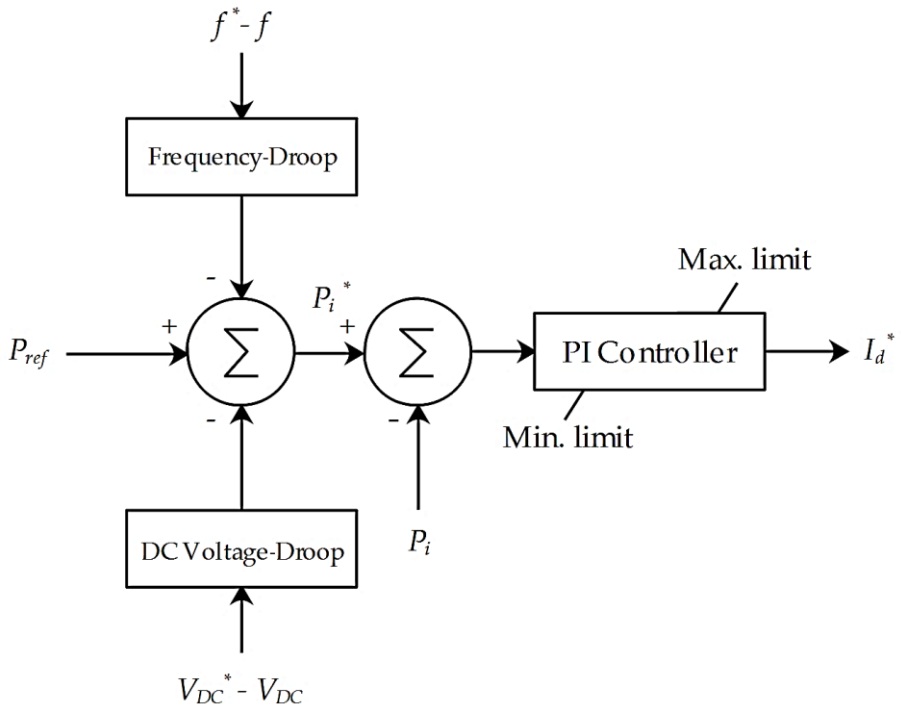


**Figure 3.5.** The proposed improved droop-based outer controller to obtain $I_d^*$

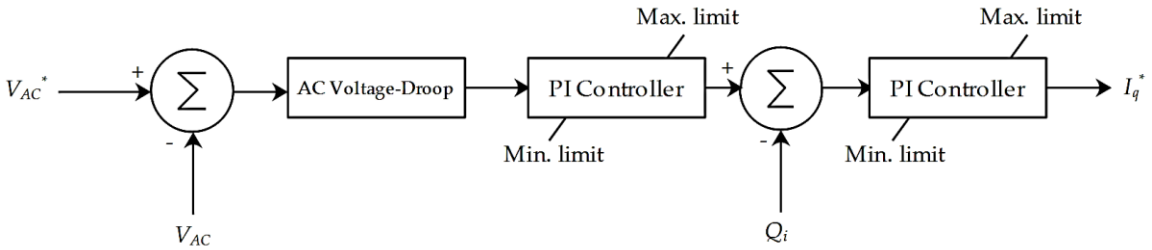


**Figure 3.6.** The proposed improved droop-based outer controller to obtain $I_q^*$

### *3.2.2. Optimal Tuning of the PI Controllers*

Optimal performance of the control loops is achieved by optimal tuning the PI controllers. This leads to a faster response of the system and minimizing the damping oscillations. To increase the cut-off frequency, $\omega_{c.o.}$, of the control loops (with low-order transfer functions), the Modulus Optimum Technique (MOT) is used. Considering a dominant and minor pole in the transfer function, the MOT selects the integral time constant of the PI controller to cancel out the dominant pole.

The Open Loop Transfer Function (OLTF) of the inner current loop is given as follows:

$$OLTF_{inner} = K_{PI}\left(\frac{1+T_{PI}s}{T_{PI}s}\right)\left(\frac{1}{1+T_w s}\right)\frac{1}{R}\left(\frac{1}{1+\tau s}\right) \quad (3\text{-}24)$$

where $K_{PI}$ and $T_{PI}$ are the proportional gain and time constant of the PI controller, respectively. $s$ denotes the Laplace operator, $\tau = \frac{L}{R}$ is the time constant, and $T_w = \frac{1}{2f_s}$ is the time delay of the converter (due to the sinusoidal PWM technique), where $f_s$ is the switching frequency of the converter.

$\tau \gg T_w$ is required to cancel the dominant poles in the external control system. Moreover, considering $T_{PI} = \tau$, and $\omega_{c.o.} \ll \frac{1}{T_w}$, any noise and interference from the switching frequency components can be avoided.

As the unity gain at $\omega_{c.o.}$ is required, Equation (3-25) can lead to determining the proportional gain of the PI controller given in Equation (3-26).

$$|OLTF| = \left|K_{PI}\left(\frac{1}{T_{PI}s}\right)\left(\frac{1}{1+T_w s}\right)\frac{1}{R}\right|_{s=j\omega_{c.o.}} \quad (3\text{-}25)$$

$$K_{PI} = \omega_{c.o.} T_{PI} R|1 + j\omega_{c.o.} T_w| \quad (3\text{-}26)$$

The OLTFs of the DC voltage control loop, active and reactive control loop, and AC voltage control loop are given in Equations (3-27)-(3-29), respectively.

$$OLTF_{V_{DC}} = K_{PI}\left(\frac{1+T_{PI}s}{T_{PI}s}\right)\left(\frac{1}{1+T_{eq}s}\right)\frac{3V_{x,d}}{2V_{DC}}\frac{1}{Cs} \quad (3\text{-}27)$$

$$OLTF_{P/Q} = K_{PI}\left(\frac{1+T_{PI}s}{T_{PI}s}\right)\left(\frac{1}{1+T_{eq}s}\right)\frac{3V_{x,d}}{2} \quad (3\text{-}28)$$

$$OLTF_{V_{AC}} = K_{PI}\left(\frac{1+T_{PI}s}{T_{PI}s}\right)\left(\frac{1}{1+T_{eq}s}\right)\frac{V_{x,d}}{\omega L} \quad (3\text{-}29)$$

where $T_{eq}$ is the total time delay ($T_{eq} = T_{PI} + \tau + T_w$).

Assuming a pole of the OLTF close to the origin or at the origin by itself, the MOT cannot be applied to the control system, and instead, the Symmetrical Optimum (SO)

method is used for specifying the PI controllers. The SO method can maximize the phase margin.

Considering the OLTF of the DC voltage control loop, the phase angle of the DC voltage control loop is given as follows:

$$\angle OLTF_{V_{DC}} = \Phi_m - 180° \tag{3-30}$$

where $\Phi_m$ is the phase margin.

Differentiating the phase margin with respect to the cut-off frequency leads to the following equation.

$$\frac{d\Phi_m}{d\omega_{c.o.}} = \frac{T_{PI}}{1 + (T_{PI}\omega_{c.o.})^2} - \frac{T_{eq}}{1 + (T_{eq}\omega_{c.o.})^2} \tag{3-31}$$

Considering $\omega_{c.o.} = \frac{1}{\sqrt{T_{PI}T_{eq}}}$, $\tan^{-1}(\sqrt{\frac{T_{PI}}{T_{eq}}}) = \alpha$ $(0 < \alpha < 16)$, the phase angle of $\Phi_m$ can be written as follows:

$$\angle\Phi_m = \alpha - (90° - \alpha) \tag{3-32}$$

and accordingly,

$$\sin(\Phi_m) = \sin(2\alpha - 90°) = -\cos(2\alpha) \tag{3-33}$$

Therefore,

$$\sqrt{\frac{T_{PI}}{T_{eq}}} = \tan(\alpha) = \sqrt{\frac{1 - \cos(2\alpha)}{1 + \cos(2\alpha)}} = \sqrt{\frac{1 + \sin(\Phi_m)}{1 - \sin(\Phi_m)}} \tag{3-34}$$

Equation (3-34) results in the integral time constant as follows:

$$T_{PI} = T_{eq}\left(\frac{1 + \sin(\Phi_m)}{1 - \sin(\Phi_m)}\right) = \sigma^2 T_{eq} \tag{3-35}$$

where $\sigma$ is constant number.

As the unity gain at $\omega_{c.o.}$ is required, therefore,

$$\begin{aligned}\left|OLTF_{V_{DC}}\right| &= \left|K_{PI}\left(\frac{1+j\omega_{c.o.}T_{PI}}{j\omega_{c.o.}T_{PI}}\right)\left(\frac{1}{1+j\omega_{c.o.}T_{eq}}\right)\frac{3V_{x,d}}{2V_{DC}}\frac{1}{j\omega_{c.o.}C}\right|_{s=j\omega_{c.o.}} \\ &= \Big|K_{PI}|1 \\ &\quad + j\omega_{c.o.}T_{PI}|\left|\left(\frac{1}{j\omega_{c.o.}T_{PI}-\omega_{c.o.}{}^{2}T_{eq}T_{PI}}\right)\right|\frac{3V_{x,d}}{2V_{DC}}\frac{1}{j\omega_{c.o.}C}\Big| \\ &= K_{PI}\frac{3V_{x,d}}{2V_{DC}}\frac{1}{j\omega_{c.o.}C}=1\end{aligned} \tag{3-36}$$

Hence,

$$K_{PI}=\frac{2V_{DC}}{3V_{x,d}}\omega_{c.o.}C \tag{3-37}$$

### *3.2.3. Operation of the Proposed Improved Droop-Based Control System*

#### *3.2.3.1. Principle and Operation of the Improved Droop-Based Controllers*

Assume the level of the DC voltage in the DC grid decreases. Therefore, the DC voltage-droop controller modifies the amount of power by the VSC-HVDC station. This modification decreases the frequency of the AC grid connected to the VSC-HVDC station and the frequency-droop controller opposed the action of the DC voltage-droop controller and regulates the frequency of the AC grid.

Considering $n$ converters in an MT-HVDC system, then,

$$\Delta V_{DC_i}=\Delta V_{DC},\quad \forall i\in\{1,\dots,n\} \tag{3-38}$$

Assuming an outage of a power generation unit or a significant change in the load level, the active power deviation of all converters equipped with the proposed improved droop-based control strategy based on their reference values is as follows:

$$\sum_{i=1}^{n} \Delta P_i = \sum_{i=1}^{n} \frac{1}{K_{V_{DC_i}}} \left(V_{DC_i}^* - V_{DC_i}\right) + \sum_{i=1}^{n} \frac{1}{K_{f_i}} (f_i^* - f_i) \tag{3-39}$$

As the variation of the power losses is disregarded and due to the fact that the converter equipped with the DC voltage-droop controller balances the power of the DC grid, therefore, $\sum_{i=1}^{n} \Delta P_i = 0$, and the following equation is obtained.

$$\sum_{i=1}^{n} \frac{1}{K_{V_{DC_i}}} \left(V_{DC_i}^* - V_{DC_i}\right) = -\sum_{i=1}^{n} \frac{1}{K_{f_i}} (f_i^* - f_i) \tag{3-40}$$

In other words,

$$\left(V_{DC_i}^* - V_{DC_i}\right) = \frac{-1}{\sum_{i=1}^{n} \frac{1}{K_{V_{DC_i}}}} \sum_{i=1}^{n} \frac{1}{K_{f_i}} (f_i^* - f_i) \tag{3-41}$$

Therefore, the effective active power deviation for the $j^{th}$ converter of the MT-HVDC system is as follows:

$$\Delta P_j = \frac{-1}{K_{V_{DC_j}} \sum_{i=1}^{n} \frac{1}{K_{V_{DC_i}}}} \left( \sum_{i=1}^{n} \frac{1}{K_{f_i}} (f^* - f) \right) + \frac{1}{K_{f_j}} (f_j^* - f_j) \tag{3-42}$$

Equation (3-42) shows the effective active power deviation generated by the frequency-droop controller of the $j^{th}$ converter of the MT-HVDC system. Also, the contribution of the $j^{th}$ converter of the MT-HVDC system participating in the DC voltage regulation of the DC grid depends on $\frac{-1}{K_{V_{DC_j}} \sum_{i=1}^{n} \frac{1}{K_{V_{DC_i}}}}$.

Considering a fault on the AC grid and $k$ converters are connected to the faulty AC grid, as the frequency should be regulated throughout the entire system, the effective active power deviation can be written as follows:

$$\sum_{j=1}^{k} \Delta P_j = \sum_{j=1}^{k} \left( \frac{-\sum_{i=1}^{k} \frac{1}{K_{V_{DC_i}}}}{K_{V_{DC_j}} \sum_{i=1}^{n} \frac{1}{K_{V_{DC_i}}}} + \frac{1}{K_{f_j}} \right) (f_j^* - f_j) \tag{3-43}$$

Assume there is only one VSC-HVDC station connected to the faulty AC grid. Therefore, Equation (3-43) can be rewritten as follows:

$$\Delta P_j = \frac{1}{K_{f_j}} \left(1 - \frac{1}{K_{V_{DC_j}} \sum_{i=1}^{n} \frac{1}{K_{V_{DC_i}}}}\right) (f_j^* - f_j) \tag{3-44}$$

Equation (3-44) shows that the effective frequency-droop parameter, $K'_{f_j}$, which is the ratio of the frequency-droop parameter and the active power deviation for the $j^{th}$ converter of the MT-HVDC system, is not equal to the initial frequency-droop value. Therefore,

$$K'_{f_j} = \frac{(f_j^* - f_j)}{\Delta P_j} = \frac{K_{f_j}}{\left(1 - \frac{1}{K_{V_{DC_j}} \sum_{i=1}^{n} \frac{1}{K_{V_{DC_i}}}}\right)} \tag{3-45}$$

In addition, the AC voltage-droop controller modifies the level of the AC voltage in the AC grid. The reactive power deviation of all converters equipped with the proposed improved droop-based control strategy based on their reference values is as follows:

$$\sum_{i=1}^{n} \Delta Q_i = \sum_{i=1}^{n} \frac{1}{K_{V_{AC_i}}} \left(V_{AC_i}^* - V_{AC_i}\right) \tag{3-46}$$

#### *3.2.3.2. Impact of the Improved Droop-Based Controllers' Limits*

There are limits for the proposed improved droop-based controller. In other words, the droop controller's limits prevent the active power deviation generated by the DC voltage-droop controller, the active power deviation generated by the frequency-droop controller, and the reactive power deviation generated by the AC voltage controller of the

$i^{th}$ converter of the MT-HVDC system from becoming higher than $\pm\Delta P_{V_{DC}i_{max}}$, $\pm\Delta P_{f_{i_{max}}}$, and $\pm\Delta Q_{V_{AC}i_{max}}$, respectively. Therefore,

$$\begin{cases} \Delta P_{V_{DC_i}} = -\Gamma(\Delta V_{DC_i})\min\left\{\left|\frac{1}{K_{V_{DC_i}}}\Delta V_{DC_i}\right|, \Delta P_{V_{DC}i_{max}}\right\} \\ \Delta P_{f_i} = \Gamma(\Delta f_i)\min\left\{\left|\frac{1}{K_{f_i}}\Delta f_i\right|, \Delta P_{f_{i_{max}}}\right\} \\ \Delta Q_{V_{AC_i}} = -\Gamma(\Delta V_{AC_i})\min\left\{\left|\frac{1}{K_{V_{AC_i}}}\Delta V_{AC_i}\right|, \Delta Q_{V_{AC}i_{max}}\right\} \end{cases} \tag{3-47}$$

where for $x \in \mathbb{R}$, $\Gamma(.)$ is defined as follows:

$$\Gamma(x) = \begin{cases} 1, & x > 0 \\ 0, & x = 0 \\ -1, & x < 0 \end{cases} \tag{3-48}$$

In normal operation condition of the MT-HVDC system,

$$\begin{cases} \Delta P_i = -\Gamma(\Delta V_{DC_i})\min\left\{\left|\frac{1}{K_{V_{DC_i}}}\Delta V_{DC_i}\right|, \Delta P_{V_{DC}i_{max}}\right\} + \Gamma(\Delta f_i)\min\left\{\left|\frac{1}{K_{f_i}}\Delta f_i\right|, \Delta P_{f_{i_{max}}}\right\} \\ \Delta Q_{V_{AC_i}} = -\Gamma(\Delta V_{AC_i})\min\left\{\left|\frac{1}{K_{V_{AC_i}}}\Delta V_{AC_i}\right|, \Delta Q_{V_{AC}i_{max}}\right\} \end{cases} \tag{3-49}$$

Therefore, neglecting the possible variation of the active and reactive power losses for $n$ converters, Equation (3-49) can be written as follows:

$$\begin{cases} \Gamma(\Delta V_{DC_i})\sum_{i=1}^{n}\min\left\{\left|\frac{1}{K_{V_{DC_i}}}\Delta V_{DC_i}\right|, \Delta P_{V_{DC}i_{max}}\right\} = \sum_{i=1}^{n}\Gamma(\Delta f_i)\min\left\{\left|\frac{1}{K_{f_i}}\Delta f_i\right|, \Delta P_{f_{i_{max}}}\right\} \\ \Gamma(\Delta V_{AC_i})\sum_{i=1}^{n}\min\left\{\left|\frac{1}{K_{V_{AC_i}}}\Delta V_{AC_i}\right|, \Delta Q_{V_{AC}i_{max}}\right\} = 0 \end{cases} \tag{3-50}$$

Assume $m$ converters are reached $\Delta P_{V_{DC}i_{max}}$. Then, Equation (3-50) can be written as follows:

$$\begin{cases} \Delta V_{DC_i} = \dfrac{1}{\sum_{i=m+1}^{n} \dfrac{1}{K_{V_{DC_i}}}} [-\Gamma(\Delta V_{DC_i}) \sum_{i=1}^{m} \Delta P_{V_{DC_{i_{max}}}} + \sum_{i=1}^{n} \Gamma(\Delta f_i) \min\left\{\left|\dfrac{1}{K_{f_i}} \Delta f_i\right|, \Delta P_{f_{i_{max}}}\right\} \\ \Gamma(\Delta V_{AC_i}) \sum_{i=1}^{n} \min\left\{\left|\dfrac{1}{K_{V_{AC_i}}} \Delta V_{AC_i}\right|, \Delta Q_{V_{AC_{i_{max}}}}\right\} = 0 \end{cases} \quad (3\text{-}51)$$

Considering the $j^{th}$ converter of the MT-HVDC system ($j > m$), and $K_{V_{DC_i}} < 0$ and $K_{f_i} > 0$, substituting Equation (3-51) in Equation (3-49) leads to the following equation.

$$\begin{cases} \Delta P_j = \rho[-\Gamma(\Delta V_{DC_i}) \sum_{i=1}^{m} \Delta P_{V_{DC_{i_{max}}}} + \sum_{i=1}^{n} \Gamma(\Delta f_i) \min\left\{\left|\dfrac{1}{K_{f_i}} \Delta f_i\right|, \Delta P_{f_{i_{max}}}\right\} + \Gamma(\Delta f_j) \min\left\{\left|\dfrac{1}{K_{f_j}} \Delta f_j\right|, \Delta P_{f_{j_{max}}}\right\}] \\ \Gamma(\Delta V_{AC_i}) \sum_{i=1}^{n} \min\left\{\left|\dfrac{1}{K_{V_{AC_i}}} \Delta V_{AC_i}\right|, \Delta Q_{V_{AC_{i_{max}}}}\right\} = 0 \end{cases} \quad (3\text{-}52)$$

where,

$$\rho = \frac{-1}{K_{V_{DC_j}} \sum_{i=m+1}^{n} \dfrac{1}{K_{V_{DC_i}}}} \quad (3\text{-}53)$$

If the maximum power deviation of the $j^{th}$ converter of the MT-HVDC system with regards to the frequency is not reached, the following equation can be derived.

$$\begin{cases} \Delta P_j = \dfrac{1}{K_{f_j}} \left(1 - \dfrac{1}{K_{V_{DC_j}} \sum_{i=m+1}^{n} \dfrac{1}{K_{V_{DC_i}}}} \Delta f_j + \dfrac{\Gamma(\Delta V_{DC_i})}{K_{V_{DC_j}} \sum_{i=m+1}^{n} \dfrac{1}{K_{V_{DC_i}}}} \sum_{i=1}^{m} \Delta P_{V_{DC_{i_{max}}}} \right. \\ \Gamma(\Delta V_{AC_i}) \sum_{i=1}^{n} \min\left\{\left|\dfrac{1}{K_{V_{AC_i}}} \Delta V_{AC_i}\right|, \Delta Q_{V_{AC_{i_{max}}}}\right\} = 0 \end{cases} \quad (3\text{-}54)$$

Based on the above-mentioned explanations, the coupling between the DC voltage-droop and frequency-droop controllers leads to dynamically modifying their droop parameters. This also induces a modification of the dynamics of the MT-HVDC system.

It should be noted that the AC voltage-droop controller is independent and the active power deviation generated by the other droop controllers has no impact on it. The

same strategy as the DC voltage-droop control without the frequency terms is valid for the AC voltage-droop controller.

### *3.3. Results and Discussions*

To validate the performance of the proposed improved droop-based control system, a five-terminal MT-HVDC system consisting of five VSC-HVDC stations connected to different types of AC systems is modeled in PSCAD/EMTDC and MATLAB software. Figure 3.7 shows the configuration of the studied five-terminal MT-HVDC system.

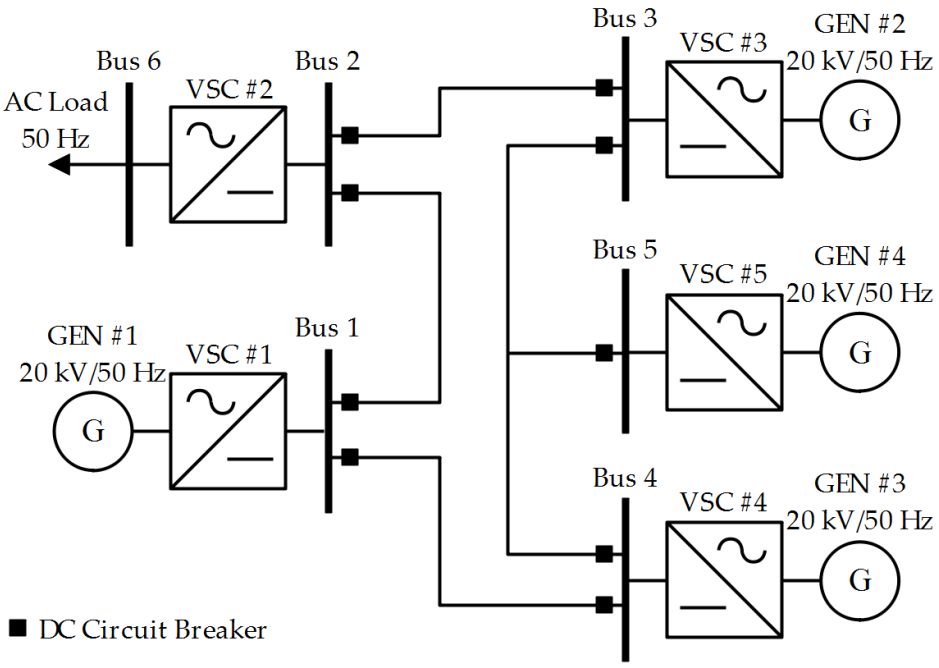


**Figure 3.7.** The configuration of the studied five-terminal MT-HVDC system

For all VSC-HVDC stations, $R = 0.06\,\Omega$, $L = 4.8\,mH$, and $C = 800\,\mu F$. The switching frequency in all VSC-HVDC stations is set to 5 kHz. The DC links between the VSC-HVDC stations are represented by series resistances of 0.01 Ω. To protect the DC grids against the DC faults, two hybrid DC circuit breakers are installed at both ends of each DC link [144].

It is considered that VSC-HVDC stations #1, #2, #3, #4, and #5 are operated in constant DC voltage, constant AC voltage, constant active power, constant active power-AC voltage, and constant DC voltage control modes. It should be noted that VSC-HVDC

station #1 is in converter mode ($Q - V_{DC}$ control (negative power)), VSC-HVDC station #2 is in inverter mode (constant $V_{AC}$ control (positive power)), VSC-HVDC station #3 is in inverter mode (constant $P - Q$ control (positive power)), VSC-HVDC station #4 is in converter mode and ($P - V_{DC}$ control (negative power)), and VSC-HVDC station #5 is in inverter mode ($V_{AC} - V_{DC}$ control (positive power)).

For all the PI controllers of the inner current controllers, the proportional gain and integral time constant are set to 4 and 0.0133, respectively. For VSC-HVDC station #1, the proportional gain and integral time constant of the outer current controller (reactive power controller) are set to -0.43 and 0.0267, respectively. For VSC-HVDC station #2, the proportional gain and integral time constant of the outer current controller (AC voltage regulator) are set to 3 and 0.05, respectively. For VSC-HVDC station #3, the proportional gain and integral time constant of the outer current controllers are set to 0.43 and 0.0267 (for the active power controller) and -0.43 and -0.0267 (for the reactive power controller), respectively. For VSC-HVDC station #4, the proportional gain and integral time constant of the outer current controllers are set to 0.43 and 0.0267 (for the active power controller), 50 and 0.005 (for the AC voltage regulator) and -0.43 and -0.0267 (for the reactive power controller), respectively. For VSC-HVDC station #5, the proportional gain and integral time constant of the outer current controllers are set to 50 and 0.005 (for the AC voltage regulator) and -0.43 and -0.0267 (for the reactive power controller), respectively.

The initial settings of the system are $V_{DC_{ref}}^{VSC-HVDC\#1} = 50\ kV$, $V_{AC_{RMS}}^{VSC-HVDC\#2} = 24.5\ kV$, $P_{ref}^{VSC-HVDC\#3} = 0\ MW$, and $P_{ref}^{VSC-HVDC\#4} = 0\ MW$. It is assumed that at $t = 3\ sec.$, a load of 20 MVA at 1 PF is switched on at Bus 6. Then, at $t = 7\ sec.$, an additional load of 11.4 MW at 0.8 PF is switched on at Bus 6. After that, at $t = 12\ sec.$, $P_{ref}^{VSC-HVDC\#4}$ is set to -50 MW (rectifier mode). Then, At $t = 16\ sec.$, $P_{ref}^{VSC-HVDC\#3}$ is set to 40 MW (inverter mode). At $t = 19\ sec.$, $Q_{ref}^{VSC-HVDC\#3}$ is set to 30 MVAR (reactive power generation). To check the stability of the system, the VSC-HVDC station #1 is disconnected from the system at $t = 24\ sec.$, and lastly, at $t = 29\ sec.$, the VSC-HVDC station #3 is disconnected from the system. To check the performance of the studied system, different scenarios are investigated.

### *3.3.1. Scenario 1: The Case Study with Four VSC-HVDC Stations*

In the first scenario, it is assumed that the VSC-HVDC station #5 is disconnected from the entire system. This is done by keeping the DC breaker at Bus 5 open for the entire simulation time. Therefore, the VSC-HVDC station #1 solely controls the DC voltage in the entire system. Figures 3.8, 3.9, 3.10, and 3.11 show the DC voltage, AC voltage, active power flow, and reactive power flow of the system when the VSC-HVDC station #5 is disconnected from the grid.

As the simulation results demonstrate when the VSC-HVDC station #1 is disconnected from the grid at $t = 24\ sec.$, there is not enough power supply and therefore, the level of the DC voltage drops from 53.18 kV to approximately 36 kV. Also, the disconnection of the VSC-HVDC station #3 from the grid at $t = 29\ sec.$ results in excess power inflow into the MT-HVDC system and in turn leads to increasing the level of the DC voltage from 53.18 kV to 185 kV. The large and continuous deviations in power flow result in deviations in the voltage and frequency and consequently, decreasing the overall stability of the grid [18, 145]. The large oscillations shown in figures 3.8-3.11 show that without considering a backup VSC-HVDC station to regulate the DC voltage, the entire system becomes unstable.

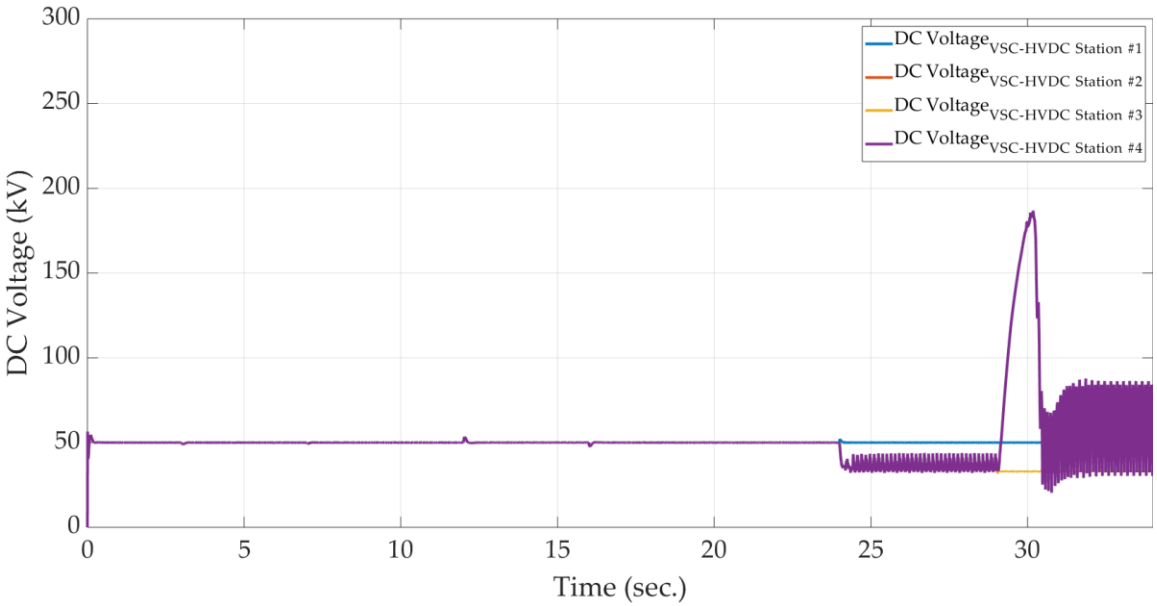


**Figure 3.8.** The DC voltage profile of different VSC-HVDC stations in the first scenario

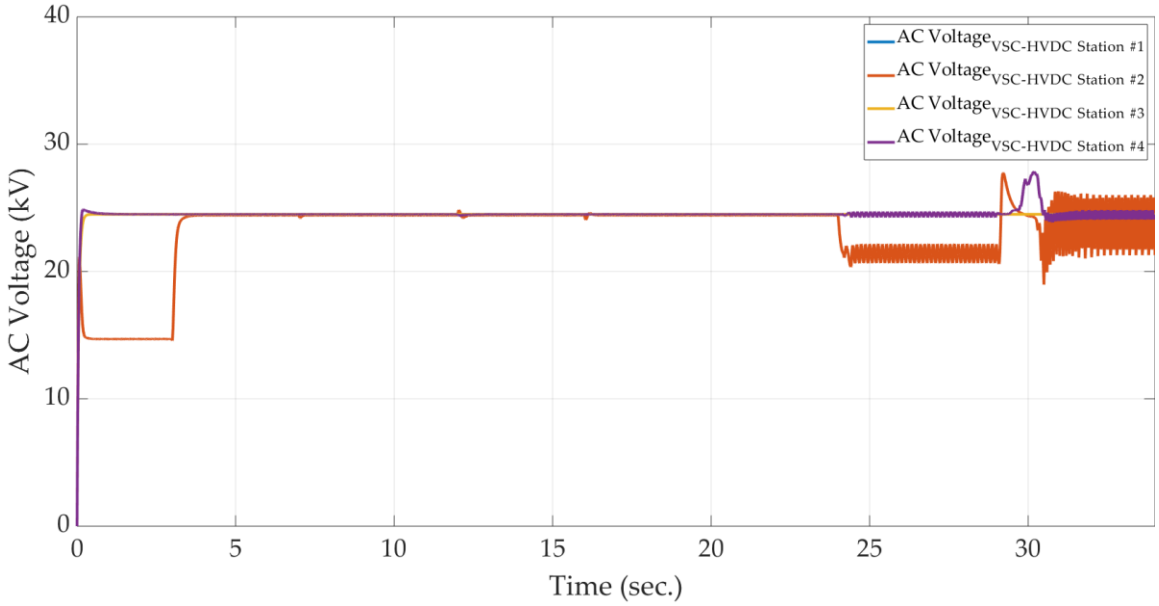


**Figure 3.9.** The AC voltage profile of different VSC-HVDC stations in the first scenario

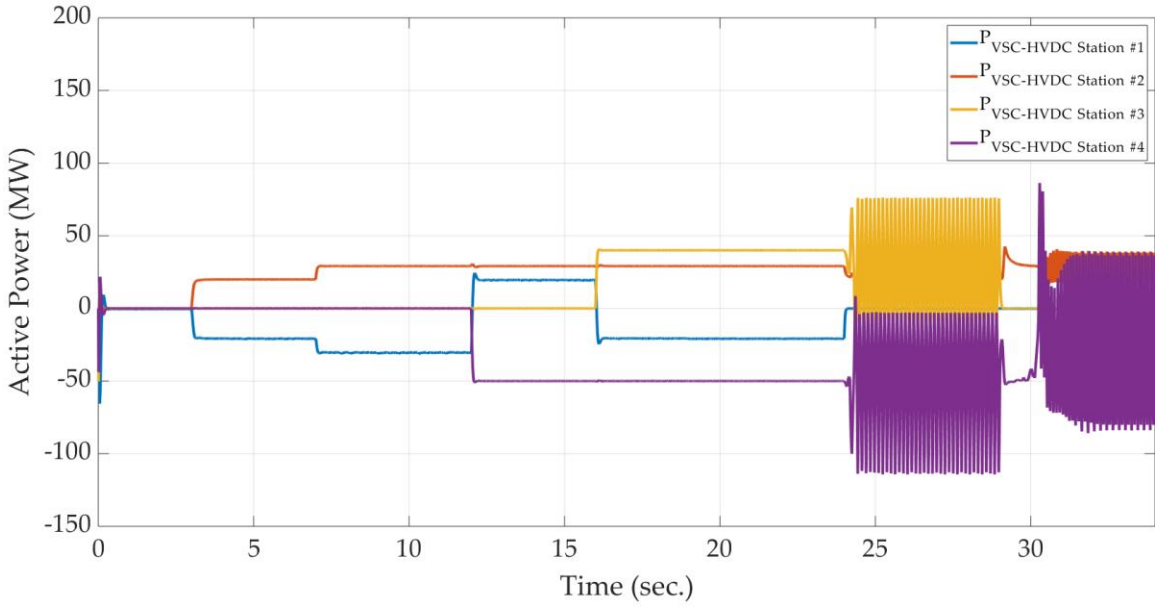


**Figure 3.10.** The active power profile of different VSC-HVDC stations in the first scenario

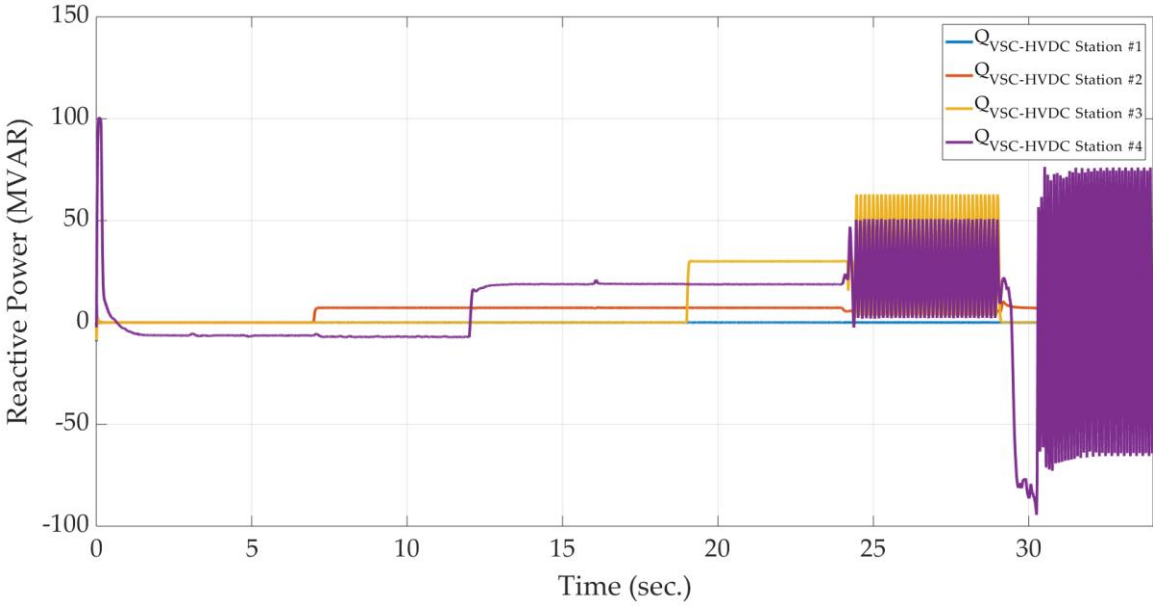


**Figure 3.11.** The reactive power profile of different VSC-HVDC stations in the first scenario

### *3.3.2. Scenario 2: VSC-HVDC #5 Contribution to the DC Voltage Regulation*

In the second scenario, it is assumed that the VSC-HVDC station #5 is connected to the grid to contribute to the DC voltage regulation. Therefore, the reference inputs of the DC voltage controller at VSC-HVDC stations #1 and #5 are the same.

The combination of the DC voltage-droop control and DC margin control enables the power-sharing among VSC-HVDC station in the DC voltage control mode based on a predefined participation factor for each station. The participation factor determines the active power rectified/inverted by a VSC-HVDC station as a fraction of the total power demand/supply in the MT-HVDC system to maintain the level of the DC voltage constant.

For $n$ number of VSC-HVDC stations in the DC voltage-droop control mode, the participation factor ($\chi_i$) of the $i^{th}$ VSC-HVDC station can be calculated as follows:

$$\chi_i = \frac{K_i}{\sum_{j=1}^{n} K_j} \tag{3-55}$$

where $K_i$ and $K_j$ are the proportional gains of the $i^{th}$ and $j^{th}$ VSC-HVDC stations in the DC voltage control mode, respectively.

As only VSC-HVDC stations #1 and #5 regulate the DC voltage, it is assumed that the participation factors of the VSC-HVDC station #1 and #5 are 67% and 33%, respectively.

Accordingly,

$$\chi_{VSC-HVDC\#5} = \frac{K_{VSC-HVDC\#5}}{K_{VSC-HVDC\#1} + K_{VSC-HVDC\#5}} \tag{3-56}$$

In other words, the following droop setting for the VSC-HVDC station #5 should be considered.

$$K_{VSC-HVDC\#5} = \frac{1}{2} K_{VSC-HVDC\#1} \tag{3-57}$$

Figures 3.12, 3.13, 3.14, and 3.15 show the DC voltage, AC voltage, active power flow, and reactive power flow of the system, respectively, when the DC voltage reference setting of VSC-HVDC stations #1, #3, #4, and #5 is 54 kV and the participation factors of the VSC-HVDC stations #1 and #5 are 67%, and 33%, respectively.

As shown in figure 3.12, although the DC voltage of the MT-HVDC system is affected by the disconnection of VSC-HVDC station #1 at $t = 24\ sec.$ and the disconnection of VSC-HVDC station #3 at $t = 29\ sec.$, the steady-state DC voltage is kept within the acceptable range.

Compared to the previous scenario, as there are two VSC-HVDC stations to regulate the DC voltage, the disconnection of the VSC-HVDC stations #1 at $t = 24\ sec.$ and the disconnection of the VSC-HVDC stations #3 at $t = 29\ sec.$ do not prevent power-sharing in hybrid AC/DC grids. Therefore, the system remains stable.

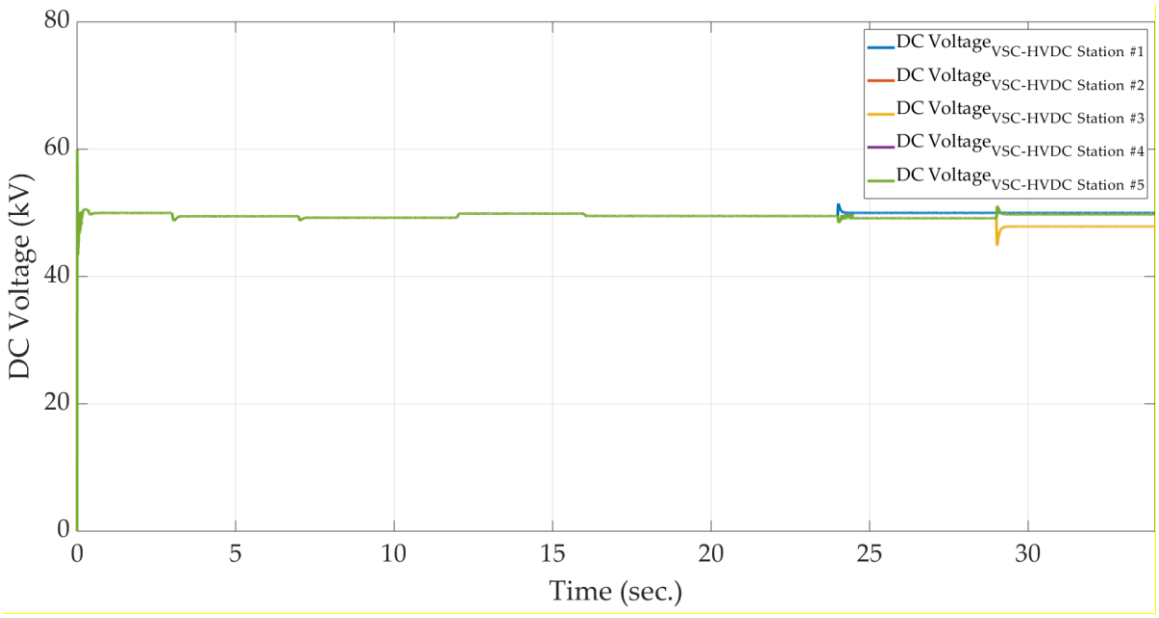


**Figure 3.12.** The DC voltage profile of different VSC-HVDC stations in the second scenario

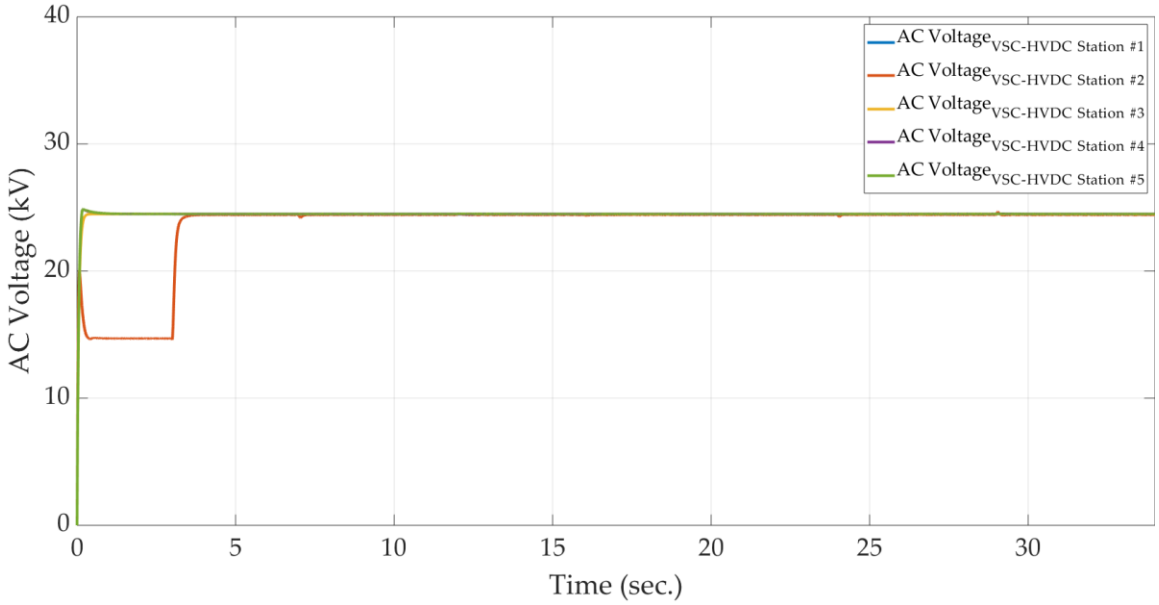


**Figure 3.13.** The AC voltage profile of different VSC-HVDC stations in the second scenario

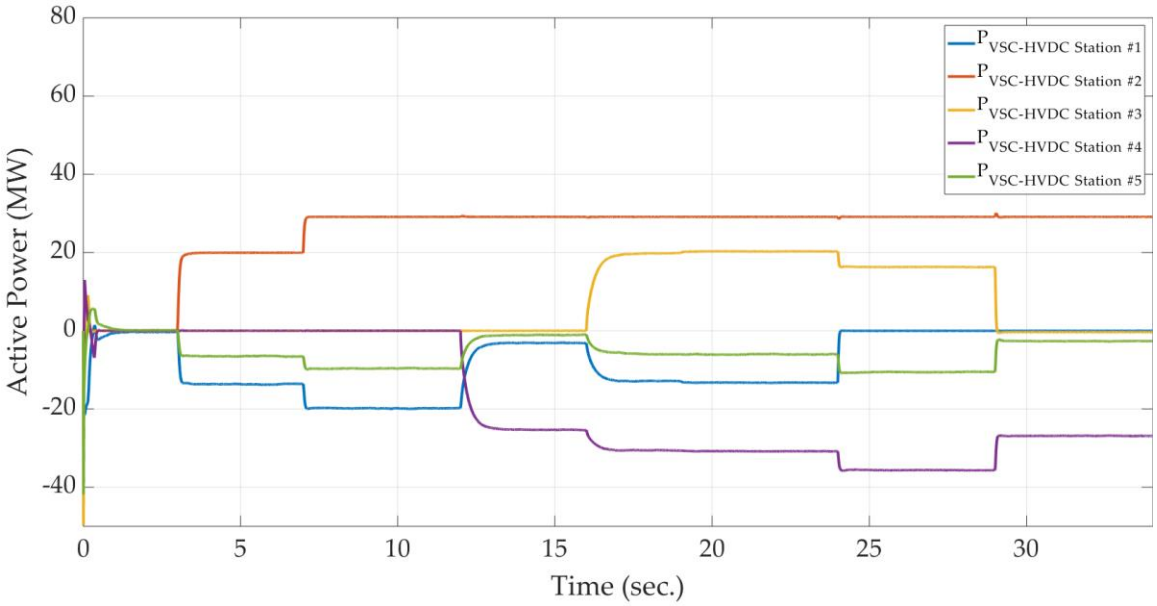


**Figure 3.14.** The active power profile of different VSC-HVDC stations in the second scenario

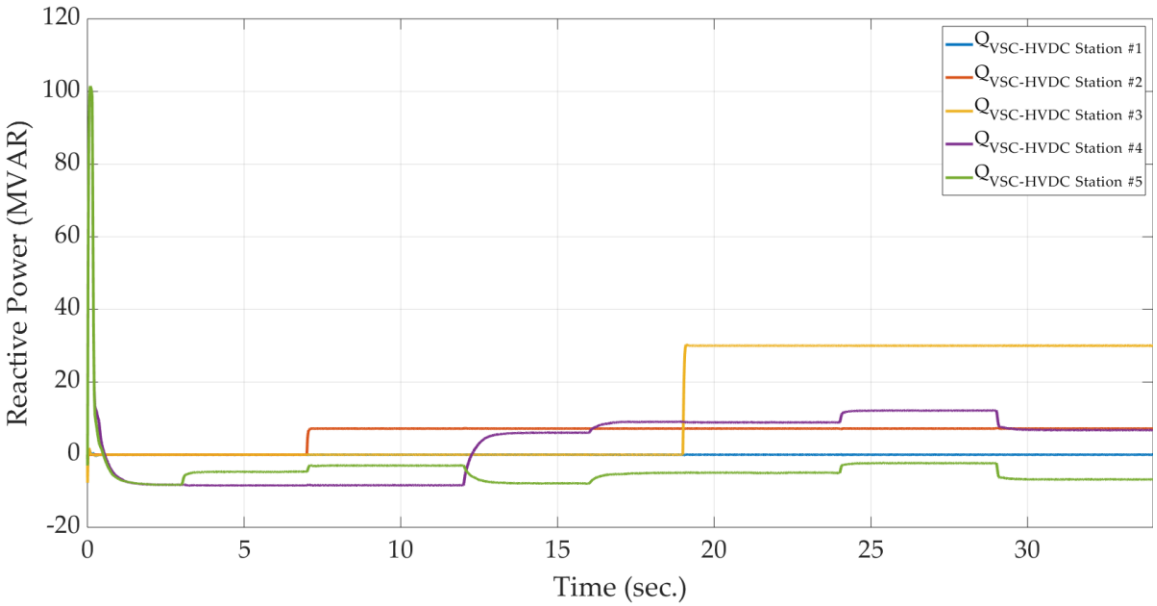


**Figure 3.15.** The reactive power profile of different VSC-HVDC stations in the second scenario

### *3.3.3. Scenario 3: Equipping VSC-HVDC #4 with the Proposed Improved Droop-Based Controller*

In the third scenario, it is assumed that VSC-HVDC station #5 is connected to the grid to contribute to the DC voltage regulation and VSC-HVDC station #4 is equipped with the proposed improved droop-based controller. Hence, the reference inputs of the DC

voltage controller at VSC-HVDC stations #1, #4, and #5 are the same. For VSC-HVDC station #4, the proportional gain and integral time constant of the outer current controllers are set to 0.43 and 0.0267 (for the active power controller), 50 and 0.005 (for the AC voltage regulator) and -0.43 and -0.0267 (for the reactive power controller), respectively.

Figures 3.16, 3.17, 3.18, and 3.19 demonstrate the active power flow, reactive power flow, DC voltage, and AC voltage of the system, respectively, when the DC voltage reference setting of VSC-HVDC stations #1, #3, #4, and #5 is 50 kV and the DC voltage-droop settings of the VSC-HVDC stations #1, #4, and #5 are -2, -0.0001, and -1, respectively. In addition, the frequency and AC voltage-droop settings are set to 0.001 and -0.0001, respectively.

According to the obtained result, changing in the droop settings leads to changes in the power flow and overall stability of the system. Based on figure 3.14, the dominant VSC-HVDC station to supply the active power is the VSC-HVDC station #1. However, employing the proposed improved droop-based controller leads to supplying the majority of the active power by VSC-HVDC station #4.

It should be noted that any changes in the frequency of the AC grid and DC voltage in the DC grid are regulated by injecting active power to the grid. Also, the AC voltage regulation is performed by injecting reactive power to the grid. As shown in figure 3.16, the oscillations in the DC voltage profile after disconnection of VSC-HVDC station #1 at $t = 29\ sec.$ and the disconnection of VSC-HVDC station #3 at $t = 24\ sec.$ are regulated by injecting active power by VSC-HVDC stations #2, #3, and #4. According to the obtained result, the main aim, which is the simultaneous regulation of the frequency, AC voltage, and DC voltage at Bus 4, is achieved.

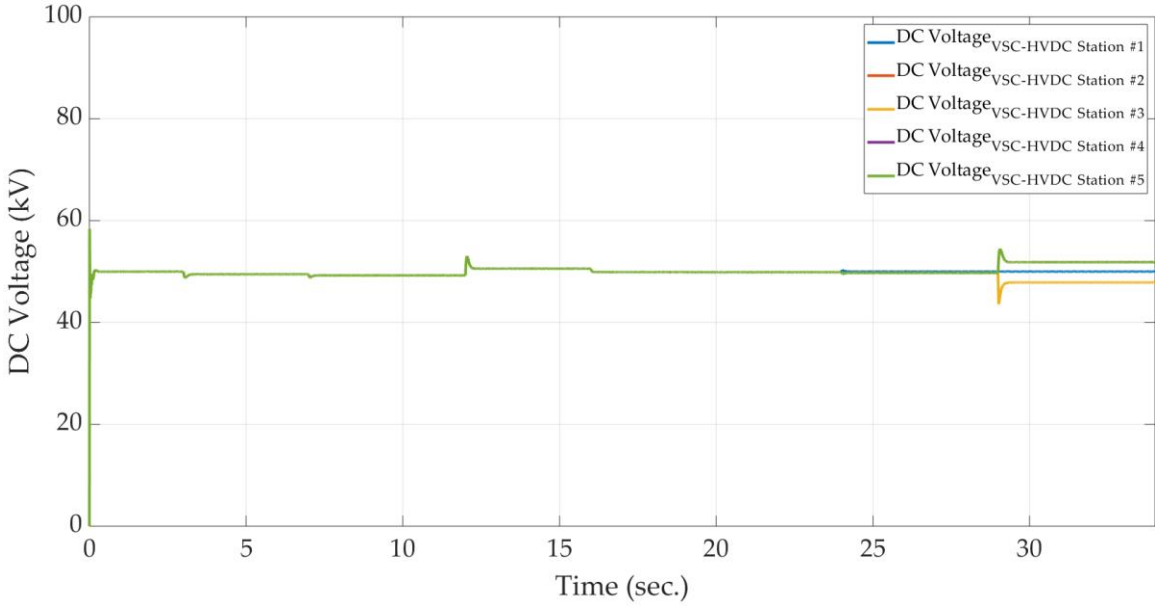


**Figure 3.16.** The DC voltage profile of different VSC-HVDC stations in the second scenario

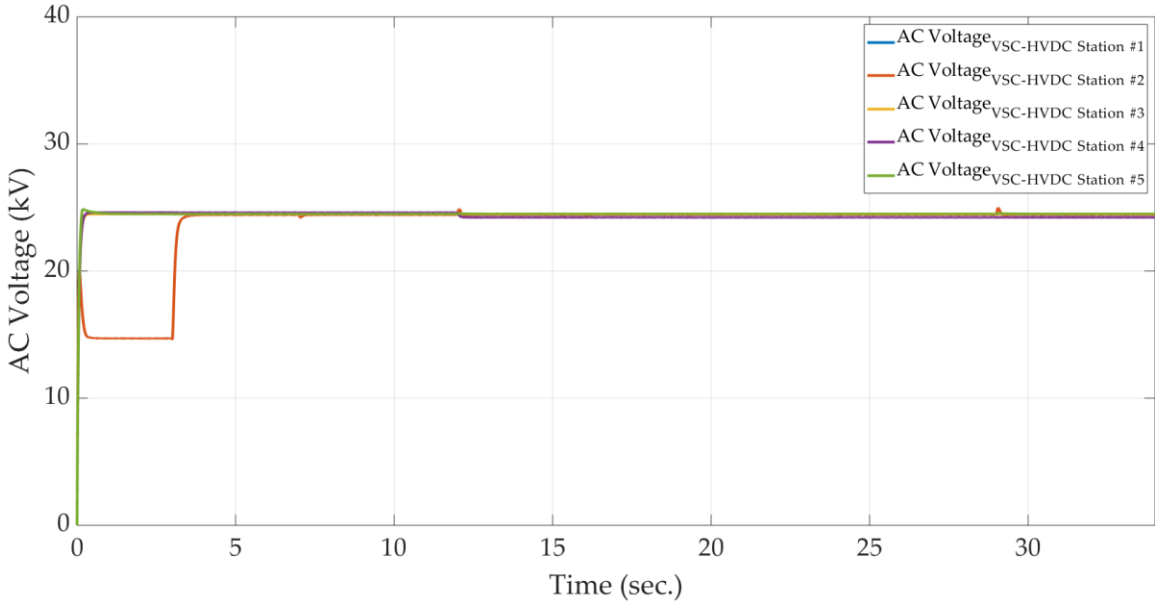


**Figure 3.17.** The AC voltage profile of different VSC-HVDC stations in the third scenario

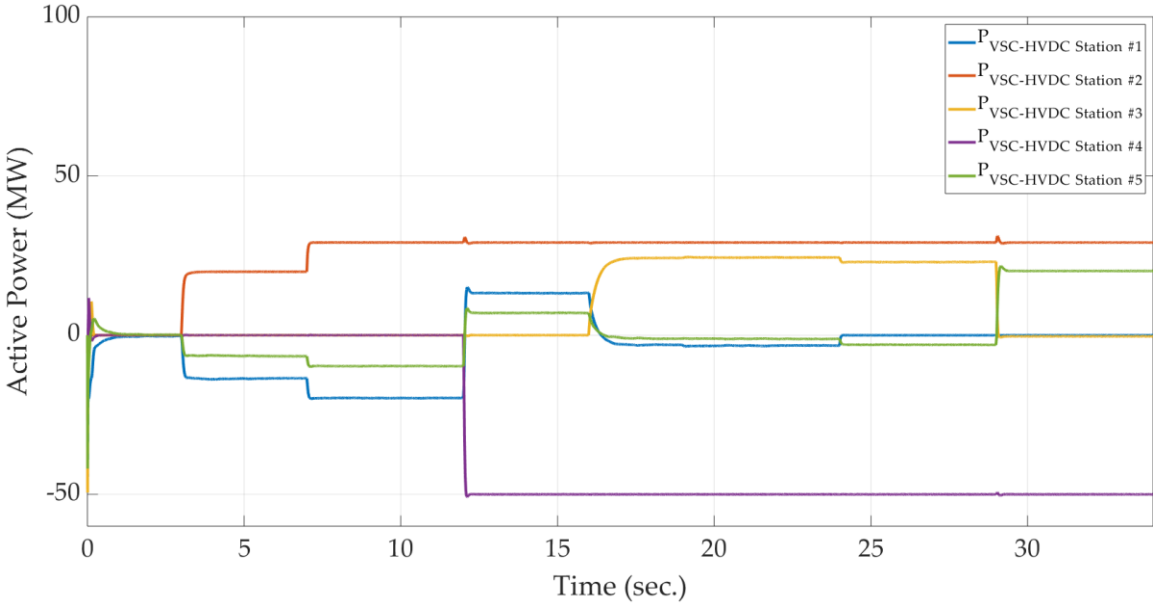


**Figure 3.18.** The active power profile of different VSC-HVDC stations in the third scenario

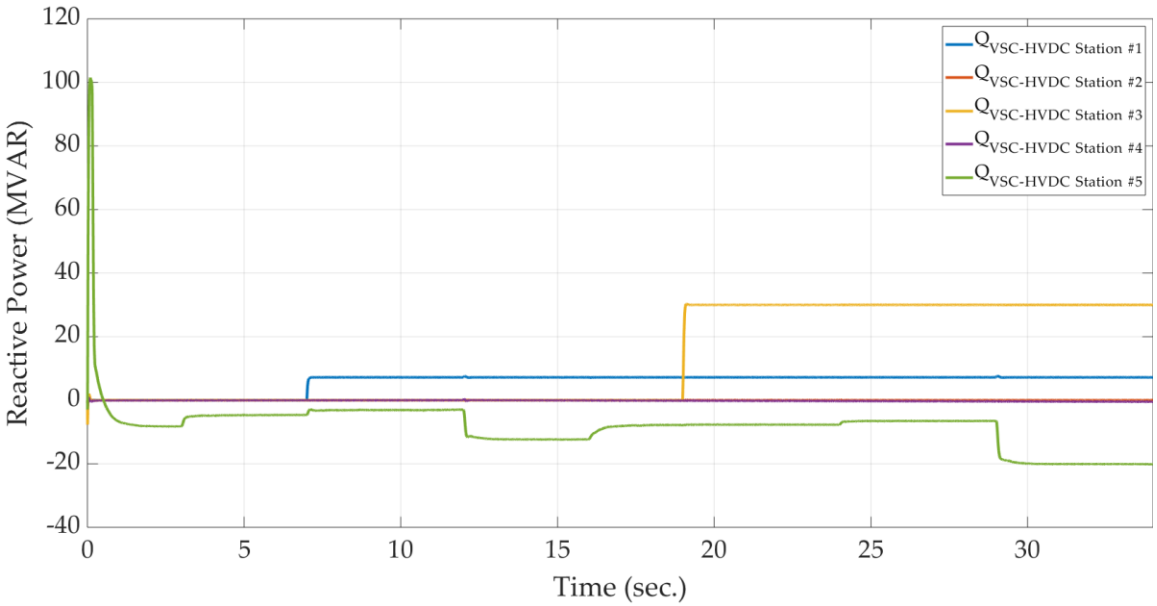


**Figure 3.19.** The active power profile of different VSC-HVDC stations in the third scenario

In order to check the impact of modifying the droop settings of the proposed improved droop-based controller on the active and reactive power flow, different cases are investigated, as shown in table 3.1. In table 3.1, case 1 is the reference case which is studied in Section 3.3.3. Figures 3.20 and 3.21 show the active and reactive power flow of the

VSC-HVDC station #4, which is equipped with the proposed improved droop-based controller, after changing the droop settings based on table 3.1.

**Table 3.1.** Different droop parameters of VSC-HVDC station #4

| | $K_{V_{DC}}$-Droop | $K_{V_{AC}}$-Droop | $f$-Droop |
|---|---|---|---|
| Case 1: Reference Case | -0.0001 | -0.0001 | 0.001 |
| Case 2: Increasing $K_{V_{DC}}$ and $K_{V_{AC}}$-droop parameters | -0.01 | -0.01 | 0.001 |
| Case 3: Increasing $K_{V_{AC}}$-droop parameter | -0.0001 | -0.01 | 0.001 |
| Case 4: Increasing $K_{V_{DC}}$-droop parameter | -0.01 | -0.0001 | 0.001 |
| Case 5: Increasing $f$-droop parameter | -0.0001 | -0.0001 | 0.1 |

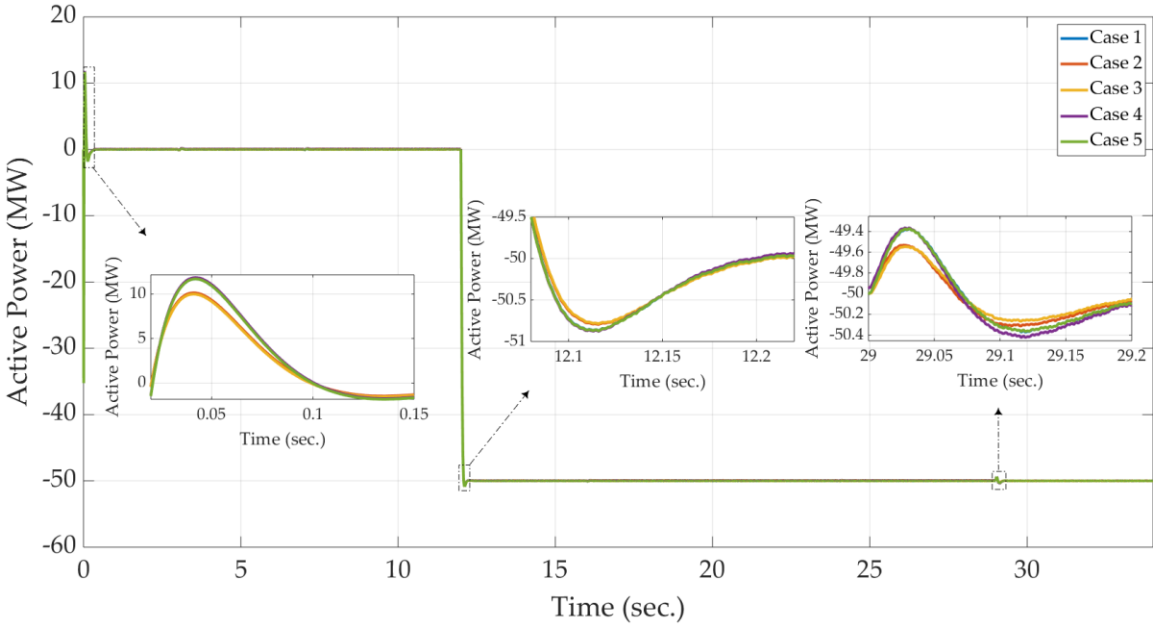


**Figure 3.20.** The impact of modifications of droop settings on the active power profile of VSC-HVDC station #4 in the third scenario

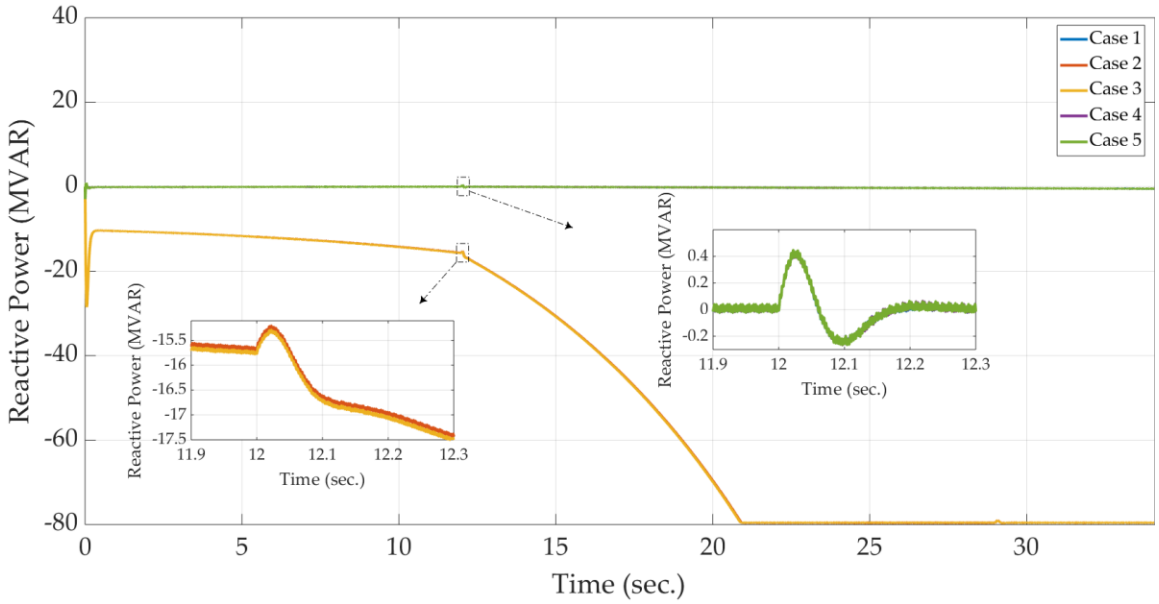


**Figure 3.21.** The impact of modifications of droop settings on the reactive power profile of VSC-HVDC station #4 in the third scenario

### *3.4. Summary*

In this chapter, an improved droop-based control strategy for the active and reactive power-sharing on the large-scale Multi-Terminal High Voltage Direct Current (MT-HVDC) systems is proposed. The equivalent circuit of the Voltage-Sourced Converter (VSC)-HVDC station in the $dq$ reference frame is established and employed for developing an improved droop-based control strategy for the VSC-HVDC station. The proposed improved droop-based control strategy is a communication-free control method in which its droop parameters, consisting of AC voltage-droop, DC voltage-droop, and frequency-droop parameters, are selected optimally. The proposed improved droop-based control strategy is applied to a five-terminal MT-HVDC system to control both the AC and DC grids for a stable-steady state and dynamic performance. In addition, different control strategies of the VSC-HVDC station are investigated in this chapter. Modifications on the droop settings are also performed. The simulation results illustrate that the proposed improved droop-based control strategy not only results in a stable steady stated and dynamic operation of the MT-HVDC system but also is capable of restoring operation during the loss of DC voltage regulating VSC-HVDC station without the need for communication infrastructure. The simulation results validate the robustness and effectiveness of the proposed improved droop-based control strategy.

CHAPTER 4

# *A Mixed AC/DC Power Flow Algorithm for MT-HVDC Systems*

## *4.1. Principles of Power Flow in Power Systems*

### *4.1.1. AC Grid Power Flow*

The main objective of the AC PF is to determine the magnitude and angle at each bus of the AC grids. In order to analyze the AC PF in power systems, the following assumptions are considered.

- The AC transmission networks have fast dynamics compared to the other components. In this regard, AC transmission networks can be represented by algebraic equations.
- Each transmission line and transformer is modeled by an equivalent $\pi$ model.
- The power in AC grids is balanced.
- The positive sequence parameters on a per-phase basis are assumed.

Accordingly, the network equations can be written as follows:

$$\begin{bmatrix} \bar{I}_1 \\ \bar{I}_2 \\ \vdots \\ \bar{I}_i \\ \vdots \\ \bar{I}_{n_{AC}} \end{bmatrix} = \begin{bmatrix} \bar{Y}_{11} & \bar{Y}_{12} & \cdots & \bar{Y}_{1i} & \cdots & \bar{Y}_{1n_{AC}} \\ \bar{Y}_{21} & \bar{Y}_{22} & \cdots & \bar{Y}_{2i} & \cdots & \bar{Y}_{2n_{AC}} \\ \vdots & \vdots & \vdots & \vdots & \vdots & \vdots \\ \bar{Y}_{i1} & \bar{Y}_{i2} & \cdots & \bar{Y}_{ii} & \cdots & \bar{Y}_{in_{AC}} \\ \vdots & \vdots & \vdots & \vdots & \vdots & \vdots \\ \bar{Y}_{n_{AC}1} & \bar{Y}_{n_{AC}2} & \cdots & \bar{Y}_{n_{AC}i} & \cdots & \bar{Y}_{n_{AC}n_{AC}} \end{bmatrix} \begin{bmatrix} \bar{V}_1 \\ \bar{V}_2 \\ \vdots \\ \bar{V}_i \\ \vdots \\ \bar{V}_{n_{AC}} \end{bmatrix} \tag{4-1}$$

where $\bar{I}_i$ and $\bar{V}_i = V_i e^{j\theta_i}$ are the injected current and voltage at the $i^{th}$ node, $\bar{Y}_{ii}$ is the self-admittance at the $i^{th}$ node, $\bar{Y}_{ij}$ is the mutual admittance between nodes $i$ and $j$, and $n_{AC}$ represents the total number of buses in the AC grid.

The voltage of each node can be used for solving the equation of $[\bar{I}] - [\overline{Y_{bus}}][\bar{V}] = 0$. The injected current at the $i^{th}$ node is related to the injected power and bus voltage at that node and it can be calculated as follows:

$$\bar{I}_i = \frac{P_i - jQ_i}{\bar{V}_i^*} \tag{4-2}$$

Considering the operational constraints in power systems, the PF problem becomes nonlinear, and the nodes in AC grids can be classified into four types:

- Slack bus where the voltage magnitude ($V_i$) and angle ($\theta_i$) are determined.
- PV bus where the active power ($P_i$) injected to the grid and the voltage magnitude ($V_i$) are known.
- PQ bus where the active power and reactive power ($Q_i$) injected into the grid are known.
- MT-HVDC Point of Common Coupling (PCC) bus where different constraints based on the control mode of each converter station are applied.

From Equation (4-1), the injected current at the $i^{th}$ node (without considering the PCC buses of MT-HVDC systems) can be written as follows:

$$\bar{I}_i = \sum_{j=1}^{n_{AC}} \overline{Y_{ij} V_j} \tag{4-3}$$

Therefore, the active and reactive power injected to the grid can be derived as follows:

$$P_i = \sum_{j=1}^{n_{AC}} V_i\, V_j [G_{ij} \cos(\theta_i - \theta_j) + B_{ij} \sin(\theta_i - \theta_j)] \tag{4-4}$$

$$Q_i = \sum_{j=1}^{n_{AC}} V_i\, V_j [G_{ij} \sin(\theta_i - \theta_j) - B_{ij} \cos(\theta_i - \theta_j)] \tag{4-5}$$

where $\bar{Y}_{ij} = G_{ij} + jB_{ij}$.

It should be noted that a generator can be either a slack bus or a PV bus, and a load can be a PQ bus with known active and reactive power.

### *4.1.2. MT-HVDC Systems Power Flow*

The main aim of MT-HVDC systems PF is to determine the DC voltage magnitude at each converter station and the PF within the DC grid. Considering $n$ converter stations in MT-HVDC systems, the following items should be considered to derive the PF equations for the $i^{th}$ converter station of MT-HVDC systems.

- Interface of the converter station with the AC grid
- AC side of the converter station
- Interface of the converter station AC and DC sides
- DC side of MT-HVDC systems
- Control modes of the converter station

#### *4.1.2.1. Interface of the Converter Station with the AC Grid*

The PF equations of at the PCC bus of the $i^{th}$ converter station interfacing with the AC grid is as follows:

$$P_{gi} = \sum_{j=1}^{n_{AC}} V_{gi}\, V_j [G_{ij} \cos(\theta_{gi} - \theta_j) + B_{ij} \sin(\theta_{gi} - \theta_j)] \tag{4-6}$$

$$Q_{gi} = \sum_{j=1}^{n_{AC}} V_{gi}\, V_j [G_{ij} \sin(\theta_{gi} - \theta_j) - B_{ij} \cos(\theta_{gi} - \theta_j)] \tag{4-7}$$

where $\bar{V}_{gi} = V_{gi} e^{j\theta_{gi}}$.

#### *4.1.2.2. AC Side of the Converter Station*

The PF equations of at the PCC bus of the $i^{th}$ converter station for the asymmetric bipolar MT-HVDC systems is as follows:

$$P_{gi} - P_{gi}^{p} - P_{gi}^{n} = 0 \tag{4-8}$$

$$Q_{gi} - Q_{gi}^{p} - Q_{gi}^{n} = 0 \tag{4-9}$$

where $P_{gi}^{p}$, $P_{gi}^{n}$, $Q_{gi}^{p}$, and $Q_{gi}^{n}$ are the active and reactive power of the positive and negative poles of the $i^{th}$ converter station, respectively.

Therefore, the apparent power at the PCC bus of the $i^{th}$ converter station by the positive and negative poles can be written as follows:

$$S_{gi}^{p} = \bar{V}_{gi}\bar{I}_{gi}^{p^*} = P_{gi}^{p} + jQ_{gi}^{p} \tag{4-10}$$

$$S_{gi}^{n} = \bar{V}_{gi}\bar{I}_{gi}^{n^*} = P_{gi}^{n} + jQ_{gi}^{n} \tag{4-11}$$

Applying KCL at the PCC bus of the $i^{th}$ converter station leads to deriving the following equation.

$$\bar{I}_{gi} = \bar{I}_{gi}^{p} + \bar{I}_{gi}^{p} \tag{4-12}$$

Using KVL between the PCC bus and the converter terminal of the $i^{th}$ converter station leads to deriving the following equation.

$$\bar{I}_{gi}^{p} = \frac{\bar{V}_{ti}^{p} - \bar{V}_{gi}}{Z_{i}^{p}} = (\bar{V}_{ti}^{p} - \bar{V}_{gi})(G_{i}^{p} + jB_{i}^{p}) \tag{4-13}$$

$$\bar{I}_{gi}^{n} = \frac{\bar{V}_{ti}^{n} - \bar{V}_{gi}}{Z_{i}^{n}} = (\bar{V}_{ti}^{n} - \bar{V}_{gi})(G_{i}^{n} + jB_{i}^{n}) \tag{4-14}$$

where $Z_{i}^{p} = R_{i}^{p} + jX_{i}^{p}$ and $Z_{i}^{n} = R_{i}^{n} + jX_{i}^{n}$. Also, $\bar{V}_{ti}^{p} = V_{ti}^{p}e^{j\theta_{ti}^{p}}$ and $\bar{V}_{ti}^{n} = V_{ti}^{n}e^{j\theta_{ti}^{n}}$ are the voltage of the positive and negative pole converter terminal, respectively.

Substituting Equations (4-13) and (4-14) into Equations (4-10) and (4-11), and also separating the active and reactive power, the following equations are obtained.

$$P_{gi}^{p} = V_{gi}[-V_{gi}G_{i}^{p} + V_{ti}^{p}\{G_{i}^{p}\cos(\theta_{gi} - \theta_{ti}^{p}) + B_{i}^{p}\sin(\theta_{gi} - \theta_{ti}^{p})\}] \tag{4-15}$$

$$Q_{gi}^{p} = V_{gi}[V_{gi}B_{i}^{p} + V_{ti}^{p}\{G_{i}^{p}\sin(\theta_{gi} - \theta_{ti}^{p}) - B_{i}^{p}\cos(\theta_{gi} - \theta_{ti}^{p})\}] \tag{4-16}$$

$$P_{gi}^{n} = V_{gi}[-V_{gi}G_{i}^{n} + V_{ti}^{n}\{G_{i}^{n}\cos(\theta_{gi} - \theta_{ti}^{n}) + B_{i}^{n}\sin(\theta_{gi} - \theta_{ti}^{n})\}] \tag{4-17}$$

$$Q_{gi}^{n} = V_{gi}[V_{gi}B_i^n + V_{ti}^n\{G_i^n \sin(\theta_{gi} - \theta_{ti}^n) - B_i^n \cos(\theta_{gi} - \theta_{ti}^n)\}] \quad (4\text{-}18)$$

#### *4.1.2.3. Interface of the Converter Station AC and DC Sides*

Regardless of the converter station switching losses, the active power balance between converter station AC and DC sides is as follows:

$$P_{ti}^{p} = V_{DCi}^{p} I_{DCi}^{p} \quad (4\text{-}19)$$

$$P_{ti}^{n} = V_{DCi}^{n} I_{DCi}^{n} \quad (4\text{-}20)$$

where $V_{DCi}^{p}$, $I_{DCi}^{p}$, $V_{DCi}^{n}$, and $I_{DCi}^{n}$ are the DC bus voltage and current of the positive and negative pole of the $i^{th}$ converter station.

Also, the active power at the AC-side terminal of the positive and negative pole of the converter stations can be written as follows:

$$P_{ti}^{p} = V_{ti}^{p}[V_{ti}^{p}G_i^p - V_{gi}\{G_i^p \cos(\theta_{ti}^p - \theta_{gi}) + B_i^p \sin(\theta_{ti}^p - \theta_{gi})\} \quad (4\text{-}21)$$

$$P_{ti}^{n} = V_{ti}^{n}[V_{ti}^{n}G_i^n - V_{gi}\{G_i^n \cos(\theta_{ti}^n - \theta_{gi}) + B_i^n \sin(\theta_{ti}^n - \theta_{gi})\} \quad (4\text{-}22)$$

#### *4.1.2.4. DC Side of MT-HVDC Systems*

When the current flowing through the DC-bus capacitor is zero, $I_{DCi}^{p} = I_{Li}^{p}$ and $I_{DCi}^{n} = I_{Li}^{n}$, where $I_{Li}^{p}$ and $I_{Li}^{n}$ are the current of the positive and negative DC link connected to the $i^{th}$ converter station. The injected current can be determined by the conductance matrix of the DC grid. The DC current injection at the positive and negative poles of the DC bus is as follows:

$$\begin{bmatrix} -I_{DC1}^{p} \\ \vdots \\ -I_{DCi}^{p} \\ \vdots \\ -I_{DCN}^{p} \\ -I_{DC1}^{n} \\ \vdots \\ -I_{DCi}^{n} \\ \vdots \\ -I_{DCN}^{n} \end{bmatrix} = \begin{bmatrix} G_{pp11} & \cdots & G_{pp1i} & \cdots & G_{pp1N} & G_{pn11} & \cdots & G_{pn1i} & \cdots & G_{pn1N} \\ \vdots & \vdots & \vdots & \vdots & \vdots & \vdots & \vdots & \vdots & \vdots & \vdots \\ G_{ppi1} & \cdots & G_{ppii} & \cdots & G_{ppiN} & G_{pni1} & \cdots & G_{pnii} & \cdots & G_{pniN} \\ \vdots & \vdots & \vdots & \vdots & \vdots & \vdots & \vdots & \vdots & \vdots & \vdots \\ G_{ppN1} & \cdots & G_{ppNi} & \cdots & G_{ppNN} & G_{pnN1} & \cdots & G_{pnNi} & \cdots & G_{pnNN} \\ G_{np11} & \cdots & G_{np1i} & \cdots & G_{np1N} & G_{nn11} & \cdots & G_{nn1i} & \cdots & G_{np1N} \\ \vdots & \vdots & \vdots & \vdots & \vdots & \vdots & \vdots & \vdots & \vdots & \vdots \\ G_{npi1} & \cdots & G_{npii} & \cdots & G_{npiN} & G_{nni1} & \cdots & G_{nnii} & \cdots & G_{npiN} \\ \vdots & \vdots & \vdots & \vdots & \vdots & \vdots & \vdots & \vdots & \vdots & \vdots \\ G_{npN1} & \cdots & G_{npNi} & \cdots & G_{npNN} & G_{nnN1} & \cdots & G_{nnNi} & \cdots & G_{npNN} \end{bmatrix} \begin{bmatrix} V_{DC1}^{p} \\ \vdots \\ V_{DCi}^{p} \\ \vdots \\ V_{DCN}^{p} \\ V_{DC1}^{n} \\ \vdots \\ V_{DCi}^{n} \\ \vdots \\ V_{DCN}^{n} \end{bmatrix} \quad (4\text{-}23)$$

Hence, the injected current at the $i^{th}$ bus in the DC side is as follows:

$$I_{DCi}^{p} = -\sum_{j=1}^{N} (G_{ppji}\, V_{DCj}^{p} + G_{pnji} V_{DCj}^{n}) \quad (4\text{-}24)$$

$$I_{DCi}^{n} = -\sum_{j=1}^{N} (G_{npji}\, V_{DCj}^{p} + G_{nnji} V_{DCj}^{n}) \quad (4\text{-}25)$$

where $N$ represents the total number of buses in the DC grid. In addition, $G_{ppji}$, $G_{nnji}$, $G_{pnji}$, and $G_{npji}$ are the conductance of the positive and negative DC link between nodes $i$ and $j$, respectively.

#### *4.1.2.5. Control Modes of the Converter Station*

There are different modes of operation for each converter station in MT-HVDC systems [139], and based on them, the steady-state equations in the form of equality

constraints can be obtained. Also, there are some inequality constraints due to the limits, which are imposed by the converter station voltage and current ratings, as follows:

$$V_{DCi}^{\min} \leq V_{DCi} \leq V_{DCi}^{\max} \tag{4-26}$$

$$V_i^{\min} \leq V_i \leq V_i^{\max} \tag{4-27}$$

$$I_{gi} \leq I_{gi}^{\max} \tag{4-28}$$

$$I_{DCi} \leq I_{DCi}^{\max} \tag{4-29}$$

### *4.2. Mixed AC/DC Power Flow Algorithm*

The mixed AC/DC PF algorithm, which is an improved sequential AC/DC PF algorithm [153], can be used to obtain the initial operating points to analyze the dynamics of the hybrid AC/DC grids by solving the AC and DC PF sequentially and keeping both the converter station power and voltage at each node constant.

In order to implement the mixed AC/DC PF algorithm, the per-unit conversion should be performed for the entire system. Each converter station is connected to both AC and DC grids. The AC side of the converter station is modeled by a voltage source connected to the AC bus through a phase reactor ($Z_C = R_C + j\omega L_C$), a capacitor ($Z_F = \frac{-j}{\omega C}$), and a transformer ($Z_{TR} = R_{TR} + j\omega L_{TR}$). Also, the DC side of the converter station is connected to the DC grid. The power losses at the converter station are considered as a quadratic function of the converter station Root Mean Square (RMS) AC current as follows [181]:

$$P_{Loss} = a + bI + cI^2 \tag{4-30}$$

where $a$, $b$, and $c$ are the loss coefficients.

It should be noted that,

$$P_{gi} + P_{DCi} + P_{Lossi} = 0 \tag{4-31}$$

Assume an MT-HVDC system with $n$ converter stations and $n_{DC}$ DC lines. For AC/DC PF analysis, at least one converter station should be capable of controlling $V_{DC}$ (DC-slack bus) in the entire DC grids, and the rest of the converter stations control the active power. The detailed explanations of the mixed AC/DC PF are given as follows:

1. Start by an initial guess of the active power injected to the AC grid by the DC-slack converter station at the $l^{th}$ iteration ($P_{gn_s}^{(l)}$), where $n_s$ represents the index of the DC-slack bus.
2. Transform all converter stations which are connected to the $j^{th}$ bus to PV or PQ buses based on their control modes (including droop-based control strategies) and solve the AC PF. At the $l^{th}$ iteration, the active power injected by all the non-slack converter stations is constant, while $P_{gn_s}^{(l)}$ changes.
3. Calculate the converter station losses using Equation (4-30) considering the active power injected by the $i^{th}$ converter to the AC grid ($P_{gi}^{(l)}$) and the active power injected by the $i^{th}$ converter station to the DC grid ($P_{DCi}^{(l)}$). In this step, the AC/DC connections and the converter stations' limits should be considered.
4. Solve the DC PF for the DC grid using the Newton-Raphson method. In this step, the DC-slack bus regulates the DC voltage ($V_{DCn_s}^{(0)}$) initially, and the DC buses determine the active power injection ($P_{DCi}^{(l)}$). Therefore, the DC voltage at each bus and also $P_{DCn_s}^{(l)}$ are calculated.
5. Compute DC-slack and droop buses iteration ($k$). As a new value of $P_{gn_s}^{(l+1)}$ is calculated, considering the converter station losses,
    I. Initialization: $P_{gn_s}^{(k=0)} = P_{gn_s}^{(l)}$.
    II. Solve the branch $j, n_s - g, n_s$ considering $V_{jns}$, $\theta_{jns}$, $Q_{jns}$, and $P_{gn_s}^{(k)}$ using the Newton-Raphson method.
    III. Obtain the new value of $P_{gn_s}^{(k+1)}$ with $P_{DCns}$ and $P_{Lossns}$ using Equations (4-30) and (4-31).

IV. If $\left|P_{gn_s}^{(k+1)} - P_{gn_s}^{(k)}\right| < \varepsilon$, stop the calculations. Otherwise, $k = k + 1$ and return to step II. The output is $P_{jn_s}^{(k+1)}$.

6. Check the convergence criterion. If $\left|P_{gn_s}^{(k+1)} - P_{gn_s}^{(k)}\right| < \varepsilon$, stop the calculations. Otherwise, $k = k + 1$ and return to step 1.

It should be noted that all linear and nonlinear variables are considered in the mixed AC/DC PF algorithm. Based on the topology of the hybrid AC/DC grids, the rating and length of each transmission line are determined. Also, the droop parameters and reference voltage have a direct impact on the reference power.

### *4.3. Results and Discussions*

For validation and to demonstrate the performance of the mixed AC/DC PF algorithm, a five-bus MT-HVDC system is simulated in MATLAB software, as shown in figure 4.1. The test system is composed of both AC and DC grids. The data of the system is provided in tables 4.1-4.5.

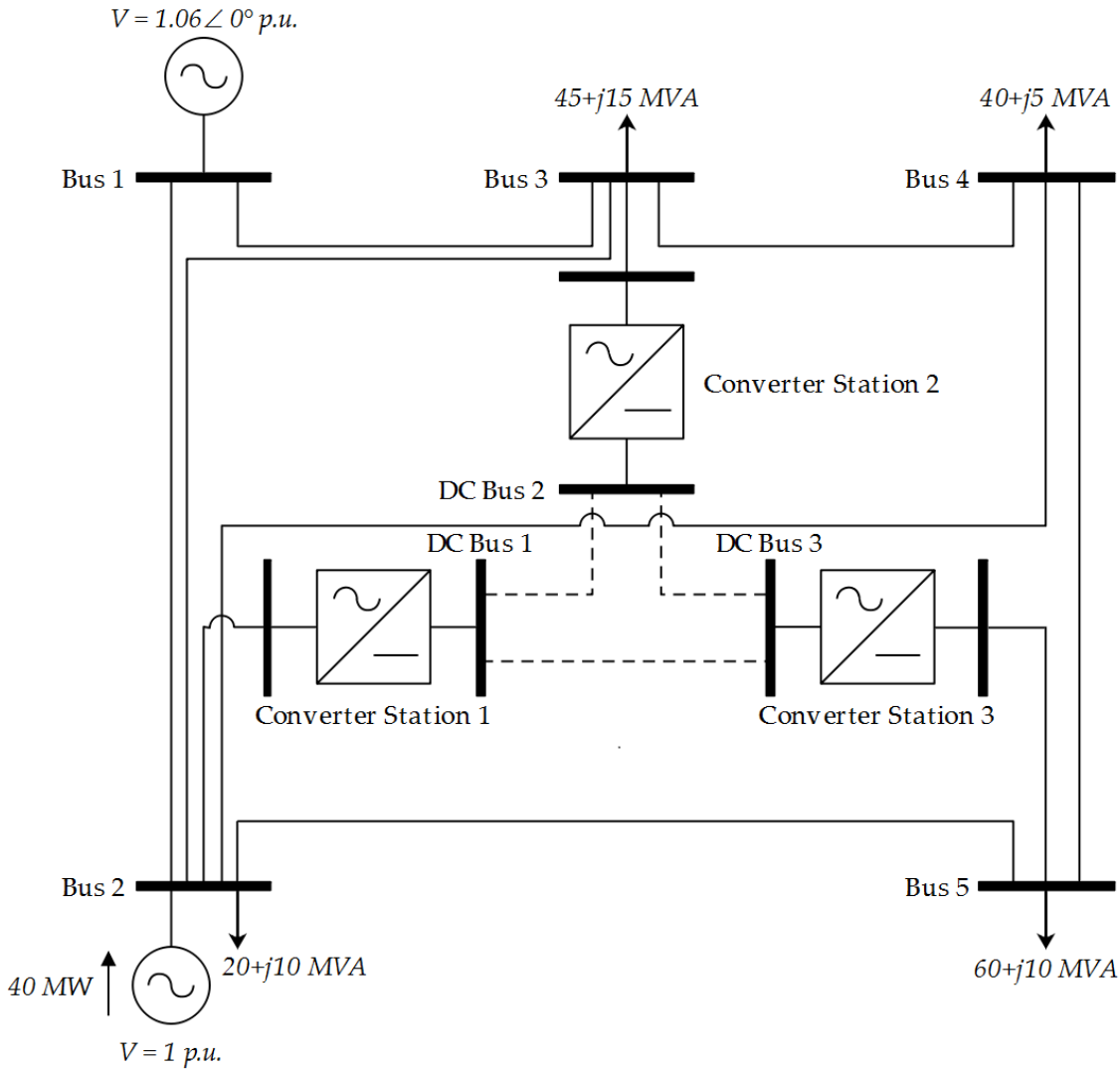


**Figure 0.1.** Single-line diagram of a five-bus MT-HVDC system

**Table 4.1.** Parameters of the AC system

| **Bus** | **Type** | $\boldsymbol{V\ (p.u.)}$ | $\boldsymbol{\theta}$ (°) | $\boldsymbol{P_G\ (MW)}$ | $\boldsymbol{Q_G\ (MVAR)}$ | $\boldsymbol{P_D\ (MW)}$ | $\boldsymbol{Q_D\ (MVAR)}$ |
|---|---|---|---|---|---|---|---|
| 1 | Slack | 1.060 | 0.00 | - | - | 0.00 | 0.00 |
| 2 | PV | 1.000 | - | 40.00 | - | 20.00 | 10.00 |
| 3 | PQ | - | - | - | - | 45.00 | 15.00 |
| 4 | PQ | - | - | - | - | 40.00 | 5.00 |
| 5 | PQ | - | - | - | - | 60.00 | 10.00 |

**Table 4.2.** Parameters of the AC lines

| From | To | $R\ (p.u.)$ | $X\ (p.u.)$ | $B\ (p.u.)$ | $S_N\ (MVA)$ |
|---|---|---|---|---|---|
| 1 | 2 | 0.02 | 0.06 | 0.06 | 100 |
| 1 | 3 | 0.08 | 0.24 | 0.05 | 100 |
| 2 | 3 | 0.06 | 0.18 | 0.04 | 100 |
| 2 | 4 | 0.06 | 0.18 | 0.04 | 100 |
| 2 | 5 | 0.04 | 0.12 | 0.03 | 100 |
| 3 | 4 | 0.01 | 0.03 | 0.02 | 100 |
| 4 | 5 | 0.08 | 0.24 | 0.05 | 100 |

**Table 4.3.** Parameters of the converter stations in per-unit

| Converter Station | $S_N\ (MVA)$ | $R_{TR}$ | $X_{TR}$ | $B_F$ | $R_{TR}$ | $X_{TR}$ |
|---|---|---|---|---|---|---|
| 1 | 100 | 0.0015 | 0.1121 | 0.0887 | 0.0001 | 0.1643 |
| 2 | 100 | 0.0015 | 0.1121 | 0.0887 | 0.0001 | 0.1643 |
| 3 | 100 | 0.0015 | 0.1121 | 0.0887 | 0.0001 | 0.1643 |

**Table 4.4.** Power losses coefficients of the converter stations

| Converter Station | $a$ | $b$ | $c_{rec}$ | $c_{inv}$ |
|---|---|---|---|---|
| 1 | 1.103 | 0.887 | 2.885 | 4.371 |
| 2 | 1.103 | 0.887 | 2.885 | 4.371 |
| 3 | 1.103 | 0.887 | 2.885 | 4.371 |

**Table 4.5.** Parameters of the DC lines

| From | To | $R_{DC}\ (p.u.)$ | $V_{DC}\ (kV)$ | $P_{DC}\ (MW)$ |
|---|---|---|---|---|
| 1 | 2 | 0.0260 | 345 | 100 |
| 1 | 3 | 0.0365 | 345 | 100 |
| 2 | 3 | 0.0260 | 345 | 100 |

The parameters of the converter stations for the PF calculations are as follows:

- Converter Station #1: $P-Q$ control mode, $P_g = -60\ MW$ and $Q_g = -40\ MVAR$
- Converter Station #2: $V_{DC}-V$ control mode, $V_{DC} = 1\ p.u.$ and $V = 1\ p.u.$
- Converter Station #3: $P-Q$ control mode, $P_g = 35\ MW$ and $Q_g = 5\ MVAR$

It should be noted that $S_B = 100\ MVA$, $V_{DC_B} = 345\ kV$, and $V_B = 345\ kV$ are the base values for hybrid AC/DC grids per-unit system.

### *4.3.1. Case 1: AC Power Flow without DC System*

In the first case, the AC PF calculations are performed without considering the DC system. Tables 4.6 and 4.7 show the results of AC PF without DC grids.

**Table 4.6.** Results of AC PF calculations in Case 1. AC bus data

| Bus | Voltage | | Generation | | Load | |
|---|---|---|---|---|---|---|
| | $\|V\|$ $(p.u.)$ | $\theta$ (°) | $P$ | $Q$ | $P$ | $Q$ |
| 1 | 1.060 | 0.000 | 131.12 | 90.82 | - | - |
| 2 | 1.000 | -2.061 | 40.00 | -61.59 | 20.00 | 10.00 |
| 3 | 0.987 | -4.637 | - | - | 45.00 | 15.00 |
| 4 | 0.984 | -4.957 | - | - | 40.00 | 5.00 |
| 5 | 0.972 | -5.765 | - | - | 60.00 | 10.00 |
| | | **Total:** | 171.12 | 29.23 | 165.00 | 40.00 |

* $P$ and $Q$ are in $MW$ and $MVAR$, respectively.

**Table 4.7.** Results of AC PF calculations in Case 1. AC branch data

| Branch | | | From Bus Injection | | To Bus Injection | | Power Losses | |
|---|---|---|---|---|---|---|---|---|
| | From | To | $P$ | $Q$ | $P$ | $Q$ | $P$ | $Q$ |
| 1 | 1 | 2 | 89.33 | 74.00 | -86.85 | -72.91 | 2.486 | 7.46 |
| 2 | 1 | 3 | 41.79 | 16.82 | -40.27 | -17.51 | 1.518 | 4.55 |
| 3 | 2 | 3 | 24.47 | -2.52 | -24.11 | -0.35 | 0.360 | 1.08 |
| 4 | 2 | 4 | 27.71 | -1.72 | -27.25 | -0.83 | 0.461 | 1.38 |
| 5 | 2 | 5 | 54.66 | 5.56 | -53.44 | -4.83 | 1.215 | 3.65 |
| 6 | 3 | 4 | 19.39 | 2.86 | -19.35 | -4.69 | 0.040 | 0.12 |
| 7 | 4 | 5 | 6.60 | 0.52 | -6.56 | -5.17 | 0.043 | 0.13 |
| | | | | | | **Total:** | 6.123 | 18.37 |

* $P$ and $Q$ are in $MW$ and $MVAR$, respectively.

### *4.3.2. Case 2: AC/DC Power Flow Considering Constant Active Power and DC Voltage*

In the second case, the algorithm is applied to solve the AC/DC PF problem for the studied system considering that converter stations #1 and #3 are operated in constant $P$-mode and converter station #2 is operated in constant $V_{DC}$-mode. Tables 4.8-4.12 show the obtained results of the mixed AC/DC PF calculations in Case 2.

**Table 4.8.** Results of the mixed AC/DC PF calculations in Case 2. AC bus data

| Bus | Voltage | | Generation | | Load | |
|---|---|---|---|---|---|---|
| | $\|V\|$ $(p.u.)$ | $\theta$ (°) | $P$ | $Q$ | $P$ | $Q$ |
| 1 | 1.060 | 0.000 | 133.64 | 84.32 | - | - |
| 2 | 1.000 | -2.383 | 40.00 | -32.84 | 20.00 | 10.00 |
| 3 | 1.000 | -3.895 | - | - | 45.00 | 15.00 |
| 4 | 0.996 | -4.262 | - | - | 40.00 | 5.00 |
| 5 | 0.991 | -4.149 | - | - | 60.00 | 10.00 |
| | | **Total:** | 173.64 | 51.48 | 165.00 | 40.00 |

* $P$ and $Q$ are in $MW$ and $MVAR$, respectively.

**Table 4.9.** Results of the mixed AC/DC PF calculations in Case 2. AC branch data

| Branch | | | From Bus Injection | | To Bus Injection | | Power Losses | |
|---|---|---|---|---|---|---|---|---|
| | From | To | $P$ | $Q$ | $P$ | $Q$ | $P$ | $Q$ |
| 1 | 1 | 2 | 98.38 | 71.37 | -95.66 | -69.59 | 2.717 | 8.15 |
| 2 | 1 | 3 | 35.26 | 12.96 | -34.20 | -15.08 | 1.062 | 3.19 |
| 3 | 2 | 3 | 13.25 | -6.22 | -13.14 | 2.57 | 0.116 | 0.35 |
| 4 | 2 | 4 | 17.08 | -5.18 | -16.89 | 1.74 | 0.181 | 0.54 |
| 5 | 2 | 5 | 25.33 | -1.85 | -25.07 | -0.35 | 0.257 | 0.77 |
| 6 | 3 | 4 | 23.09 | 4.64 | -23.04 | -6.47 | 0.057 | 0.17 |
| 7 | 4 | 5 | -0.07 | -0.27 | 0.07 | -4.65 | 0.004 | 0.01 |
| | | | | | | **Total:** | 4.394 | 13.18 |

* $P$ and $Q$ are in $MW$ and $MVAR$, respectively.

**Table 4.10.** Results of the mixed AC/DC PF calculations in Case 2. DC bus data

| Bus DC | Bus AC | Voltage Magnitude (p.u.) | Active Power (MW) |
|---|---|---|---|
| 1 | 2 | 1.008 | -58.627 |
| 2 | 3 | 1.000 | 21.901 |
| 3 | 5 | 0.998 | 36.186 |

**Table 4.11.** Results of the mixed AC/DC PF calculations in Case 2. Converter station data

| Bus DC | Bus Injection | | Converter Voltage | | Total Loss |
|---|---|---|---|---|---|
| | $P$ | $Q$ | $\|V\|$ $(p.u.)$ | $\theta$ (°) | $P$ |
| 1 | -60.00 | -40.00 | 0.890 | -13.017 | 1.37 |
| 2 | 20.76 | 7.14 | 1.007 | -0.655 | 1.14 |
| 3 | 35.00 | 5.00 | 0.995 | 1.442 | 1.19 |
| | | | | **Total:** | 3.70 |

| Bus DC | Converter Power | | Filter | Transformer Loss | | Reactor Loss | | Converter Loss |
|---|---|---|---|---|---|---|---|---|
| | $P$ | $Q$ | $Q$ | $P$ | $Q$ | $P$ | $Q$ | $P$ |
| 1 | -59.22 | -32.63 | -8.12 | 0.08 | 5.83 | 0.01 | 9.66 | 1.29 |
| 2 | 20.76 | -0.65 | -9.02 | 0.01 | 0.54 | 0.00 | 0.70 | 1.14 |
| 3 | 35.02 | -0.37 | -8.83 | 0.02 | 1.43 | 0.00 | 2.03 | 1.17 |
| | | | **Total:** | 0.11 | 7.80 | 0.01 | 12.39 | 3.60 |

| Bus DC | Grid Power | | Trans. Filter Power | | Filter | Conv. Filter Power | Conv. Power | |
|---|---|---|---|---|---|---|---|---|
| | $P$ | $Q$ | $P$ | $Q$ | $Q$ | $Q$ | $P$ | $Q$ |
| 1 | -60.00 | -40.00 | -59.92 | -34.17 | -8.12 | -42.29 | -59.92 | -32.63 |
| 2 | 20.76 | 7.14 | 20.76 | 7.68 | -9.02 | -1.35 | 20.76 | -0.65 |
| 3 | 35.00 | 5.00 | 35.02 | 6.43 | -8.83 | -2.40 | 35.02 | -0.37 |

* $P$ and $Q$ are in $MW$ and $MVAR$, respectively.

**Table 4.12.** Results of the mixed AC/DC PF calculations in Case 2. DC branch data

| Branch | | | From Bus | To Bus | Power Losses |
|---|---|---|---|---|---|
| | From | To | $P$ | $P$ | $P$ |
| 1 | 1 | 2 | 30.66 | -30.42 | 0.24 |
| 2 | 2 | 3 | 8.52 | -8.50 | 0.02 |
| 3 | 1 | 3 | 27.96 | -27.68 | 0.28 |
| | | | | **Total:** | 0.54 |

* $P$ and $Q$ are in $MW$ and $MVAR$, respectively.

Based on the obtained results in tables 4.8-4.12, figures 4.2 and 4.3 show the AC/DC PF solutions under the normal operation.

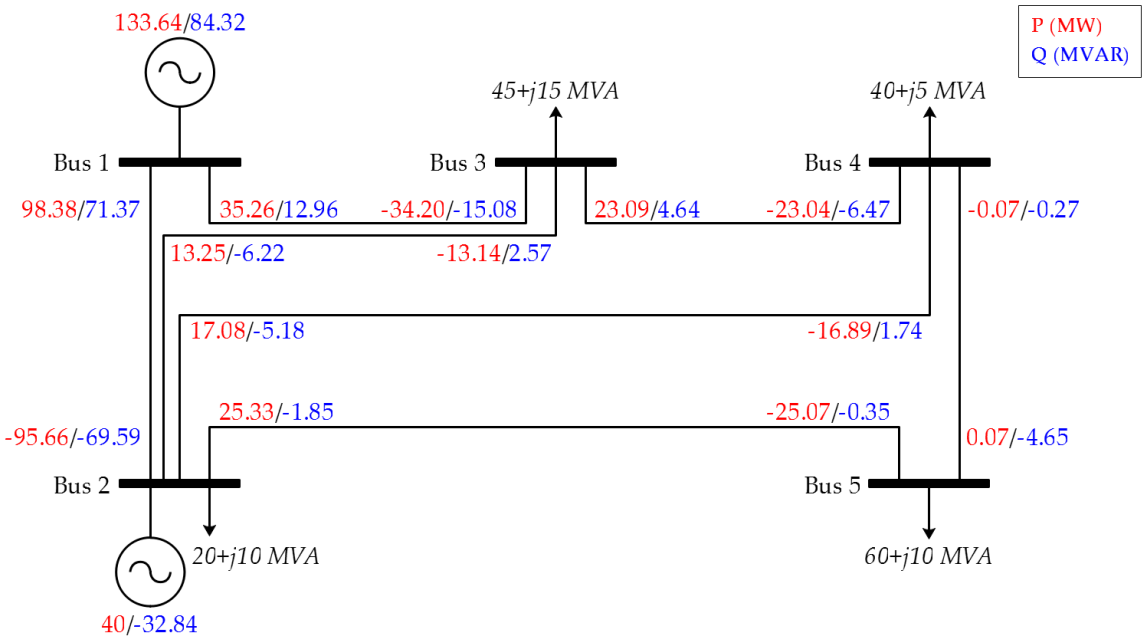


**Figure 4.2.** The AC grid PF solution in Case 2

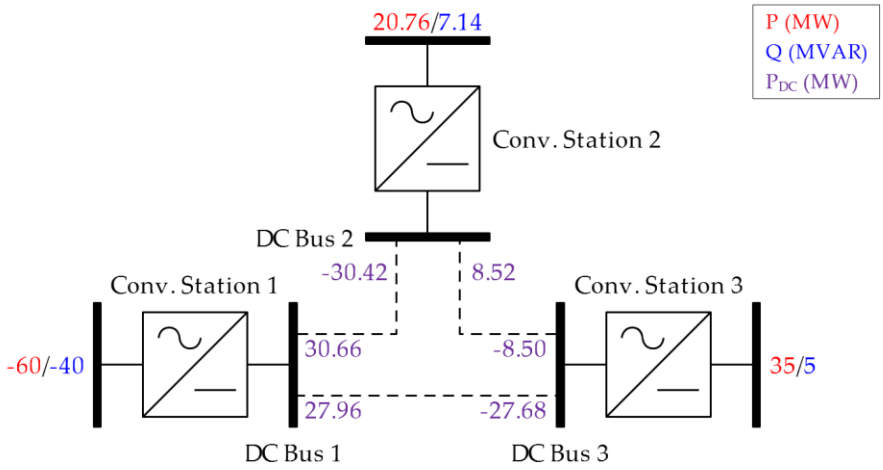


**Figure 4.3.** The AC/DC PF solution of the MT-HVDC system in Case 2

### *4.3.3. Case 3: AC/DC Power Flow Considering Converter Station Outage*

In the third case, the impact of the converter station outage on the AC/DC PF results is analyzed. Figures 4.4 and 4.5 demonstrate the results of PF calculations both in all AC and DC buses and branches in case of the outage of converter station #1. As shown in figure 4.5, converter station #3 is capable of operating in constant *P*-mode.

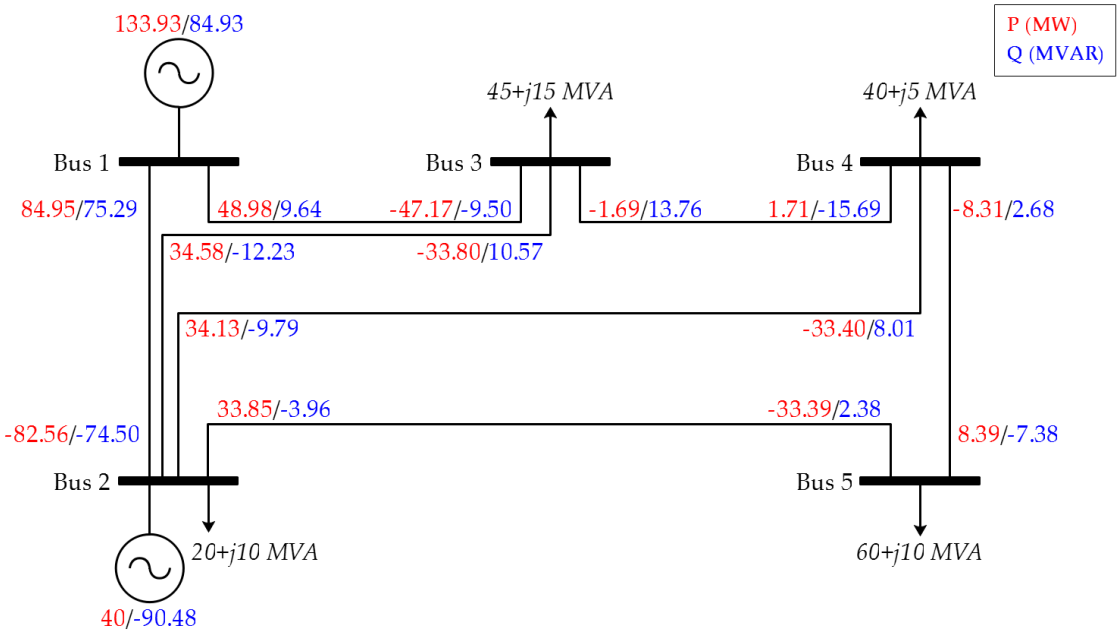


**Figure 4.4.** The AC grid PF solution in Case 3

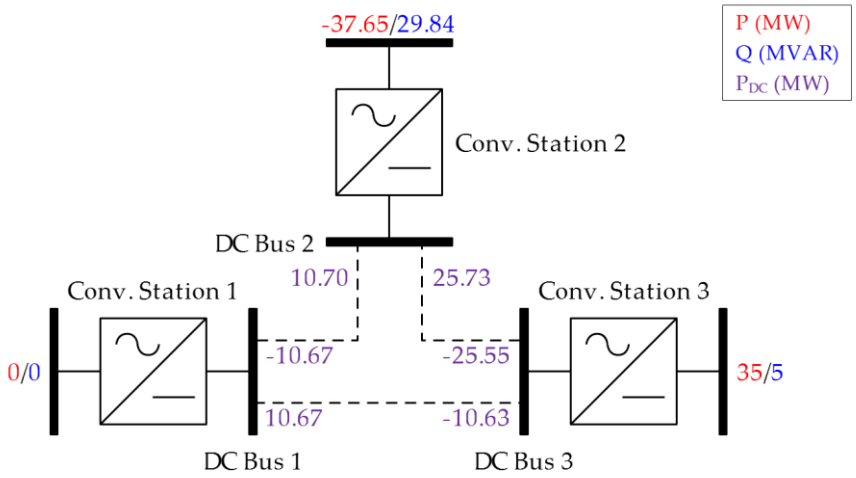


**Figure 4.5.** The AC/DC PF solution of the MT-HVDC system in Case 3

### *4.3.4. Case 4: AC/DC Power Flow Considering Droop Control Strategy*

As stated in Section 1.2.3.2, the droop control strategy is an efficient way of controlling MT-HVDC systems that can improve the PF of the AC and DC grids after an outage. In the fourth case, it is assumed that all converter stations in the studied system are equipped with the droop controllers. Table 4.13 illustrates the detailed information of the droop settings for each converter station. Figures 4.6 and 4.7 show the results of PF

calculations both in all AC and DC buses and branches in case of the outage of converter station #1 and considering droop control settings provided in table 4.13.

**Table 4.13.** Droop control settings for each converter station

| Converter Station | Droop Parameter | $P^*_{DC}$ $(MW)$ | $V^*_{DC}$ $(p.u.)$ |
|---|---|---|---|
| 1 | 0.005 | -58.6274 | 1.0079 |
| 2 | 0.007 | 21.9013 | 1.0000 |
| 3 | 0.005 | 36.1856 | 0.9778 |

* $P^*_{DC}$ and $V^*_{DC}$ are the reference power and reference DC voltage, respectively.

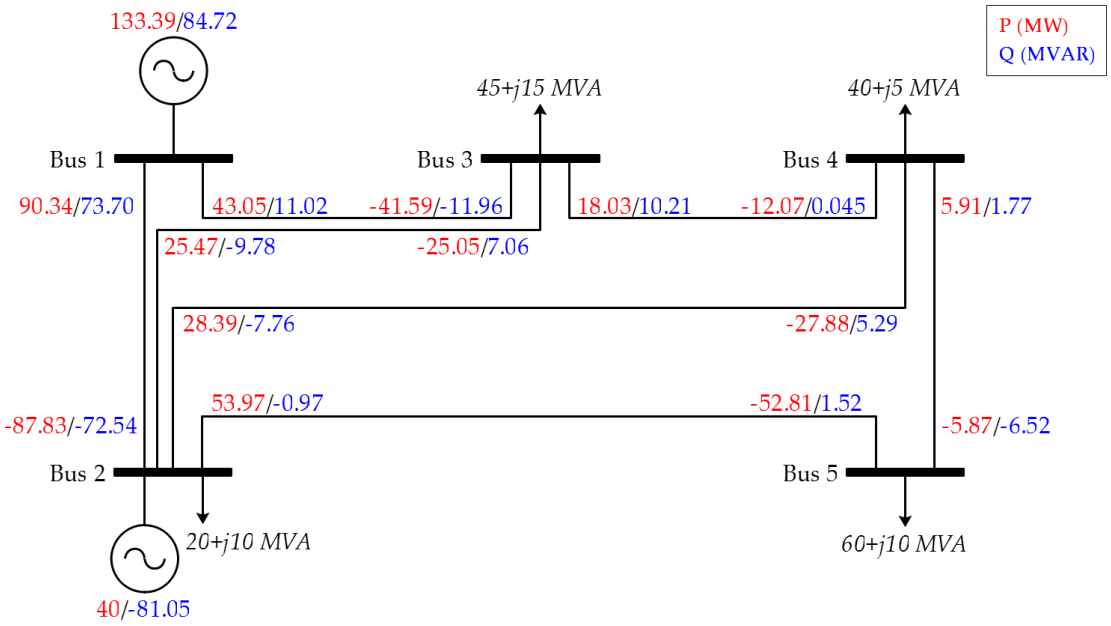


**Figure 4.6.** The AC grid PF solution in Case 4

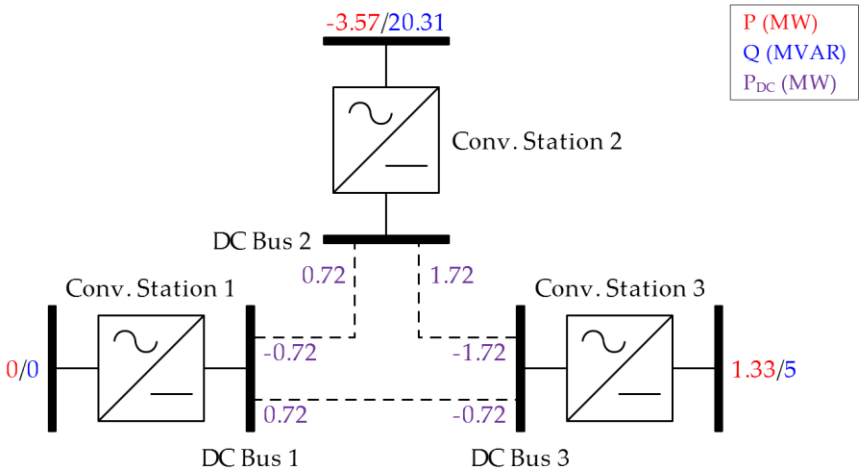


**Figure 4.7.** The AC/DC PF solution of the MT-HVDC system in Case 4

### *4.3.5. Case 5: AC/DC Power Flow Considering Changes of Droop Parameters*

In the fifth case, to demonstrate the impact of changes in the droop parameters of each converter station, the same test as Case 4 is evaluated by changing the droop parameters as shown in table 4.14. Figures 4.8 and 4.9 depict the results of PF calculations both in all AC and DC buses and branches in case of the outage of converter station #1 and considering the changes in droop parameters according to table 4.14.

**Table 4.14.** Changes in the droop parameters of each converter station

| Converter Station | Droop Parameter |
|---|---|
| 1 | 0.0010 |
| 2 | 0.0014 |
| 3 | 0.0010 |

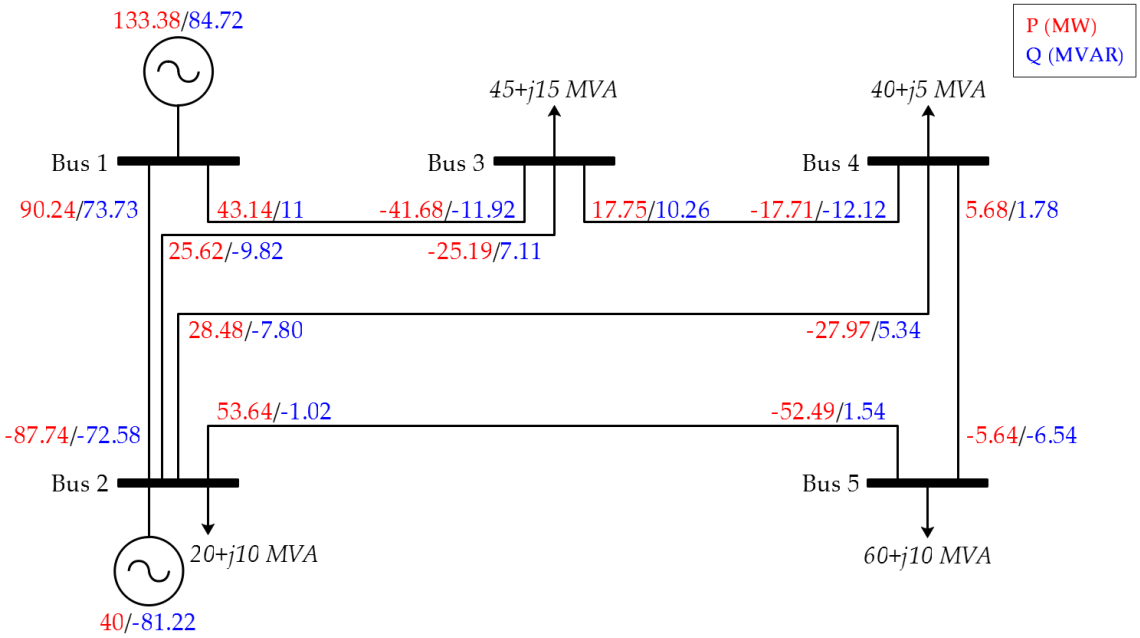


**Figure 4.8.** The AC grid PF solution in Case 5

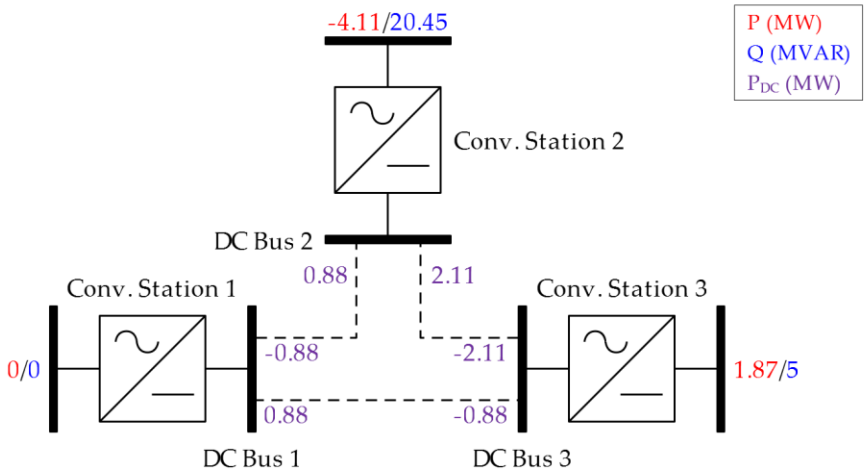


**Figure 4.9.** The AC/DC PF solution of the MT-HVDC system in Case 5

### *4.3.6. Case 6: AC/DC Power Flow Considering Converter Station Limits*

In the sixth case, the impact of the converter station limits on the AC/DC PF solution is investigated. When an active power set-point of a converter station equipped with the *P* controller is outside of the P-Q capability chart[1], the active power order should be reduced to comply with the predefined limit. Similarly, when a reactive power set-point

[1] P-Q capability chart shows the possible operation points.

of a converter station equipped with the $Q$ controller is outside of the P-Q capability chart, the reactive power order should be reduced to comply with the predefined limit, subject to not reaching the active power limit. Also, when a converter station equipped with the $V_{DC}$-droop controller reaches its limit, the converter station should be set to a constant $P$ injection equal to the maximum active power limit of the converter station. In addition, when a converter station equipped with the $V$-droop controller reaches its limit, the converter station should be set to a constant $Q$ injection based on the predefined limit. For both converter stations equipped with the $Q$ controller and $V_{DC}$-droop controller, the priority is given to active power over reactive power, when enforcing the limits. It should be noted that however, all the DC-slack buses are disregarded from the analysis, they are rechecked at the end of AC/DC PF calculations.

According to the above explanations, it is assumed that the converter station #1 reaches the reactive power limit and the converter station control is changed from constant $V$-mode to constant $Q$-mode. Figures 4.10 and 4.11 illustrate the results of PF calculations both in all AC and DC buses and branches after enforcing the converter station current and voltage limits.

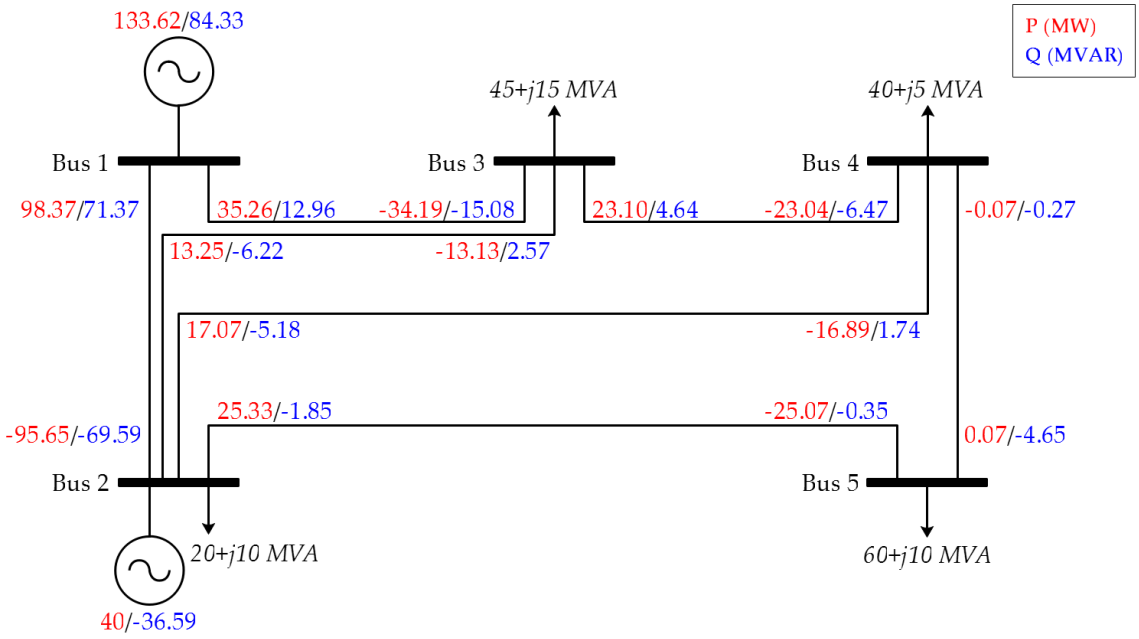


**Figure 4.10.** The AC grid PF solution in Case 6

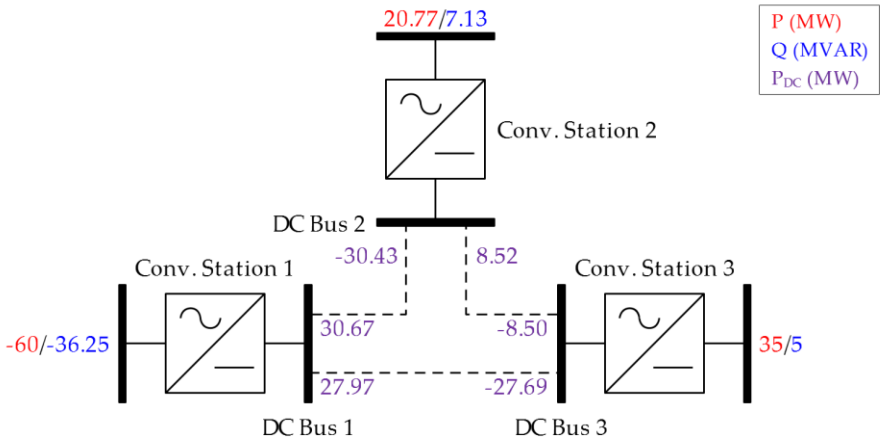


**Figure 4.11.** The AC/DC PF solution of the MT-HVDC system in Case 6

To demonstrate the impact of changing the set-point of the converter station, the active power set-point of the converter station #1 is set to -130 MW so that simultaneously both active and reactive power violate their limits. Figures 4.12 and 4.13 show the results of PF calculations both in all AC and DC buses and branches after changing the active power set-point of the converter station #1 to -130 MW.

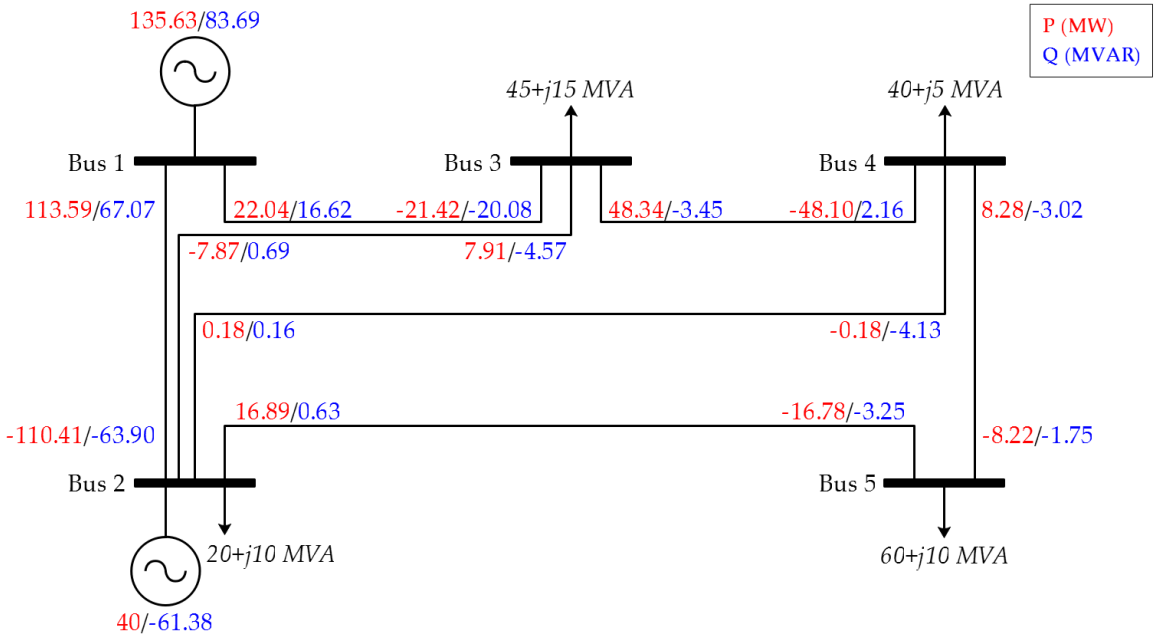


**Figure 4.12.** The AC grid PF solution in Case 6 after changing the set-point of converter station #1

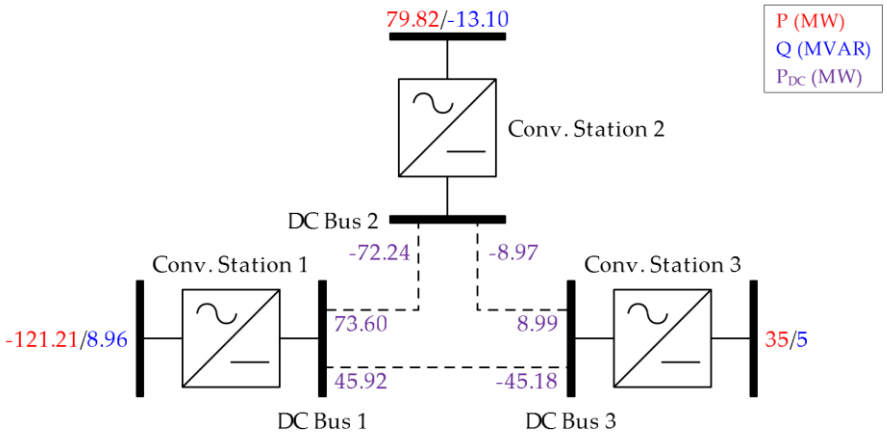


**Figure 4.13.** The AC/DC PF solution of the MT-HVDC system in Case 6 after changing the set-point of converter station #1

### *4.4. Summary*

In this chapter, a mixed AC/DC Power Flow (PF) algorithm for the steady-state interaction of the large-scale MT-HVDC systems is investigated. This algorithm is an improved sequential AC/DC PF algorithm, which uses the Newton-Raphson method to solve the DC PF problem. Different operational constraints and control strategies along with contingency analysis in hybrid AC/DC grids are considered in this study. Fast convergence and high accuracy are the main advantages of the mixed AC/DC PF algorithm. Also, it is a powerful tool for sensitivity analysis and congestion management in power systems. Various cases are studied in this chapter to evaluate the performance of the mixed AC/DC PF algorithm. The obtained results demonstrate the robustness and effectiveness of the mixed AC/DC PF algorithm for power system operation and planning studies.

CHAPTER 5

# *A New Topology of a Fast Proactive Hybrid DC Circuit Breaker for MT-HVDC Grids*

## *5.1. Configuration and Operation of the Proposed Hybrid DC Circuit Breaker*

### *5.1.1. Configuration of the Proposed Hybrid DC Circuit Breaker*

Figure 5.1 illustrates the overall structure of the proposed HDCCB with bidirectional current interruption capability. This structure consists of two main DC CBs in the main branch, a fast mechanical switch and an auxiliary DC CB in the auxiliary branch, and a residual DC current disconnector. The residual DC current disconnector (in series with a current limiting reactor) is used to entirely isolate the DC circuit.

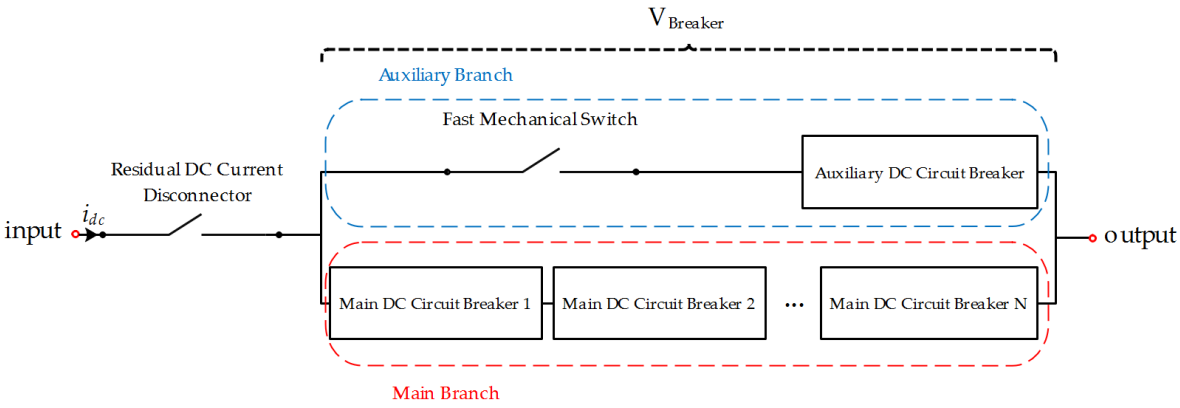


**Figure 5.1.** Overall structure of the proposed HDCCB

Figure 5.2 demonstrates the proposed configuration of the main DC CBs in the main branch. In this configuration, four submodules are considered to be connected back-to-back to isolate the DC current fault. Each submodule includes a diode, $D$, and a low resistance switch, $S$, in series and a capacitor, $C$, in parallel with the diode and switch. The switches are capable of breaking the bidirectional fault current. Also, the polarity of the capacitor changes with respect to the direction of the fault current. In order to protect the back-to-back submodules and prevent the capacitors from overvoltage, a Metal Oxide Varistor, $MOV$, is used.

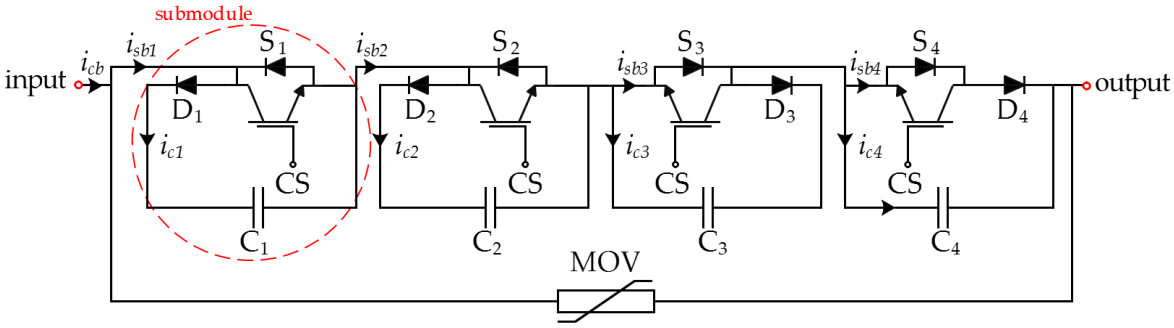


**Figure 5.2.** Configuration of the main DC CBs in the main branch

The auxiliary DC CB consists of two switches, as shown in figure 5.3. This CB matches lower voltage and current capability.

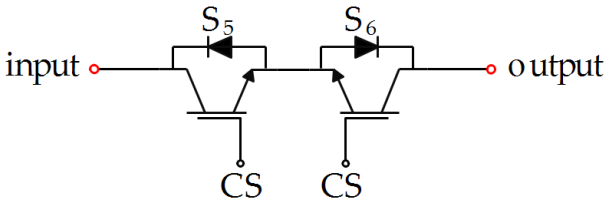


**Figure 5.3.** Configuration of the auxiliary DC CB

### *5.1.2. Principle and Operation of the Proposed Hybrid DC Circuit Breaker*

Predefined states of each component in the submodule determine the operation modes of the proposed HDCCB. Considering the operation modes, the switches can be either turned on or off. During the normal operation, the DC current flows through the auxiliary branch. In case of the DC fault, the auxiliary DC CB commutes the current to the main branch, and the fast mechanical switch opens. During the current breaking, the fast mechanical switch isolates the auxiliary DC CB from the voltage across the main DC CB. As a result, the rating voltage of the auxiliary DC CB reduces. Therefore, the majority of the power losses would be related to the switching losses. The fast mechanical switch opens when zero current and/or low voltage stress can be detected. The recovery voltage of the fast mechanical switch determines by the proactive level of the surge arresters, while both the main and auxiliary DC CBs are open. By connecting several mechanical switches, the operation time exceeds 30 ms. Proper control of the HDCCB leads to minimizing the time delay of the mechanical switching elements. Hence, the operation time of the multiple switches should be less than the time for selective protection. Figure 5.4 depicts the typical proactive control of the HDCCB. The proactive control system enables when the level of

the DC line current exceeds the predefined overcurrent level. In this case, two events are expected: (1) The selective protection sends a trip signal. (2) The DC current of the faulty line reaches the maximum breaking current capability of the main DC CB. In both cases, there would be a time delay for the current breaking of the main DC CB.

To extend the operation time until the main DC CB sends the trip signal, the main DC CB may disconnect the line in the current limitation mode prior to the current breaking. To prevent sudden increases in the line current, the voltage drop across the DC reactor should be controlled by the main DC CB. The energy dissipation capability of the surge arrester determines the maximum operation time of the current limiting mode. Also, to allow maintenance on demand while not interrupting the power transfer in the DC grids, scheduled current transfer of the line current from the auxiliary DC CB to the main DC CB is required. Considering the proactive mode, overcurrent in the DC grid can activate the current transfer from the auxiliary branch into the main branch of the DC CB prior to the trip signal of the protection device. Considering the CB failure, the backup CB activates within less than 0.2 ms to avoid large disturbances in the DC grids and maintain the breaking current capability of the backup CB at the reasonable levels. After clearing the fault, the HDCCB returns to its normal operation mode.

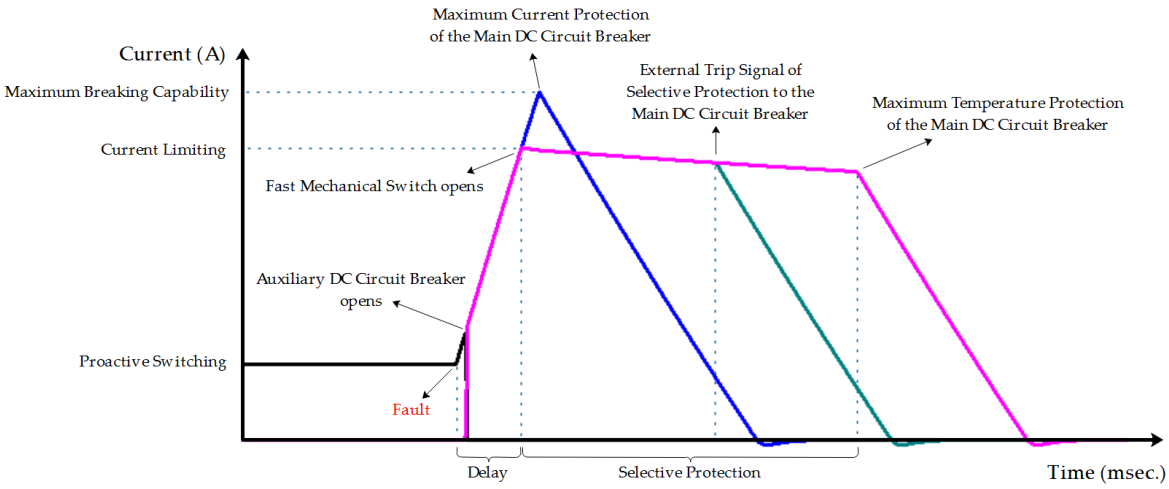


**Figure 5.4.** The current waveform of a typical proactive HDCCB

According to figure 5.2, when the DC CB, which is located at the power receiving, is closed, the power flows from the output of the DC CB, based on the unidirectional conduction ability of the diode that is paralleled with the IGBT in the submodule. When

the DC CB, which is placed at the power sending end, is closed, the power flows from the input of the DC CB with the conduction of the IGBT in the submodule. Under the normal operation, the IGBT in the submodule is conducted and cascaded into the circuit. In case of DC fault, the IGBT of the submodule is shut down to prevent the diode and capacitor from being cascaded into the fault loop. By charging the capacitor, the back Electromotive Force (EMF) forces both ends of the equivalent capacitor on the short-circuit path to surpass the peak line voltage on the AC side to block the fault current. The fault tolerance capability can be significantly improved as the diode in the submodule, and the arm inductance in the AC/DC converter station in the DC fault are both shock resistance. This structure limits the rate of rise of the voltage across the DC CB, reduces the on-state switching losses, and guarantees an equal voltage distribution regardless of tolerances in the switching characteristics. Table 5.1 shows the operation status of the components in each submodule.

**Table 5.1.** The operation status of the components in each submodule

| Operation Mode | Diode | IGBT | Capacitor |
|---|---|---|---|
| Mode 1: Power Receiving End | Bypass | No Action | Bypass |
| Mode 2: Power Sending End | Bypass | Conducted | Bypass |
| Mode 3: Shut Down | Accessing to the Circuit | Shut Down | Charging |

### *5.2. Design Parameters in the Proposed Hybrid DC Circuit Breaker*

The designed parameters of the proposed HDCCB should be properly determined successfully to interrupt the fault current. Figure 5.5 illustrates the equivalent circuit of the DC CB in the DC grid in case of a short-circuit fault. As shown in this figure, the AC/DC converter station can be modeled as a DC voltage source, $U_{DC}$, and the line reactor in the DC grid is replaced by $L_{DC}$ [136].

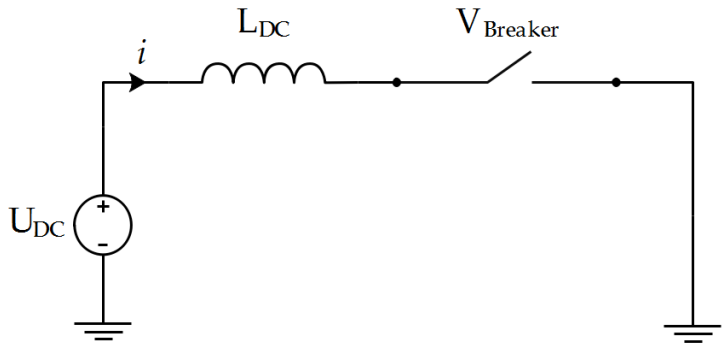


**Figure 5.5.** Equivalent circuit of the DC CB in the DC grid

After the DC fault occurrence, the induced voltage, $V_L$, is generated by the inductor of the DC grid. Considering that the inter-terminal voltage of the DC CB is $V_{Breaker}$, then:

$$U_{DC} = V_L + V_{Breaker} = L_{DC}\frac{di}{dt} \tag{5-1}$$

By establishing the transient state of the voltage of the DC CB, $V_L$ reverses, and $V_{Breaker}$ limits by the voltage of MOV, $V_{MOV}$. Therefore:

$$U_{DC} = V_L + V_{Breaker} = L_{DC}\frac{di}{dt} + V_{MOV} \tag{5-2}$$

According to Equations (5-1) and (5-2), the fault current can be derived as follows:

$$i = \begin{cases} \dfrac{U_{DC}}{L_{DC}}.t \\ \dfrac{U_{DC} - V_{MOV}}{L_{DC}}.t \end{cases} \tag{5-3}$$

Hence, the rate of rise of fault current can be calculated as follows:

$$\frac{di}{dt} = \begin{cases} \dfrac{U_{DC}}{L_{DC}} \\ \dfrac{U_{DC} - V_{MOV}}{L_{DC}} \end{cases} \tag{5-4}$$

Considering the time of the fault, $t_{fault}$, the maximum breaking current capability of the DC CB is as follows:

$$i_{(max)} = \frac{di}{dt}.t_{fault} = \frac{U_{DC}}{L_{DC}}.t_{fault} \tag{5-5}$$

In addition, the maximum rate of rise of fault current can be derived as follows:

$$\frac{di}{dt_{(max)}} = \frac{U_{DC}}{L_{DC}} \tag{5-6}$$

The energy dissipation capability of the HDCCB is from the DC power source and the stored energy in the line reactor. The energy dissipation from the DC power supply can be written as follows:

$$E_{source} = \int U_{DC}.idt = \int U_{DC}.\frac{U_{DC} - V_{MOV}}{L_{DC}}.tdt \tag{5-7}$$

In addition, the energy dissipation from the line reactor can be written as follows:

$$E_{reactor} = \frac{1}{2}L_{DC}(i_{(max)})^2 \tag{5-8}$$

The summation of the energy dissipation from the DC power source and the line reactor gives the total energy dissipation of the HDCCB.

$$E_{MOV} = \frac{1}{2}.\frac{U_{DC}V_{MOV}}{U_{MOV} - V_{DC}}.(\frac{1}{\frac{di}{dt_{(max)}}}.i_{(max)})^2 \tag{5-9}$$

### *5.3. Results and Discussions*

#### *5.3.1. Simulation Results*

In order to check the performance of the proposed HDCCB, a DC-link representing a DC-pole of the VSC-HVDC system is modeled on PSCAD/EMTDC environment, as shown in figure 5.6. An HDCCB is located at the end of the DC-link. As one of the most common faults in the VSC-HVDC systems, a single line-to-ground fault on the DC-link is selected for the fault mechanism analysis. It is assumed that the output voltage of the VSC-

HVDC converter station, $U_{DC}$, is constant. Tables 5.2 and 5.3 show the main parameters of the DC-link and the specifications of the proposed HDCCB, respectively.

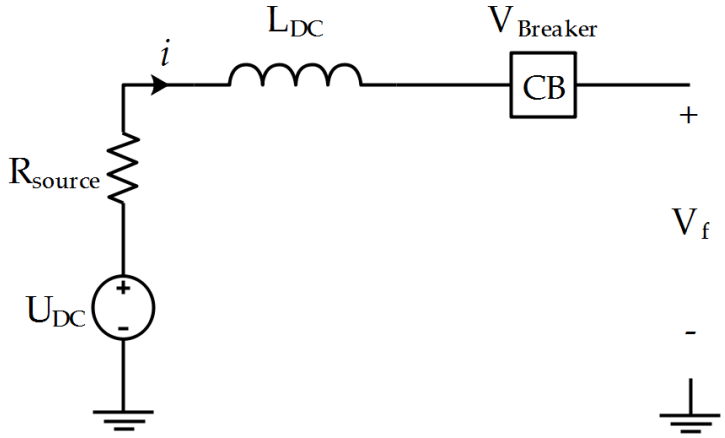


**Figure 5.6.** Configuration of the DC-link for fault analysis

**Table 5.2.** DC-link parameters

| Parameter | Value |
|---|---|
| $U_{DC}$ | 320 kV |
| $R_{source}$ | 0.001 Ω |
| $L_{DC}$ | 100 mH |

**Table 5.3.** Specifications of the proposed HDCCB

| Parameter | Value |
|---|---|
| Capacitor ($C$) | 6.8 μF |
| Time delay of residual disconnector | 20 ms |
| Time delay of fast mechanical switch | 2 ms |
| Forward Breakover Voltage (IGBT) | 100 kV |
| Forward Breakover Voltage (Diode) | 100 kV |

#### *5.3.1.1. Rated Current Interruption*

To give a general perspective about the relation of the designed parameters, considering 2 ms as the breaking time, and the fact that DC line fault is close to the DC switchyard, the maximum rate of rise of fault current is 3.5 kA/ms for a DC reactor of 100 mH in a 320 kV DC power grid with 10% maximum overvoltage. If the rated line current is 2 kA, the minimum required current breaking current capability of the HDCCB should be 9 kA. When there is no fault in the DC grid, the voltage drop across the DC CB is 0.04 V, and the total current passing through the DC grid is 1.6 kA. Figure 5.7 shows the

behavior of the DC line current, and the current passing through the capacitors and switches of the HDCCB after applying a short-circuit DC fault at 5 s. As shown in figure 5.7, the breaking time is less than 2.5 ms. The maximum current passing through the capacitors and switches of the HDCCB is 2.3157 kA and 8.0713 kA, respectively. The auxiliary CB opens into 50 µs. At 5.00195 s., the fast mechanical switch opens, where the corresponding value of the current limiting is 8.0713 kA. According to figure 5.7, the maximum value of the DC fault current is 8.4425 kV, which is less than the minimum required breaking current capability of the HDCCB and the fault is successfully cleared within 16 ms. Based on the provided results, the maximum breaking current capability of 9 kA is confirmed. It should be noted that in figure 5.7, the DC current passing through the line and the DC current of the proposed HDCCB are the same.

As there are some limitations in terms of breaking current capabilities of the IGBTs, by rising the current, voltage drop across the IGBTs increases significantly. To overcome this issue, the press-back IGBTs are used to ensure a reliable short-circuit without mechanical damage and failure of the IGBTs' modules. Therefore, in case of the failure of one of the IGBT modules, the fault can be cleared by the rest of IGBTs.

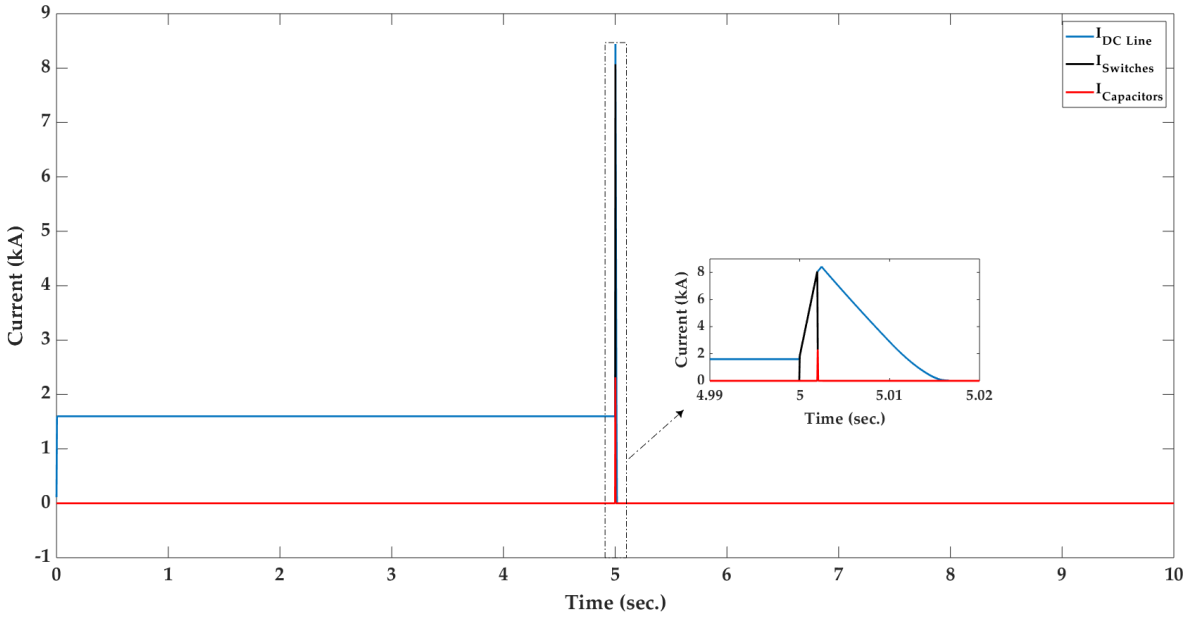


**Figure 5.7.** The DC line current, and the current passing through the capacitors and switches of the proposed HDCCB after applying a short-circuit DC fault at 5 s

Figure 5.8 illustrates the CB voltage and voltage at the fault location ($V_{Fault}$) after applying a short-circuit DC fault at 5 s. As shown in figure 5.8, the voltage across the proposed HDCCB exceeds approximately 180 kV during the current commutation, and the proposed HDCCB successfully clears the fault within 16 ms.

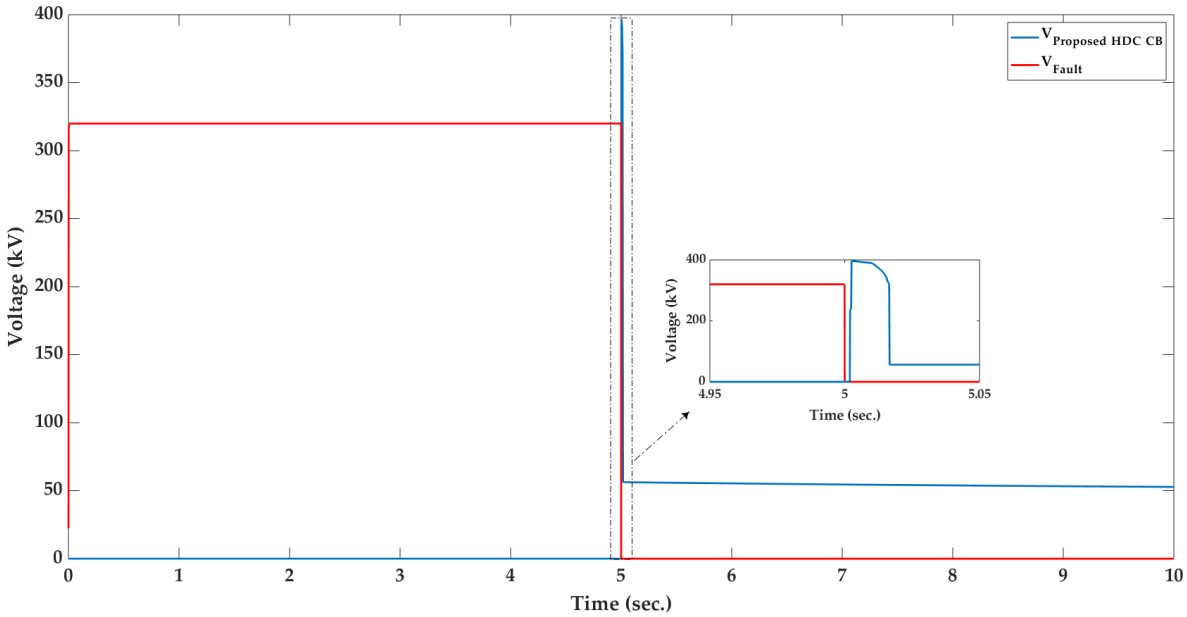


**Figure 5.8.** The CB voltage and voltage at the fault location after applying a short-circuit DC fault at 5 s

By increasing the capacity of the capacitors of the main DC CBs, the maximum breaking current capability of the HDCCB increases. However, due to the discharge time of the capacitors, it takes longer time to entirely clear the DC fault.

Figure 5.9 demonstrates the dissipated energy of the surge arrestors in the two main DC CBs of the proposed HDCCB. The maximum dissipated energy of the surge arrestors in the main DC CB 1 and 2 is 12.6209 kJ and 7.7952 kJ, respectively.

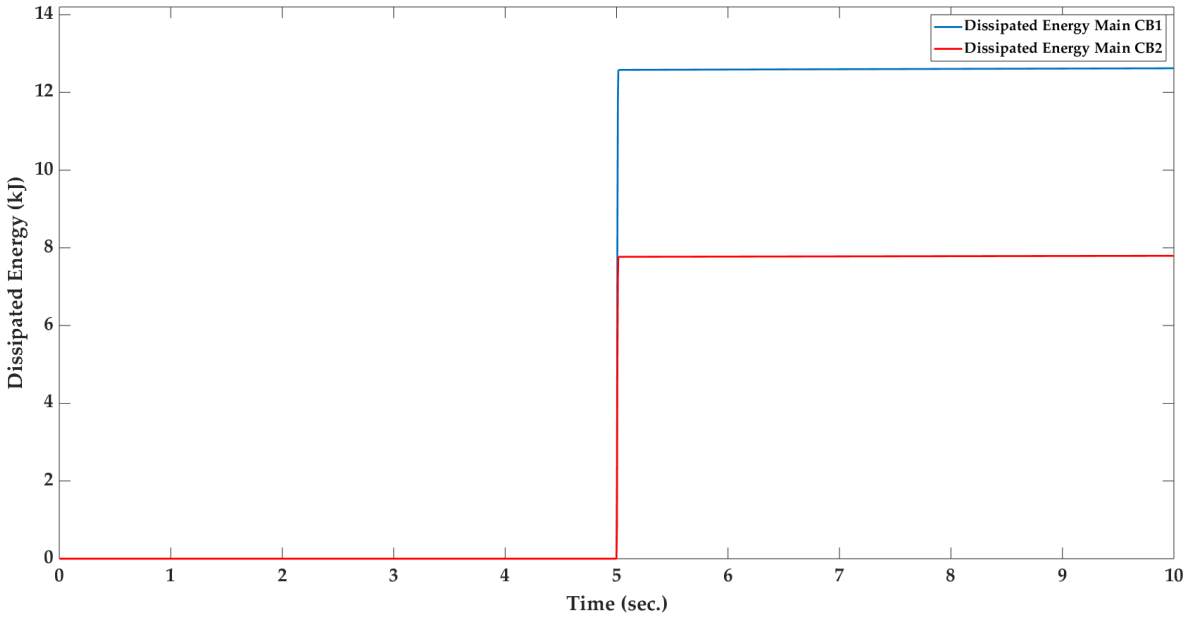


**Figure 5.9.** The dissipated energy of the surge arrestors in the two main DC CBs of the proposed HDCCB after applying a short-circuit DC fault at 5 s

#### *5.3.1.2. Reverse Current Interruption*

In order to demonstrate the reverse current interruption of the proposed HDCCB, the direction of designed CB is reversed, so that the fault current flows in the opposite direction. Figure 5.10 shows that the same as the rated current interruption, the maximum breaking current capability of -9 kA is confirmed.

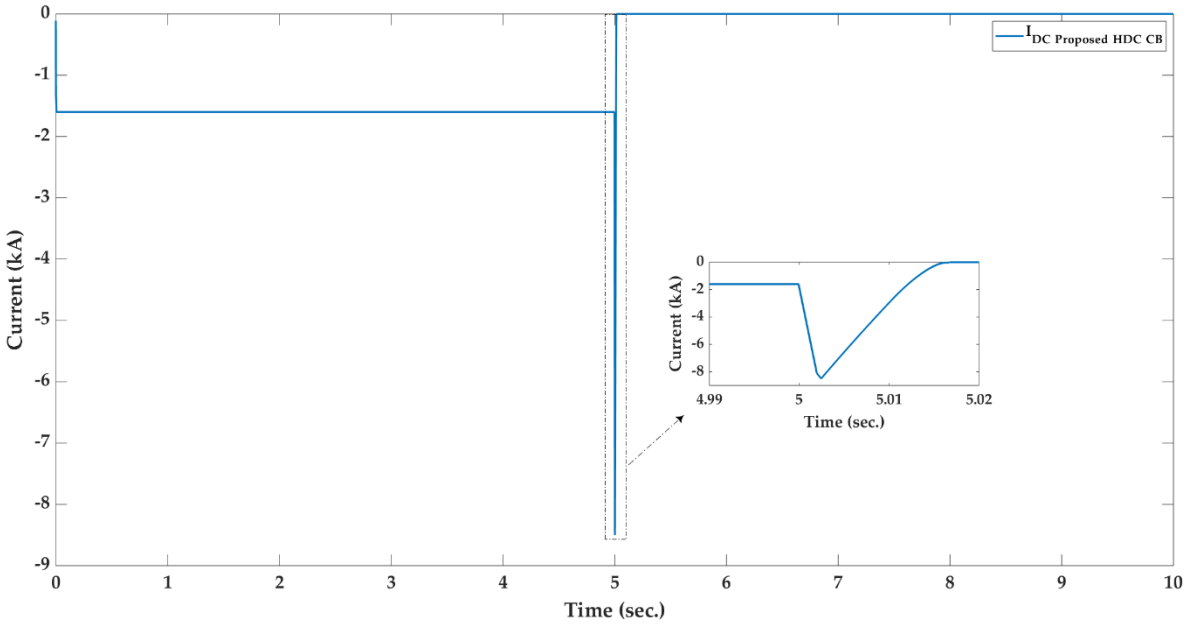


**Figure 5.10.** The DC current of the proposed HDCCB after applying a short-circuit DC fault at 5 s after changing the direction of the proposed HDCCB

Figure 5.11 illustrates the CB voltage and voltage at the fault location after applying a short-circuit DC fault at 5 s after changing the direction of the proposed HDCCB. As shown in figure 5.11, the proposed HDCCB successfully clears the fault within 16 ms.

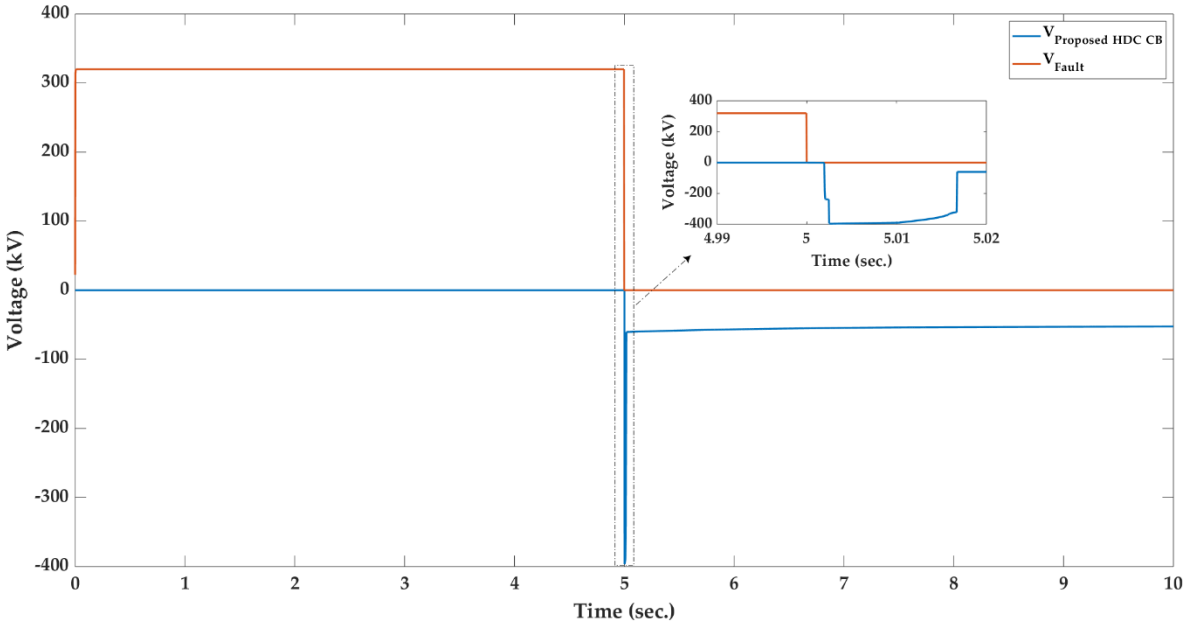


**Figure 5.11.** The CB voltage and voltage at the fault location after applying a short-circuit DC fault at 5 s after changing the direction of the proposed HDCCB

### *5.3.1.3. Reclosing and Rebreaking Capabilities*

To evaluate reclosing and rebreaking capabilities of the proposed HDCCB, a short time (dead time) between the first trip signal and the closing signal is considered. During this period of the time, there is no response from the proposed HDCCB to the test system. After the first trip signal, the proposed HDCCB opens and performs the first current interruption. The reclosing signal is sent to the proposed HDCCB 50 ms after the first trip, and the proposed HDCCB attempts to reconnect the source to the line. As the fault is not cleared from the system, the fault current rises as soon as the CB is closed. The second trip signal is sent to the proposed HDCCB 50 ms after the CB is closed, and then the proposed HDCCB performs the second current interruption. After that, the proposed HDCCB remains open to insulate the DC fault. Figures 5.12, 5.13, 5.14, and 5.15 show reclosing and rebreaking capabilities of the proposed HDCCB in both the rated and reverse current interruptions. The simulation results validate the reclosing and rebreaking capabilities of the proposed HDCCB in both the rated and reverse current interruptions.

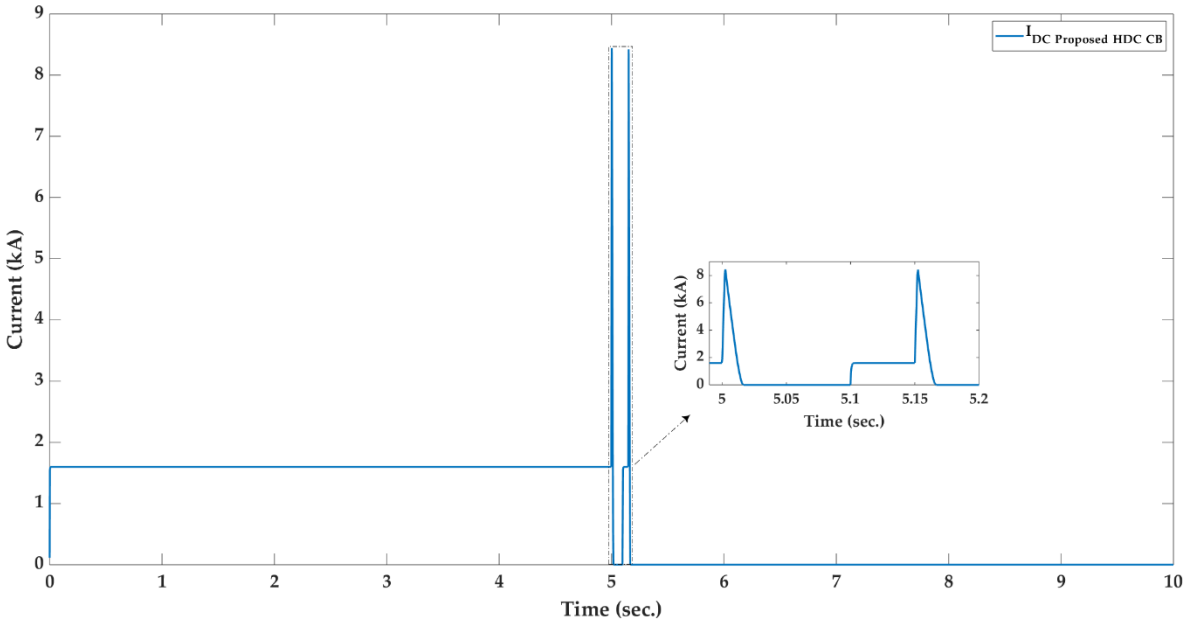


**Figure 5.12.** The DC current of the proposed HDCCB in reclosing and rebreaking test in the rated current interruption

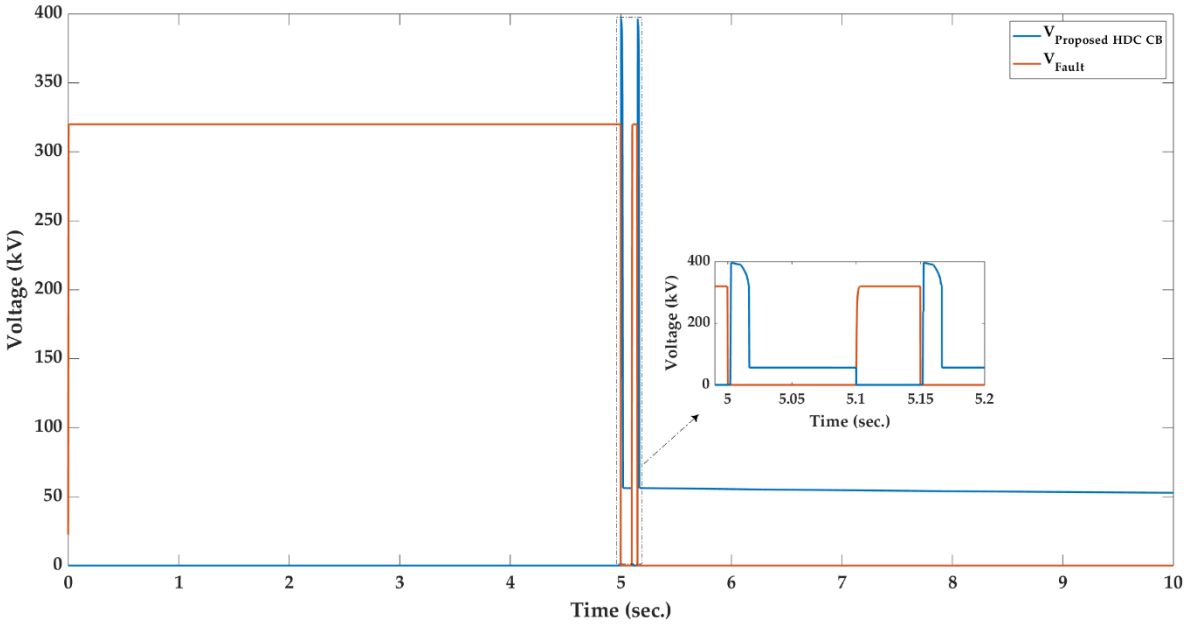


**Figure 5.13.** The CB voltage and voltage at the fault location in reclosing and rebreaking test in the rated current interruption

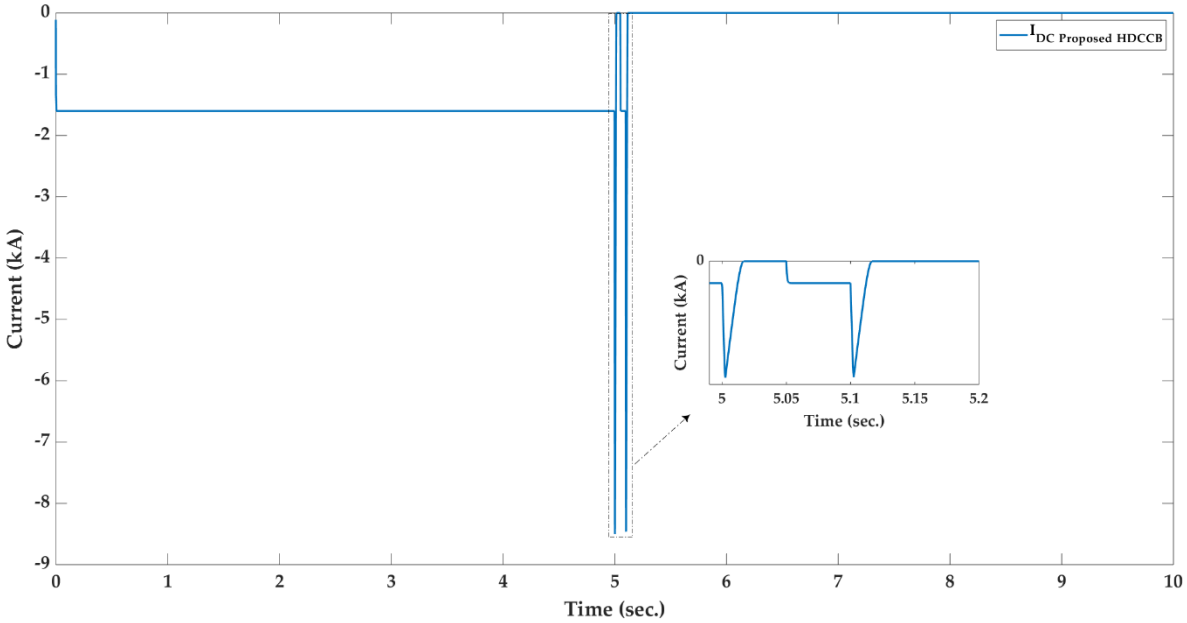


**Figure 5.14.** The DC current of the proposed HDCCB in reclosing and rebreaking tests in the reverse current interruption

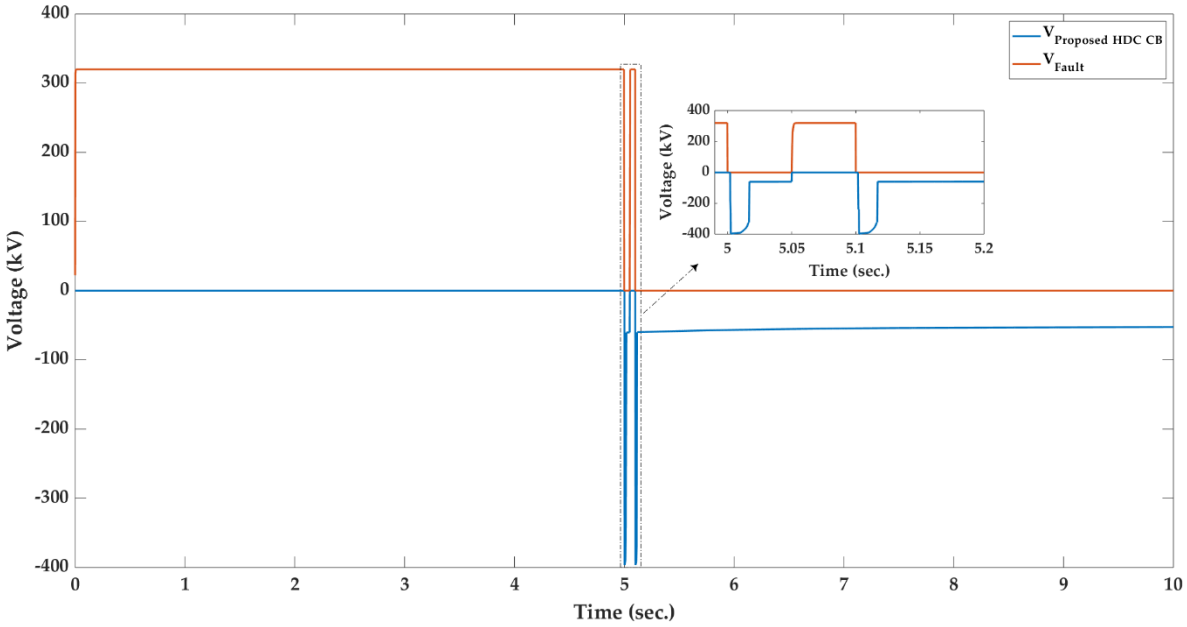


**Figure 5.15.** The CB voltage and voltage at the fault location in reclosing and rebreaking test in the reverse current interruption

### *5.3.2. Comparison*

To evaluate and compare the performance of the proposed HDCCB over the conventional DC CB in [176, 182-183], replication is done, and proper matching is noticed in all cases. Figure 5.16 illustrates a comparison between the CB voltage responses of the proposed HDCCB and the conventional DC CB. As shown in figure 5.16, the voltage response of the proposed HDCCB tracks the voltage of the conventional DC CB. However, due to the fact that the DC capacitors have some charges, the level of DC voltage of the proposed HDCCB after the fault is more than the level of voltage of the conventional DC CB.

Figure 5.17 demonstrates the comparison between the DC current response of the proposed HDCCB and the conventional DC CB after applying a short-circuit DC fault at 5 s. As shown in figure 5.17, good matching is observed. The maximum breaking current capability of the proposed HDCCB and conventional DC CB are 8.4425 kA and 8.4207 kA, respectively. Thus, the difference between the maximum breaking current capability of the proposed HDCCB and conventional DC CB is 21.8 A.

The maximum dissipated energy of the surge arrestor in the DC CB 1 of the conventional DC CB is 12.6388 kJ, which is 17.9 J more than the corresponding value of the proposed HDCCB. However, because of the capacitor charge, the dissipated energy of the surge arrestor in the DC CB 2 of the conventional DC CB is 7.7952 kJ which is 16.1 J less than the corresponding value of the proposed HDCCB. But, the total dissipated energy of the surge arrestor of the proposed HDCCB and the conventional DC CB are approximately the same.

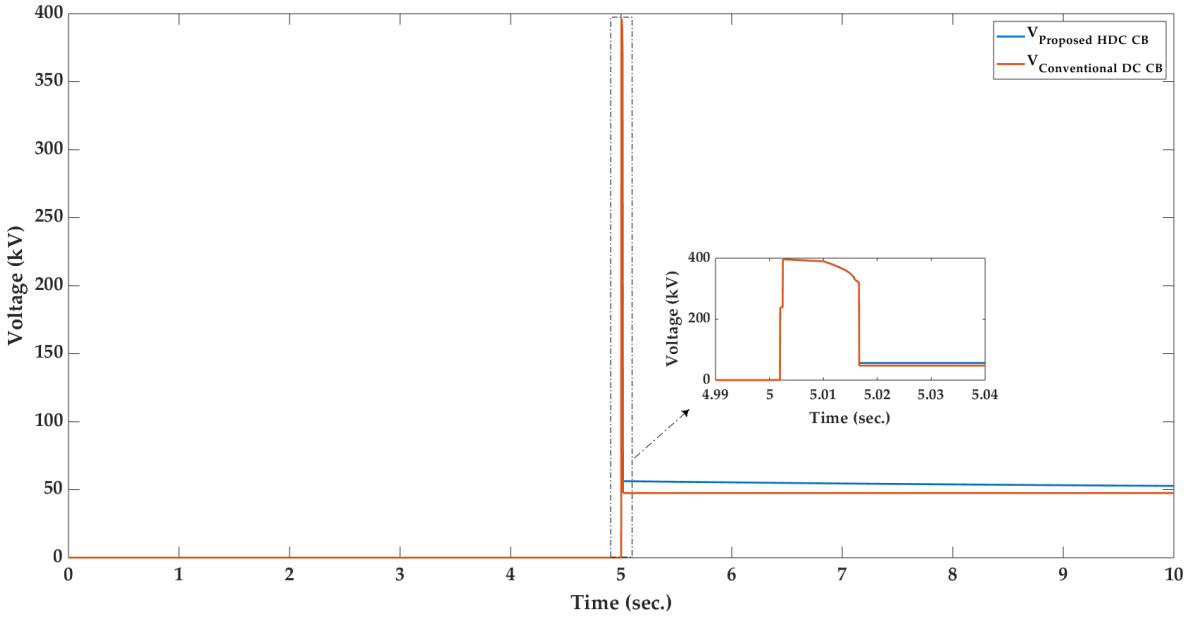


**Figure 5.16.** Comparison between the voltage response of the proposed HDCCB and the conventional DC CB after applying a short-circuit DC fault at 5 *s*

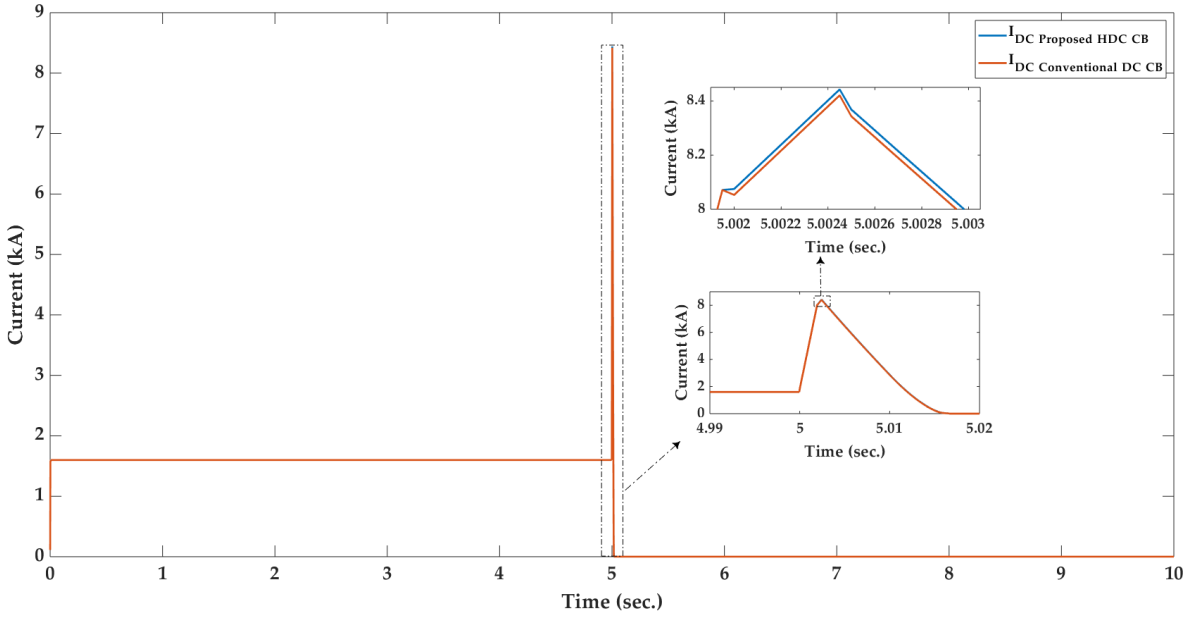


**Figure 5.17.** Comparison between the DC current response of the proposed HDCCB and the conventional DC CB after applying a short-circuit DC fault at 5 s

### *5.4. Summary*

This chapter presents a new topology of a fast proactive Hybrid DC Breaker (HDCCB) to isolate the DC faults in Multi-Terminal VSC-HVDC (MT-HVDC) grids in case of fault current interruption, along with lowering the conduction losses and lowering the interruption time. All modes of operation of the proposed topology are studied. Simulation results verify that compared to the conventional DC CB, the proposed topology has lower interruption time, lower on-state switching losses, and higher breaking current capability. Due to the fact that MT-HVDC systems can share the power among the converter stations independently and in both directions, and considering the fast bidirectional fault current interruption, and reclosing and rebreaking capabilities, the proposed HDCCB can improve the overall performance of MT-HVDC systems and increase the reliability of the DC grids.

# CHAPTER 6

## *Conclusions and Future Works*

### *6.1. Conclusions*

The main aim of this study is to solve four major challenges in hybrid AC/DC grids which are: (1) the integration of high-voltage charging stations as DG resources in power systems and their contributions to the grid regulation, (2) control the VSC-HVDC stations in MT-HVDC system in such a way to regulate the AC voltage, DC voltage, and frequency, (3) investigate the AC/DC power flow solution, and (4) the protection of MT-HVDC systems. Followings show the details of each chapter in this thesis.

In chapter 2, the impact of PHEVs charging on the power grid is shown. A bidirectional charging station with a novel control strategy is proposed to solve the problem of voltage and frequency regulation in the power system due to the charging of PHEVs. A central AC/DC VSC converter station is investigated to inject active and reactive power into the power grid to regulate the voltage and frequency and reduce the peak load, as well as power quality improvement by considering the SoC and available active power in power grids. The proposed control strategy allows PHEVs to contribute to the grid regulation when an event occurs in a DG-based power grid consisting of different microgrids, diesel generator and wind farm, PHEVs with several charging profiles, and different loads.

In chapter 3, an improved droop-based control strategy for the active and reactive power-sharing on the large-scale MT-HVDC systems is proposed. The equivalent circuit of the VSC-HVDC station in the $dq$ reference frame is established and employed for developing an improved droop-based control strategy for the VSC-HVDC station. The proposed improved droop-based control strategy is a communication-free control method which its droop parameters, consisting of AC voltage-droop, DC voltage-droop, and frequency-droop parameters, are selected optimally. The proposed improved droop-based control strategy is applied to a five-terminal MT-HVDC system to control both the AC and DC grids for a stable-steady state and dynamic performance. In addition, different control

strategies of the VSC-HVDC station is investigated in this chapter. Modifications on the droop settings are also performed. The simulation results illustrate that the proposed improved droop-based control strategy not only results in a stable steady stated and dynamic operation of the MT-HVDC system but also is capable of restoring operation during the loss of DC voltage regulating VSC-HVDC station without the need for communication infrastructure.

In chapter 4, a mixed AC/DC PF algorithm for the steady-state interaction of the large-scale MT-HVDC systems is investigated. This algorithm is an improved sequential AC/DC PF algorithm, which uses the Newton-Raphson method to solve the DC PF problem. Different operational constraints and control strategies along with contingency analysis in hybrid AC/DC grids are considered in this study. Fast convergence and high accuracy are the main advantages of the mixed AC/DC PF algorithm. In addition, it is a powerful tool for sensitivity analysis and congestion management in power systems. Various cases are studied in this chapter to evaluate the performance of the mixed AC/DC PF algorithm.

In chapter 5, a new topology of a fast proactive HDCCB to isolate the DC faults in MT-HVDC systems in case of fault current interruption, along with lowering the conduction losses and lowering the interruption time is presented. All modes of operation of the proposed topology are studied. Simulation results verify that compared to the conventional DC CB, the proposed topology has lower interruption time, lower on-state switching losses, and higher breaking current capability. Due to the fact that MT-HVDC systems can share the power among the converter stations independently and in both directions, and considering the fast bidirectional fault current interruption, and reclosing and rebreaking capabilities, the proposed HDCCB can improve the overall performance of MT-HVDC systems and increase the reliability of the DC grids.

### *6.2. Future Works*

Followings are some other ideas, which can be studied in the future.

- Sensitivity, power quality, and stability analyses in hybrid AC/DC grids considering the integration of high-voltage charging stations
- The impact of dynamic charging stations on the hybrid AC/DC grids
- Reliability analysis in hybrid AC/DC grids considering the integration of high-voltage charging stations
- Operational planning for MT-HVDC systems
- The stability analysis of the proposed droop-based controller
- Power quality analysis in MT-HVDC systems considering the proposed droop-based controller
- AC/DC optimal power flow in MT-HVDC systems
- Unit commitment and Economic dispatch in MT-HVDC systems
- Propose a new HDCCB to reduce the fault current interruption in MT-HVDC systems

# REFERENCES


1. Mohammadi, F. Design and Electrification of an Electric Vehicle Using Lithium-ion Batteries. In Proceedings of the 3rd International Conference on Electrical Engineering, Tehran, Iran, 7 September 2018.
2. Mohammadi, F. Electric Vehicle Battery Market Analysis: Lead Acid. In Proceedings of the 9th Iranian Conference on Electrical and Electronics Engineering (ICEEE), 28 August 2018.
3. Mohammadi, F. Electric Vehicle Battery Market Analysis: Nickel Metal Hydride. In Proceedings of the 9th Iranian Conference on Electrical and Electronics Engineering (ICEEE), 28 August 2018.
4. Mohammadi, F. Electric Vehicle Battery Market Analysis: Lithium-ion. In Proceedings of the 1st International Conference on Modern Approaches in Engineering Science (ICMAES), Tbilisi, Georgia, 21 November 2018.
5. Mohammadi, F. Analysis and Electrification of the Solar-Powered Electric Vehicle. In Proceedings of the 5th Iranian Conference and Exhibition on Solar Energy (ICESE), Tehran, Iran, 18 August 2018.
6. Mohammadi, F. Research in the Past, Present, and Future Solar Electric Aircraft. Journal of Solar Energy Research (JSER), Vol. 3(3), December 2018.
7. Mohammadi, F. Design, Analysis, and Electrification of a Solar-Powered Electric Vehicle. Journal of Solar Energy Research (JSER), Vol. 3(4), December 2018.
8. Mohammadi, F. Hybridization of an Electric Vehicle Using Lithium-ion Batteries. In Proceedings of the 1st International Conference on Modern Approaches in Engineering Science (ICMAES), Tbilisi, Georgia, 21 November 2018.
9. Bauer, P.; Zhou, Y.; Doppler, J.; Stembridge, N. Charging of Electric Vehicles and Impact on the Grid. In Proceedings of the 13th Mechatronika, Trencianske Teplice, Slovakia, 2-4 June 2010.
10. Dharmakeerthi, C.; Mithulananthan, H. N.; Saha, T. K. Modeling and Planning of EV Fast Charging Station in Power Grid. In Proceedings of the IEEE Power and Energy Society General Meeting, San Diego, CA, USA, 22-26 July 2012.

11. Ding, M.; Zhang, Y.; Mao, M. Key Technologies for Microgrids - A Review. In Proceedings of the International Conference on Sustainable Power Generation and Supply, Nanjing, China, 6-7 April 2009.
12. Pourbabak, H.; Kazemi, A. A New Technique for Islanding Detection Using Voltage Phase Angle of Inverter-Based DGs. International Journal of Electrical Power and Energy Systems, Vol. 57, May 2014.
13. Chen, D.; Xu, L. Autonomous DC Voltage Control of a DC Microgrid with Multiple Slack Terminals. IEEE Transactions on Power Systems, Vol. 27(4), November 2012.
14. Liu, X.; Wang, P.; Loh, P. C. A Hybrid AC/DC Micro-Grid. In Proceedings of the International Power Engineering Conference (IPEC), Singapore, 27-29 October 2010.
15. Wang, P.; Liu, X.; Jin, C.; Loh, P.; Choo, F. A Hybrid AC/DC Micro-Grid Architecture, Operation and Control. In Proceedings of the IEEE Power and Energy Society General Meeting, San Diego, CA, USA, 24-29 July 2011.
16. Kakigano, H.; Miura, Y.; Ise, T. Low-Voltage Bipolar Type DC Microgrid for Super High Quality Distribution. IEEE Transactions on Power Electronics, Vol. 25(12), Dec. 2010.
17. Mohammadi, F. Power Management Strategy in Multi-Terminal VSC-HVDC System. In Proceedings of the 4th National Conference on Applied Research in Electrical, Mechanical Computer and IT Engineering, Tehran, Iran, 4 October 2018.
18. Mohammadi, F.; Zheng, C. Stability Analysis of Electric Power System. In Proceedings of the 4th National Conference on Technology in Electrical and Computer Engineering, Tehran, Iran, 27 December 2018.
19. Xu, L.; Chen, D. Control and Operation of a DC Microgrid with Variable Generation and Energy Storage. IEEE Transactions on Power Delivery, Vol. 26(4), October 2011.
20. Liu, X.; Wang, P.; Loh, P. C.; A Hybrid AC/DC Microgrid and Its Coordination Control. IEEE Transactions on Smart Grid, Vol. 2(2), June 2011.
21. Nejabatkhah, F.; Li, Y. W. Overview of Power Management Strategies of Hybrid AC/DC Microgrid. IEEE Transactions on Power Electronics, Vol. 30(12), December 2015.
22. Lu, X.; Guerrero, J. M.; Sun, K.; Vasquez, J. C. An Improved Droop Control Method for DC Microgrids Based on Low Bandwidth Communication with DC Bus Voltage

Restoration and Enhanced Current Sharing Accuracy. IEEE Transactions on Power Electronics, Vol. 29(4), April 2014.

23. Sahoo, S.; Zhang, C.; Pullaguram, D. R.; Mishra, S.; Wu, J.; Senroya, N. Investigation of Distributed Cooperative Control for DC Microgrids in Different Communication Medium, Energy Procedia, Vol. 142, December 2017.
24. Varghese, A.; Chandran, L. R.; Rajendran, A. Power Flow Control of Solar PV Based Islanded Low Voltage DC Microgrid with Battery Management System. In Proceedings of the IEEE 1st International Conference on Power Electronics, Intelligent Control and Energy Systems (ICPEICES), Delhi, India, 4-6 July 2016.
25. Guerrero, J. M.; Vasquez, J. C.; Matas, J.; De Vicuna, L. G.; Castilla, M. Hierarchical Control of Droop-Controlled AC and DC Microgrids-A General Approach Toward Standardization. IEEE Transactions on Industrial Electronics, Vol. 58(1), January 2011.
26. Vasquez, J. C.; Guerrero, J. M.; Miret, J.; Castilla, M.; De Vicuna, L. G. Hierarchical Control of Intelligent Microgrids. IEEE Industrial Electronics Magazine, Vol. 4(4), December 2010.
27. Meng, L.; Savaghebi, M.; Andrade, F.; Vasquez, J. C.; Guerrero, J. M.; Graells, M. Microgrid Central Controller Development and Hierarchical Control Implementation in the Intelligent Microgrid Lab of Aalborg University. In Proceedings of the IEEE Applied Power Electronics Conference and Exposition (APEC), Charlotte, NC, USA, 15-19 March 2015.
28. Unamuno, E.; Barrena, J. A. Hybrid AC/DC Microgrids-Part II: Review and Classification of Control Strategies. Renewable and Sustainable Energy Reviews, Vol. 52, December 2015.
29. Feng, X.; Shekhar, A.; Yang, F.; Hebner, R. E.; Bauer, P. Comparison of Hierarchical Control and Distributed Control for Microgrid. Electric Power Components and Systems, July 2017.
30. Marzal, S.; González-Medina, R.; Salas-Puente, R.; Figueres, E.; Garcerá, G. A Novel Locality Algorithm and Peer-to-Peer Communication Infrastructure for Optimizing Network Performance in Smart Microgrids. Energies, Aug. 2017.

31. Kaura, A.; Kaushalb, J.; Basakc, P. A Review on Microgrid Central Controller. Renewable and Sustainable Energy Reviews, Vol. (55), March 2016.
32. Begum, M.; Abuhilaleh, M.; Li, L.; Zhu, J. Distributed Secondary Voltage Regulation for Autonomous Microgrid. In Proceedings of the 20th International Conference on Electrical Machines and Systems (ICEMS), Sydney, Australia, 11-14 August 2017.
33. Wu, D.; Tang, F.; Dragicevic, T.; Guerrero, J. M.; Vasquez, J. C. Coordinated Control Based on Bus-Signaling and Virtual Inertia for Islanded DC Microgrids. IEEE Transactions on Smart Grid, Vol. 6(6), November 2015.
34. Shi, D.; Chen, X.; Wang, Z.; Zhang, X.; Yu, Z.; Wang, X.; Bian, D. A Distributed Cooperative Control Framework for Synchronized Reconnection of a Multi-Bus Microgrid. IEEE Transactions on Smart Grid, Vol. 9(6), November 2018.
35. Dou, C.; Zhang, Z.; Yue, D.; Zheng, Y. MAS-Based Hierarchical Distributed Coordinate Control Strategy of Virtual Power Source Voltage in Low-Voltage Microgrid. IEEE Access, Vol. 5, June 2017.
36. Bidram, A.; Lewis, F. L.; Davoudi, A. Distributed Control Systems for Small-Scale Power Networks: Using Multiagent Cooperative Control Theory. IEEE Control Systems Magazine, Vol. 34(6), December 2014.
37. Fernandez, L. P.; San Roman, T. G.; Cossent, R.; Domingo, C. M.; Frias, P. Assessment of the Impact of Plug-in Electric Vehicles on Distribution Networks. IEEE Transactions on Power Systems, Vol. 26(1), February 2011.
38. Ying, H. H.; Han, H. J.; Jun, W. X.; Qi, T. W. Optimal Control Strategy of Vehicle-To-Grid for Modifying the Load Curve Based on Discrete Particle Swarm Algorithm. In Proceedings of the 4th International Conference on Electric Utility Deregulation and Restructuring and Power Technologies (DRPT), Weihai, China, 6-9 July 2011.
39. Jiang, B.; Fei, Y. Decentralized Scheduling of PEV On-Street Parking and Charging for Smart Grid Reactive Power Compensation. In Proceedings of the IEEE PES Innovative Smart Grid Technologies Conference (ISGT), Washington, DC, USA, 24-27 February 2013.
40. Falahi, M.; Chou, H. M.; Ehsani, M.; Xie, L.; Butler-Purry K. L. Potential Power Quality Benefits of Electric Vehicles. IEEE Transactions on Sustainable Energy, October 2013.

41. Bao, K.; Li, S.; Zheng, H. Battery Charge and Discharge Control for Energy Management in EV and Utility Integration. In Proceedings of the IEEE Power and Energy Society General Meeting, San Diego, CA, USA, 22–26 July 2012.
42. Kisacikoglu, M. C.; Ozpineci, B.; Tolbert, L. M. Examination of a PHEV Bidirectional Charger System for V2G Reactive Power Compensation. In Proceedings of the Twenty-Fifth Annual IEEE Applied Power Electronics Conference and Exposition (APEC), Palm Springs, CA, USA, 21-25 February 2010.
43. Ferreira, R. J.; Miranda, L. M.; Araújo, R. E.; Lopes, J. P. A New Bi-Directional Charger for Vehicle-to-Grid Integration. In Proceedings of the 2nd IEEE PES International Conference and Exhibition on Innovative Smart Grid Technologies, Manchester, UK, 5-7 December 2011.
44. Kadurek, P.; Ioakimidis, C.; Ferrao, P. Electric Vehicles and Their Impact to the Electric Grid in Isolated Systems. In Proceedings of the International Conference on Power Engineering, Energy and Electrical Drives, Lisbon, Portugal, 18-20 March 2009.
45. Onar, O.; Khaligh, A. Grid Interactions and Stability Analysis of a Distributed Network with Plug-in Hybrid Electric Vehicle Loads. In Proceedings of the 25th Annual IEEE Applied Power Electronics Conference and Exposition (APEC), Palm Springs, CA, USA, 21-25 February 2010.
46. Erb, D. C.; Onar, O.; Khaligh, A. Bi-directional Charging Topologies for Plug-in Hybrid Electric Vehicles. In Proceedings of the 25th Annual IEEE Applied Power Electronics Conference and Exposition (APEC), Palm Springs, CA, USA, 21-25 February 2010.
47. Musavi, F.; Edington, M.; Eberle, W.; Dunford, W. G. Energy Efficiency in Plug-in Hybrid Electric Vehicle Chargers: Evaluation and Comparison of Front End AC-DC Topologies. In Proceedings of the IEEE Energy Conversion Congress and Exposition, Phoenix, AZ, USA, 17-22 September 2011.
48. Musavi, F.; Eberle, W.; Dunford, W. G. A Phase Shifted Semi-Bridgeless Boost Power Factor Corrected Converter for Plug in Hybrid Electric Vehicle Battery Chargers. In Proceedings of the 26th Annual IEEE Applied Power Electronics Conference and Exposition (APEC), Fort Worth, TX, USA, 6-11 March 2011.

49. Musavi, F.; Eberle, W.; Dunford, W. G. A High-Performance Single-Phase Bridgeless Interleaved PFC Converter for Plug-in Hybrid Electric Vehicle Battery Chargers. IEEE Transactions on Industry Applications, Vol. 47(4), May 2011.
50. Sahu, B.; Rincon-Mora, G. A. A Low Voltage, Dynamic, Noninverting, Synchronous Buck-Boost Converter for Portable Applications. IEEE Transactions on Power Electronics, Vol. 19(2), March 2004.
51. Huang, P. C.; Wu, W. Q.; Ho, H. H.; Chen, K. H. Hybrid Buck-Boost Feedforward and Reduced Average Inductor Current Techniques in Fast Line Transient and High-Efficiency Buck-Boost Converter. IEEE Transactions on Power Electronics, Vol. 25(3), March 2010.
52. Waffler, S.; Kolar, J. W. "A Novel Low-Loss Modulation Strategy for High-Power Bidirectional Buck + Boost Converters. IEEE Transactions on Power Electronics, Vol. 24(6), June 2009.
53. Camara, M. B.; Gualous, H.; Gustin, F.; Berthon, A.; Dakyo, B. DC/DC Converter Design for Supercapacitor and Battery Power Management in Hybrid Vehicle Applications-Polynomial Control Strategy. IEEE Transactions on Industrial Electronics, Vol. 57(2), February 2010.
54. Ghanem, M. C.; Al-Haddad, K.; Roy, G. A New Control Strategy to Achieve Sinusoidal Line Current in A Cascade Buck-Boost Converter. IEEE Transactions on Industrial Electronics, Vol. 43(3), June 1996.
55. Gabriault, M.; Notman, A. A High Efficiency, Noninverting, Buck-Boost DC-DC Converter. In Proceedings of the 19th Annual IEEE Applied Power Electronics Conference and Exposition, Anaheim, CA, USA, 22-26 February 2004.
56. Midya, P.; Haddad, K.; Miller, M. Buck or Boost Tracking Power Controller. IEEE Transactions on Power Electronics, Vol. 2(4), December 2004.
57. Hwu, K. I.; Yau, Y. T. Two Types of KY Buck-Boost Converters. IEEE Transactions on Industrial Electronics, Vol. 56(8), August 2009.
58. Xu, D.; Zhao, C.; Fan, H. A PWM Plus Phase-Shift Control Bidirectional DC-DC Converter. IEEE Transactions on Power Electronics, Vol. 19(3), May 2004.

59. Gang, M.; Yuanyuan, L.; Wenlong, Q. A Novel Soft Switching Bidirectional DC/DC Converter and Its Output Characteristic. In Proceedings of the IEEE Region 10 Conference, Hong Kong, China, 14-17 November 2006.
60. Krismer, F.; Biela, J.; Kolar, J. W. A Comparative Evaluation of Isolated Bi-directional DC/DC Converters with Wide Input and Output Voltage Range. 14th IAS Annual Meeting. Conference Record of the 2005 Industry Applications Conference, Hong Kong, China, 2-6 October 2005.
61. Tsuruta, Y.; Ito, Y.; Kawamura, A. Snubber-Assisted Zero-Voltage and Zero-Current Transition Bilateral Buck and Boost Chopper for EV Drive Application and Test Evaluation at 25 kW. IEEE Transactions on Industrial Electronics, Vol. 56(1), January 2009.
62. Jung, D. Y.; Hwang, S. H.; Ji, Y. H.; Lee, J. H.; Jung, Y. C.; Won, C. Y. Soft-Switching Bidirectional DC/DC Converter with a LC Series Resonant Circuit. IEEE Transactions on Power Electronics, Vol. 28(4), April 2013.
63. Wu, H.; Lu, J.; Shi, W.; Xing, Y. Nonisolated Bidirectional DC-DC Converters with Negative-Coupled Inductor. IEEE Transactions on Power Electronics, Vol. 27(5), May 2012.
64. Do, H. L. Nonisolated Bidirectional Zero-Voltage-Switching DC-DC Converter. IEEE Transactions on Power Electronics, Vol. 26(9), September 2011.
65. Arancibia, A.; Strunz, K. Modeling of an Electric Vehicle Charging Station for Fast DC Charging. In Proceedings of the IEEE International Electric Vehicle Conference, Greenville, SC, USA, 4-8 March 2012.
66. Aggeler, D.; Canales, F.; Parra, H. Z. D. L.; Coccia, A.; Butcher, N.; Apeldoorn, O. Ultra-Fast DC-Charge Infrastructures for EV-Mobility and Future Smart Grids. In Proceedings of the IEEE PES Innovative Smart Grid Technologies Conference Europe (ISGT Europe), Gothenburg, Sweden, 11-13 October 2010.
67. Gamboa, G.; Hamilton, C.; Kerley, R.; Elmes, S.; Arias, A.; Shen, J.; Batarseh, I. Control Strategy of a Multi-Port, Grid Connected, Direct-DC PV Charging Station for Plug-in Electric Vehicles. In Proceedings of the IEEE Energy Conversion Congress and Exposition, Phoenix, AZ, USA, 17-22 September 2010.

68. Takagi, M.; Yamaji, K.; Yamamoto, H. Power System Stabilization by Charging Power Management of Plug-in Hybrid Electric Vehicles with LFC Signal. In Proceedings of the IEEE Vehicle Power and Propulsion Conference, Dearborn, MI, USA, 7-10 September 2009.
69. Ota, Y.; Taniguchi, H.; Nakajima, T.; Liyanage, K. M.; Baba, J.; Yokoyama, A. Autonomous Distributed V2G (Vehicle-to-Grid) Considering Charging Request and Battery Condition. In Proceedings of the IEEE PES Innovative Smart Grid Technologies Conference Europe (ISGT Europe), Gothenburg, Sweden, 11-13 October 2010.
70. Ota, Y.; Taniguchi, H.; Nakajima, T.; Liyanage, K. M.; Baba, J.; Yokoyama, A. Autonomous Distributed V2G (Vehicle-to-Grid) Satisfying Scheduled Charging. IEEE Transactions on Smart Grid, Vol. 3(1), March 2012.
71. Li, C. T.; Ahn, C.; Peng, H.; Sun, J. Synergistic Control of Plug-in Vehicle Charging and Wind Power Scheduling. IEEE Transactions on Power Systems, Vol. 28(2), May 2013.
72. Yang, H.; Chung, C. Y.; Zhao, J. Application of Plug-in Electric Vehicles to Frequency Regulation Based on Distributed Signal Acquisition via Limited Communication. IEEE Transactions on Power Systems, Vol. 28(2), May 2013.
73. Liu, H.; Hu, Z.; Song, Y.; Lin, J. Decentralized Vehicle-to-Grid Control for Primary Frequency Regulation Considering Charging Demands. IEEE Transactions on Power Systems, Vol. 28(3), August 2013.
74. Masuta, T.; Yokoyama, A. Supplementary Load Frequency Control by Use of a Number of Both Electric Vehicles and Heat Pump Water Heaters. IEEE Transactions on Smart Grid, Vol. 3(3), September 2012.
75. Arya, Y.; Kumar, N.; Mathur, H. D. Automatic Generation Control in Multi Area Interconnected Power System by using HVDC Links. International Journal of Power Electronics and Drive Systems, Vol. 2(1), March 2012.
76. Vachirasricirikul, S.; Ngamroo, I. Robust LFC in a Smart Grid with Wind Power Penetration by Coordinated V2G Control and Frequency Controller. IEEE Transactions on Smart Grid, Vol. 5(1), January 2014.

77. Jayakumar, A.; Chalmers, A.; Lie, T. T. Review of Prospects for Adoption of Fuel Cell Electric Vehicles in New Zealand. IET Electrical Systems in Transportation, Vol. 7(4), December 2017.
78. Mathworks, "24-hour Simulation of a Vehicle-to-Grid (V2G) System," [Online]. Available: https://www.mathworks.com/help/physmod/sps/examples/24-hour-simulation-of-a-vehicle-to-grid-v2g-system.html, [Accessed: 1 April 2019].
79. Xu, L.; Williams, B.; Yao, L. Multi-Terminal DC Transmission Systems for Connecting Large Offshore Wind Farms. In Proceedings of the IEEE Power Energy Society General Meeting Conversion and Delivery of Electrical Energy 21st Century, Pittsburgh, PA, USA, 20–24 July 2008.
80. Liang, J.; Jing, T.; Gomis-Bellmunt, O. Operation and Control of Multi-Terminal HVDC Transmission for Offshore Wind Farms. IEEE Trans. Power Deliv. 2011, 26, 2596–2604.
81. Aragues, M.; Egea, A.; Gomis, O.; Sumper, A. Optimum Voltage Control for Loss Minimization in HVDC Multi-Terminal Transmission Systems for Large Offshore Wind Farms. Electr. Power Syst. Res. 2012, 89, 54-63.
82. Meah, K.; Sadrul Ula, A.H.M. Simulation Study of the CIGRE HVDC Benchmark Model with the WSCC Nine-bus Power System Network. In Proceedings of the 2009 IEEE/PES Power Systems Conference and Exposition, Seattle, WA, USA, 15–18 March 2009.
83. Van Hertem, D.; Ghandhari, M. Multi-Terminal VSC HVDC for the European Supergrid: Obstacles. Renewable and Sustainable Energy Rev. 2010, 14, 3156–3163.
84. Wang, F.; Bertling, L.; Le, T. An Overview Introduction of VSC-HVDC: State-of-Art and Potential Applications in Electric Power Systems. In Proceedings of the CIGRÈ International Symposium, Bologna, Italy September 2011.
85. Beerten, J.; Cole, S.; Belmans, R. Modeling of Multi-Terminal VSC HVDC Systems with Distributed DC Voltage Control. IEEE Trans. Power Syst. 2014, 29, 34-42.
86. Tang, G.; He, Z.; Pang, H. R&D and Application of Voltage Sourced Converter Based High Voltage Direct Current Engineering Technology in China. J. Mod. Power Syst. Clean Energy 2014, 2, 1-15.

87. Pullaiah, G.; Venkata Subbaiah, R. Modelling of VSC-HVDC Link. Int. J. Innov. Res. Sci. Technol. 2014, 1, 106–114.
88. Pegueroles, J.; Barnes, M.; Gomis, O.; Beddard, A.; Bianchi, F. D. Modelling and Analysis of CIGRE HVDC Offshore Multi-Terminal Benchmark Grid. Energy Procedia 2015, 81, 72–82.
89. Hao, H.; Yang, L.; Rishang, L.; Tao, T.; Yuan, M.; Jianhua, Z.; Yunfei, X.; Guofeng, J. PSCAD/EMTDC-Based Modeling and Simulation of Three-Terminal VSC-HVDC System. In Proceedings of the 5th International Conference on Civil, Architectural and Hydraulic Engineering (ICCAHE 2016), Zhuhai, China, 30–31 July 2016.
90. Djehaf, M. A.; Zidi, S. A.; Djilani Kobibi, Y. Modeling of a Multi-Level Converter Based MTDC System for the Study of Power System Steady-State and Transient Characteristics. J. Electr. Eng. 2016, 16, 116–124.
91. Zhang, Y.; Ding, H.; Kuffel, R. Key Techniques in Real Time Digital Simulation for Closed-loop Testing of HVDC Systems. CSEE J. Power Energy Syst. 2017, 3, 125–130.
92. An, T.; Han, C.; Wu, Y.; Tang, G. HVDC Grid Test Models for Different Application Scenarios and Load Flow Studies. J. Mod. Power Syst. Clean Energy 2017, 5, 262–274.
93. Rodriguez, P.; Rouzbehi, K. Multi-Terminal DC Grids: Challenges and Prospects. J. Mod. Power Syst. Clean Energy 2017, 5, 515–522.
94. Beerten, J.; Belmans, R. Modeling and Control of Multi-terminal VSC HVDC Systems. Energy Procedia 2012, 24, 123–130.
95. Haileselassie, T.M.; Uhlen, K. Primary Frequency Control of Remote Grids Connected by Multi-terminal HVDC. In Proceedings of the IEEE PES General Meeting, Providence, RI, USA, 25–29 July 2010.
96. Dierckxsens, C.; Srivastava, K.; Reza, M.; Cole, S.; Beerten, J.; Belmans, R. A Distributed DC Voltage Control Method for VSC MTDC Systems. Electr. Power Syst. Res. 2012, 82, 54–58.
97. Wenig, S.; Rink, Y.; Leibfried, T. Multi-Terminal HVDC Control Strategies Applied to the CIGRE B4 DC Grid Test System. In Proceedings of the 49th International

Universities Power Engineering Conference (UPEC), Cluj-Napoca, Romania, 2–5 September 2014.

98. Andreasson, M.; Wiget, R.; Dimarogona, D. V.; Johansson, K. H.; Andersson, G. Coordinated Frequency Control through MTDC Transmission Systems. IFAC Proc. 2015, 48, 106–111.
99. Andreasson, M.; Wiget, R.; Dimarogonas, D.V.; Johansson, K. H.; Andersson, G. Distributed Secondary Frequency Control through MTDC Transmission Systems. In Proceedings of the 54th IEEE Conference on Decision and Control (CDC), Osaka, Japan, 15–18 December 2015.
100. Endegnanew, A. G.; Uhlen, K. Coordinated Converter Control Strategy in Hybrid AC/DC Power Systems for System Frequency Support. Energy Procedia 2016, 94, 173–181.
101. Wang, W.; Li Y.; Cao Y.; Häger U.; Rehtanz C. Adaptive Droop Control of VSC-MTDC System for Frequency Support and Power Sharing. IEEE Trans. Power Syst. 2018, 33, 1264–1274.
102. Che, Y.; Zhou, J.; Li, W.; Zhu, J.; Hong, C. Advanced Droop Control Scheme in Multi-Terminal DC Transmission Systems. J. Electr. Eng. Technol. 2018, 13, 1060–1068.
103. Lu, W.; Ooi, B. T. Optimal Acquisition and Aggregation of Offshore Wind Power by Multiterminal Voltage Source HVDC. IEEE Trans. Power Deliv. 2003, 18, 201–206.
104. Ekanayake, J. B. Multi-terminal DC Converters for Connecting Induction Generator Based Distribution Generation. In Proceedings of the 4th International Conference on Industrial and Information Systems, Sri Lanka, Sri Lanka, 28–31 December 2009.
105. Xu, L.; Yao, L. DC Voltage Control and Power Dispatch of a Multi-terminal HVDC System for Integrating Large Offshore Wind Farms. IET Renew. Power Gener. 2011, 5, 223–233.
106. Pinto, R. T.; Rodrigues, S. F.; Wiggelinkhuizen, E.; Scherrer, R.; Bauer, P.; Pierik, J. Operation and Power Flow Control of Multi-Terminal DC Networks for Grid Integration of Offshore Wind Farms Using Genetic Algorithms. Energies 2013, 6, 1–26.

107. Kankanala, P.; Srivastava, S. C.; Srivastava, A. K.; Schulz, N. N. Optimal Control of Voltage and Power in a Multi-Zonal MVDC Shipboard Power System. IEEE Trans. Power Syst. 2012, 27, 642–650.
108. Rudion, K.; Orths, A. G.; Eriksen, P. B. Offshore Power System Operation Planning Considering Energy Market Schedules. In Proceedings of the 2012 IEEE Power and Energy Society General Meeting, San Diego, CA, USA, 22–26 July 2012.
109. Zhao, X.; Li, K. Adaptive Backstepping Droop Controller Design for Multi-Terminal High-Voltage Direct Current Systems. IET Gener. Transm. Distrib. 2015, 9, 975–983.
110. Sandano, R.; Farrell, M.; Basu, M. Enhanced Master/Slave Control Strategy Enabling Grid Support Services and Offshore Wind Power Dispatch in a Multi-Terminal VSC HVDC Transmission System. Renew. Energy 2017, 113, 1580–1588.
111. Tokiwa, Y.; Ichikawa, F.; Suzuki, K. Novel Control Strategies for HVDC System with Self-Contained Converter. Electr. Eng. Jpn. 1993, 113, 1–13.
112. Nakajima, T.; Irokawa, S. A Control System for HVDC Transmission by Voltage Sourced Converters. In Proceedings of the 1999 IEEE PES Summer Meeting, Edmonton, AB, Canada, 18–22 July 1999.
113. Zhu, J.; Booth, C. Future Multi-Terminal HVDC Transmission Systems Using Voltage Source Converters. In Proceedings of the 45th International Universities Power Engineering Conference, Wales, UK, 31 August–3 September 2010.
114. Ismunandar, C.; Meer, A.; Hendriks, R. L.; Gibescu, M.; Kling, W. Control of Multi-Terminal VSC-HVDC for Wind Power Integration Using the Voltage Margin Method. In Proceedings of the 9th International Workshop on Large Scale Integration of Wind Power into Power Systems, Québec City, Québec, Canada, 18–19 October 2010.
115. Teixeira Pinto, R.; Rodrigues, S. F.; Bauer, P.; Pierik, J. Comparison of Direct Voltage Control Methods of Multi-Terminal DC (MTDC) Networks through Modular Dynamic Models. In Proceedings of the 14th European Conference on Power Electronics and Applications, Birmingham, UK, 30 August–1 September 2011.
116. Mier, V.; Casielles, P.G.; Coto, J.; Zeni, L. Voltage Margin Control for Offshore Multi-Use Platform Integration. In Proceedings of the 2012 International Conference on Renewable Energies and Quality, Santiago de Compostela, Spain, 28–30 March 2012.

117. De Brabandere, K.; Bolsens, B.; Van den Keybus, J.; Woyte, A.; Driesen, J.; Belmans, R. A Voltage and Frequency Droop Control Method for Parallel Inverters. IEEE Trans. Power Electron. 2007, 22, 1107–1115.
118. Egea-Alvarez, A.; Beerten, J.; Van Hertem, D.; Gomis-Bellmunt, O. Primary and Secondary Power Control of Multiterminal HVDC Grids. In Proceedings of the 10th IET International Conference on AC and DC Power Transmission, Birmingham, UK, 4–5 December 2012.
119. Rouzbehi, K.; Miranian, A.; Candela, J. I.; Luna, A.; Rodriguez, P. A Generalized Voltage Droop Strategy for Control of Multiterminal DC Grids. IEEE Trans. Ind. Appl. 2015, 51, 607–618.
120. Chaudhuri, N.R.; Majumder, R.; Chaudhuri, B. System Frequency Support Through Multi-Terminal DC (MTDC) Grids. IEEE Trans. Power Syst. 2013, 28, 347–356.
121. Rault, P.; Guillaud, X.; Colas, F.; Nguefeu, S. Investigation on Interactions between AC and DC Grids. In Proceedings of the 2013 IEEE Grenoble Conference, Grenoble, France, 16–20 June 2013.
122. Martínez Sanz, I.; Chaudhuri, B.; Strbac, G. Frequency Changes in AC Systems Connected to DC Grids: Impact of AC vs. DC Side Events. In Proceedings of the 2014 IEEE PES General Meeting, Conference, and Exposition, National Harbor, MD, USA, 27–31 July 2014.
123. Papangelis, L.; Guillaud, X.; Van Cutsem, T. Frequency Support Among Asynchronous AC Systems Through VSCs Emulating Power Plants. In Proceedings of the 11th IET International Conference on AC and DC Power Transmission, Birmingham, UK, 10–12 February 2015.
124. Pinto, R. T.; Bauer, P.; Rodrigues, S. F.; Wiggelinkhuizen, E. J.; Pierik, J.; Ferreira, B. A Novel Distributed Direct-Voltage Control Strategy for Grid Integration of Offshore Wind Energy Systems through MTDC Network. IEEE Trans. Ind. Electron. 2013, 60, 2429–2441.
125. Rodrigues, S.; Pinto, R. T.; Bauer, P.; Pierik, J. Optimal Power Flow Control of VSC-Based Multiterminal DC Network for Offshore Wind Integration in the North Sea. IEEE J. Emerg. Sel. Top. Power Electron. 2013, 1, 260–268.

126. Aragüés-Peñalba, M.; Egea-Àlvarez, A.; Arellano, S. G.; Gomis-Bellmunt, O. Droop Control for Loss Minimization in HVDC Multi-Terminal Transmission Systems for Large Offshore Wind Farms. Electr. Power Syst. Res. 2014, 112, 48–45.
127. Beerten, J.; Belmans, R. Analysis of Power Sharing and Voltage Deviations in Droop-Controlled DC Grids. IEEE Trans. Power Syst. 2014, 28, 4588-4597.
128. Prieto-Araujo, E.; Egea-Alvarez, A.; Fekriasl, S. F.; Gomis-Bellmunt, O. DC Voltage Droop Control Design for Multi-Terminal HVDC Systems Considering AC and DC Grid Dynamics. IEEE Trans. Power Deliv. 2016, 31, 575–585.
129. Vasquez, C.; Guerrero, J. M.; Luna, A.; Rodriguez, P.; Teodorescu, R. Adaptive Droop Control Applied to Voltage-Source Inverters Operating in Grid-Connected and Islanded Modes. IEEE Trans. Ind. Electron. 2009, 56, 4088–4096.
130. Hendriks, R.L.; Van Der Meer, A.A.; Kling, W.L. Impact on System Stability of Different Voltage Control Schemes of Wind Power Plants Connected Through AC and VSC-HVDC Transmission. In Proceedings of the Nordic Wind Power Conference, Rönne, Denmark, 10–15 September 2009.
131. Prieto-Araujo, E.; Bianchi, F. D.; Junyent-Ferre, A.; Gomis-Bellmunt, O. Methodology for Droop Control Dynamic Analysis of Multi-Terminal VSC-HVDC Grids for Offshore Wind Farms. IEEE Trans. Power Deliv. 2011, 26, 2476–2485.
132. Haileselassie, T. M.; Uhlen, K. Impact of DC Line Voltage Drops on Power Flow of MTDC Using Droop Control. IEEE Trans. Power Syst. 2012, 27, 1441–1449.
133. Chaudhuri, N. R.; Chaudhuri, B. Adaptive Droop Control for Effective Power Sharing in Multi-Terminal DC (MTDC) Grids. IEEE Trans. Power Syst. 2013, 28, 21–29.
134. Abdel-Khalik, A. S.; Massoud, A. M.; Elserougi, A. A.; Ahmed, S. Optimum Power Transmission-Based Droop Control Design for Multi-Terminal HVDC of Offshore Wind Farms. IEEE Trans. Power Syst. 2013, 28, 3401–3409.
135. Eriksson, R.; Beerten, J.; Ghandhari, M. Optimizing DC Voltage Droop Settings for AC/DC System Interactions. IEEE Trans. Power Deliv. 2014, 29, 362–369.
136. Mohammadi, F.; Nazri, G.-A.; Saif, M. A Bidirectional Power Charging Control Strategy for Plug-in Hybrid Electric Vehicles. Sustainability 2019, 11, 4317.
137. Bahrman, M. P.; Johnson, B. K. The ABCs of HVDC Transmission Technologies. IEEE Power Energy Mag. 2007, 5, 32–44.

138. Flourentzou, N.; Agelidis, V. G.; Demetriades, G. D. VSC-Based HVDC Power Transmission Systems: An Overview. IEEE Trans. Power Electron. 2009, 24, 592–602.
139. Mohammadi, F.; Nazri, G.-A.; Saif, M. An Improved Droop-Based Control Strategy for MT-HVDC Systems. Electronics, 2020, 9, 87.
140. Xu, L.; Fan, L. Impedance-Based Resonance Analysis in a VSC-HVDC System. IEEE Trans. Power Deliv. 2013, 28, 2209–2216.
141. Xu, L.; Fan, L.; Miao, Z. DC Impedance-Model-Based Resonance Analysis of a VSC-HVDC System. IEEE Trans. Power Deliv. 2015, 30, 1221–1230.
142. Pandya, K. S.; Joshi, S. K. A Survey of Optimal Power Flow Methods. J. Theor. Appl. Inf. Technol. 2008, 4. 450–458.
143. Frank, S.; Steponavice, I.; Rebennack, S. Optimal Power Flow: A Bibliographic Survey II: Non-Deterministic and Hybrid Methods. Energy Syst. 2012, 3, 259–289.
144. Mohammadi, F.; Nazri, G.-A.; Saif, M. A New Topology of a Fast Proactive Hybrid DC Circuit Breaker for MT-HVDC Grids. Sustainability 2019, 11, 4493.
145. Mohammadi, F.; Nazri, G.-A.; Saif, M. A Fast Fault Detection and Identification Approach in Power Distribution Systems. In Proceedings of the 5th International Conference on Power Generation Systems and Renewable Energy Technologies (PGSRET), Istanbul, Turkey, 26–27 August 2019.
146. Arrillaga, J.; Bodger, P. Integration of HVDC Links with Fast-Decoupled Load-Flow Solutions, Proceedings of the Institution of Electrical Engineers. 1977, 124, 463–468.
147. Baradar, M.; Ghandhari, M.; van Hertem, D. The Modeling Multi-Terminal VSC-HVDC in Power Flow Calculation using Unified Methodology. In Proceedings of the 2nd IEEE PES International Conference and Exhibition on Innovative Smart Grid Technologies, Manchester, UK, 5–7 December 2011.
148. Baradar, M.; Ghandhari, M. A Multi-Option Unified Power-Flow Approach for Hybrid AC/DC Grids Incorporating Multi-terminal VSC-HVDC. IEEE Trans. Power Syst. 2013, 28, 2376–2383.
149. El-Hawary, M. E.; Ibrahim, S. T. A New Approach to AC-DC Load Flow Analysis. Electr. Power Syst. Res. 1995, 33, 193–200.

150. Beerten, J.; van Hertem, D.; Belmans, R. VSC-MTDC Systems with a Distributed DC Voltage Control-A Power Flow Approach. In Proceedings of the 2011 IEEE Trondheim PowerTech, Trondheim, Norway, 19–23 June 2011.
151. Haileselassie, T. M.; Uhlen, K. Power Flow Analysis of Multi-Terminal HVDC Networks. In Proceedings of the 2011 IEEE Trondheim PowerTech, Trondheim, Norway, 19–23 June 2011.
152. Beerten, J.; Cole, S.; Belmans, R. Implementation Aspects of a Sequential AC/DC Power Flow Computation Algorithm for Multi-Terminal VSC-HVDC Systems. In Proceedings of the 9th IET International Conference on AC and DC Power Transmission, London, UK, 19–21 October 2010.
153. Beerten, J.; Cole, S.; Belmans, R. A Sequential AC/DC Power Flow Algorithm for Networks Containing Multi-Terminal VSC-HVDC Systems. In Proceedings of the IEEE PES General Meeting, Providence, RI, USA, 25–29 July 2010.
154. Beerten, J.; Cole, S.; Belmans, R. Generalized Steady-State VSC MTDC Model for Sequential AC/DC Power Flow Algorithms. IEEE Trans. Power Syst. 2012, 27, 821–829.
155. Gonzalez-Longatt, F.; Roldan, J.; Charalambous, C. A. Power Flow Solution on Multi-Terminal HVDC Systems: Supergrid Case. In Proceedings of the International Conference on Renewable Energies and Power Quality, Santiago de Compostela, Galicia, Spain, 28–30 March 2012.
156. Hendriks, R. L.; Paap, G. C.; Kling, W. L. Control of a Multi-Terminal VSC Transmission Scheme for Interconnecting Offshore Wind Farms. In Proceedings of the European Wind Energy Conference and Exhibition, Milan, Italy, 7–10 May 2007.
157. Yang, Z.; Zhong, H.; Bose, A.; Xia, Q.; Kang, C. Optimal Power Flow in AC-DC Grids with Discrete Control Devices. IEEE Trans. Power Syst. 2018, 33, 1461–1472.
158. Jiang, H.; Zhang, J.J.; Gao, W.; Wu, Z. Fault Detection, Identification, and Location in Smart Grid Based on Data-Driven Computational Methods. IEEE Trans. Smart Grid 2014, 5, 2947–2956.
159. Bucher, M. K.; Franck, C. M. Analytic Approximation of Fault Current Contributions from Capacitive Components in HVDC Cable Networks. IEEE Trans. Power Deliv. 2015, 30, 74-81.

160. Shukla, A.; Demetriades, G. D. A Survey on Hybrid Circuit-Breaker Topologies. IEEE Trans. Power Deliv. 2015, 30, 627-641.
161. Hassanpoor, A.; Häfner, J.; Jacobson, B. Technical Assessment of Load Commutation Switch in Hybrid HVDC Breaker. IEEE Trans. Power Electron. 2015, 30, 5393-5400.
162. Belda, N. A.; Smeets, R. P. P. Test Circuits for HVDC Circuit Breakers. IEEE Trans. Power Deliv. 2017, 32, 285-293.
163. Kontos, E.; Pinto, R. T.; Rodrigues, S.; Bauer, P. Impact of HVDC Transmission System Topology on Multiterminal DC Network Faults. IEEE Trans. Power Deliv. 2015, 30, 844-852.
164. Sneath, J.; Rajapakse, A. D. Fault Detection and Interruption in an Earthed HVDC Grid using ROCOV and Hybrid DC Breakers. IEEE Trans. Power Deliv. 2016, 31, 973-981.
165. Ahmed, N.; Ängquist, L.; Mehmood, S.; Antonopoulos, A.; Harnefors, L.; Norrga, S.; Nee, H. P. Efficient Modeling of an MMC-Based Multiterminal DC System Employing Hybrid HVDC Breakers. In Proceedings of the IEEE Power and Energy Society General Meeting (PESGM), Boston, MA, USA, 17-21 July 2016.
166. Jovcic, D.; Taherbaneh, M.; Taisne, J. P.; Nguefeu, S. Offshore DC Grids as an Interconnection of Radial Systems: Protection and Control Aspects. IEEE Trans. Smart Grid 2015, 6, 903-910.
167. Cwikowski, O.; Barnes, M.; Shuttleworth, R.; Chang, B. Analysis and Simulation of the Proactive Hybrid Circuit Breaker. In Proceedings of the 2015 IEEE 11th International Conference on Power Electronics and Drive Systems, Sydney, Australia, 9-12 June 2015.
168. Wang, Y.; Marquardt, R. Future HVDC-Grids Employing Modular Multilevel Converters and Hybrid DC-Breakers. In Proceedings of the 15th European Conference on Power Electronics and Applications (EPE), Lille, France, 2-6 September 2013.
169. Wang, Y.; Marquardt, R. A Fast Switching, Scalable DC-Breaker for Meshed HVDC-SuperGrids. In Proceedings of the International Exhibition and Conference for Power Electronics, Intelligent Motion, Renewable Energy and Energy Management, Nuremberg, Germany, 20-22 May 2014.

170. Mokhberdoran, A.; Carvalho, A.; Leite, H.; Silva, N. A Review on HVDC Circuit Breakers. In Proceedings of the 3rd Renewable Power Generation Conference, Naples, Italy, 24-25 September 2014.
171. Guo, Q.; Yoon, M.; Park, J.; Jang, G. Novel Topology of DC Circuit Breaker and Current Interruption in HVDC Networks. IEEJ Trans. Electr. Electron. Eng. 2017, 12, 465-473.
172. Tokoyoda, S.; Sato, M.; Kamei, K.; Yoshida, D.; Miyashita, M.; Kikuchi, K.; Ito, H. High Frequency Interruption Characteristics of VCB and Its Application to High Voltage DC Circuit Breaker. In Proceedings of the 3rd International Conference on Electric Power Equipment - Switching Technology, Busan, South Korea, 25-28 October 2015.
173. Corzine, K. A. A New-Coupled-Inductor Circuit Breaker for DC Applications. IEEE Trans. Power Electron. 2017, 32, 1411-1418.
174. Keshavarzi, D.; Ghanbari, T.; Farjah, E. A Z-Source-Based Bidirectional DC Circuit Breaker with Fault Current Limitation and Interruption Capabilities. IEEE Trans. Power Electron. 2017, 32, 6813-6822.
175. Maqsood, A.; Overstreet, A.; Corzine, K. A. Modified Z-Source DC Circuit Breaker Topologies. IEEE Trans. Power Electron. 2016, 31, 7394-7403.
176. Mokhberdoran, A.; Carvalho, A.; Silva, N.; Leite, H.; Carrapatoso, A. A New Topology of Fast Solid-State HVDC Circuit Breaker for Offshore Wind Integration Applications. In Proceedings of the 17th European Conference on Power Electronics and Applications, Geneva, Switzerland, 8-10 September 2015.
177. Häfner, J.; Jacobson, B. Proactive Hybrid HVDC Breakers - A Key Innovation for Reliable HVDC Grids. In Proceedings of the CIGRÉ International Symposium: Electric Power System of the Future - Integrating Supergrids and Microgrids, Bologna, Italy, 13-15 September 2011.
178. Lin, W.; Jovcic, D.; Nguefeu, S.; Saad, H. Modelling of High-Power Hybrid DC Circuit Breaker for Grid-Level Studies. IET Power Electron. 2016, 9, 2337-246.
179. Liu, G.; Xu, F.; Xu, Z.; Zhang, Z.; Tang, G. Assembly HVDC Breaker for HVDC Grids with Modular Multilevel Converters. IEEE Trans. Power Electron. 2017, 32, 931-941.

180. Feng, L.; Gou, R.; Yang, X.; Wang, F.; Zhuo, F.; Shi, S. A 320kV Hybrid HVDC Circuit Breaker Based on Thyristors Forced Current Zero Technique. In Proceedings of the IEEE Applied Power Electronics Conference and Exposition, Tampa, FL, USA, 26-30 March 2017.
181. Kim, B. C.; Chung, Y. H.; Hwang, H. D.; Mok, H. S. Comparison of Inverse Current Injecting HVDC Circuit Breaker. In Proceedings of the 3rd International Conference on Electric Power Equipment - Switching Technology, Busan, South Korea, 25-28 October 2015.
182. Z. Yang, H. Zhong, A. Bose, Q. Xia, and C. Kang, "Optimal Power Flow in AC-DC Grids with Discrete Control Devices," IEEE Transactions on Power Systems, Vol. 33(2), March 2018.
183. Callavik, M.; Blomberg, A.; Häfner, J.; Jacobson, B. The Hybrid HVDC Breaker, an Innovation Breakthrough Enabling Reliable HVDC Grids. ABB Grid Systems Technical Paper. 2012, 361, 143-152.
184. Liu, W.; Liu, F.; Zhuang, Y.; Zha, X.; Chen, C.; Yu, T. A Multiport Circuit Breaker-Based Multiterminal DC System Fault Protection. IEEE J. Emerg. Sel. Top. Power Electron. 2019, 7, 118-128.

# VITA AUCTORIS

Fazel Mohammadi is currently the Canada Representative in the CIGRE B3.52, C4.51, and C5.30 Working Groups. He is a Senior Member of IEEE, and an active member of CIGRE, EPE, AWEA, and IET. He serves as a Guest Editor for the Sustainability and Applied Sciences Journals. He is one of the recipients of Global Peer Review Awards powered by Publons as the top 1% of reviewers in each of the 22 Essential Science Indicators (ESI) research fields in the world. He was awarded the exceptional reviewer certificate for his contribution to the IEEE Transactions on Sustainable Energy journal, certificate and prize of excellence in reviewing for his contribution to the Springer Journal of Modern Power Systems and Clean Energy journal, and certificate of outstanding contribution in reviewing for his contribution to the Elsevier Renewable Energy journal all in 2019.

His research interests include Power System Control, Operation, Planning, and Reliability, High-Voltage Engineering and MT-HVDC Systems, Power Electronics Converters and Drives, Energy Storage Systems, Hybrid and Plug-in Electric Vehicles, Smart Grids Operation and Control, and Microgrids and Distributed Generations (DGs).